Project Report
OVLBI-1

A Survey and Assessment of Architectures for Optical Very Long Baseline Interferometry

D.M. Boroson
J.H. Shapiro
B. Dixon
J.B. Ashcom

10 June 2024

Lincoln Laboratory
MASSACHUSETTS INSTITUTE OF TECHNOLOGY
LEXINGTON, MASSACHUSETTS

This material is based upon work supported by the Under Secretary of Defense for Research and Engineering under Air Force Contract No. FA8702-15-D-0001.

This report is the result of studies performed at Lincoln Laboratory, a federally funded research and development center operated by Massachusetts Institute of Technology. This material is based upon work supported by the Under Secretary of Defense for Research and Engineering under Air Force Contract No. FA8702-15-D-0001. Any opinions, findings, conclusions or recommendations expressed in this material are those of the author(s) and do not necessarily reflect the views of the Under Secretary of Defense for Research and Engineering.

Massachusetts Institute of Technology
Lincoln Laboratory

A Survey and Assessment of Architectures for Optical Very Long Baseline Interferometry

D.M. Boroson
Division 6

J.H. Shapiro
B. Dixon
Group 67

J.B. Ashcom
Group 91

Project Report

OVLBI-1

10 June 2024

This material is based upon work supported by the Under Secretary of Defense for Research and Engineering under Air Force Contract No. FA8702-15-D-0001.

Lexington Massachusetts

This page intentionally left blank.

ABSTRACT

Motivated by the recent interest and publications in the quantum arena concerning possible improvements to Optical Very Long Baseline Interferometry (OVLBI), we have undertaken a survey and comparative analysis of a number of possible OVLBI architectures, both classical and quantum enabled. We assess here the feasibility and potential performance of them all, discussing a number of real-world considerations that must be taken into account. We also propose several technology-development paths that might lead to improved OVLBI performance.

As a brief summary, here are some of the main points of the report:

- The Gottesman et al. quantum-inspired OVLBI approach ([1],[2], to be called GJC here,) gives intrinsically slightly poorer performance than the standard classical approach, and the losses due to any optical transmissions have the same effect in both approaches.
- The GJC approach proposes making measurements over very wide bands (tens to hundreds of terahertz) one time-bandwidth slot at a time, an enormous speed. They observe that this can theoretically be done losslessly, even over lossy transmission media, using a quantum network. However, such a system would need to run even faster than that.
- The Khabiboulline et al. quantum-inspired OVLBI approach ([3], [4], to be called KBdGL here,) which depends on a quantum network, has potential performance better than the standard classical approach, and requires a much lower bandwidth quantum network than GJC. As a tradeoff, it requires enormous speed for its memory operations and quantum logic.
- For particularly bright objects, though, a space-based KBdGL approach might be less daunting.
- There is a purely classical, much simpler approach that achieves the same intrinsic performance as KBdGL, but it requires optical transmission, which might be lossy. An OVLBI designer would need to trade off both intrinsic and implementational losses to find the highest performance design.
- Both KBdGL and its classical counterpart lack a means for including corrections for turbulence and calibration errors, a problem that has been largely solved for the standard approach.
- All the investigated quantum-inspired approaches measure the huge time-bandwidth space one temporal mode at a time. Even in medium-brightness objects, there will be on the order of 100 million empty bins for every successful photon detection, which makes the engineering difficult.
- Quantum memories are central to both the quantum-inspired approaches. A huge parallel construction of narrow-band, wavelength-separated memories would be required for all the proposed concepts.
- Operating the OVLBI classically but in the fiber telecom bands, using state-of-the-art components, may actually give improved performance plus allow longer baselines.

This page intentionally left blank.

TABLE OF CONTENTS

		Page
	Abstract	iii
	List of Illustrations	ix
1.	INTRODUCTION AND BRIEF HISTORY OF VLBI	1
2.	DESIRED PERFORMANCE	3
3.	SOME EXISTING OVLBI SYSTEMS	9
	3.1 Naval Precision Optical Interferometer (NPOI)	9
	3.2 CHARA (Center for High Angular Resolution Astronomy)	10
4.	SIMPLIFIED CONCEPT OF OVLBI	11
5.	MAJOR ARCHITECTURE TRADEOFF – 1 – CORRELATIONS VS. FIELDS	13
	5.1 Introduction of Mathematical Models	13
	5.2 Pairwise Interferometric Processing: van Cittert-Zernike Theory	13
	5.3 Field Processing	15
6.	MAJOR ARCHITECTURE TRADEOFF – 2 – LOCAL VS. NON-LOCAL PROCESSING	17
	6.1 Local Classical Processing	17
	6.2 Two-Photon/Hanbury-Brown and Twiss Intensity Interferometer	18
	6.3 Non-local Classical Processing	18
7.	MAJOR ARCHITECTURE TRADEOFF – 3 – CLASSICAL VS. QUANTUM-ENABLED	21
	7.1 Classical	21
	7.2 Quantum Enabled	21
	7.3 How Many Photons?	26

TABLE OF CONTENTS
(Continued)

		Page
8.	PERFORMANCE ANALYSIS RESULTS	33
	8.1 Pairwise Measurement SNR – Classical Direct Detection	33
	8.2 Pairwise Measurement SNR – Classical Heterodyne	34
	8.3 Pairwise Measurement SNR – GJC	34
9.	IMAGE CREATION	37
	9.1 Correlation-Based Image Creation	37
	9.2 Array Geometry Requirements	38
	9.3 Field-Based Image Creation	39
	9.4 Field-Based Image Performance	42
	9.5 Quantum-Inspired Classical Field-Based Image Creation	43
	9.6 Turbulence and Calibration	44
10.	SIZING/PERFORMANCE EXAMPLES	47
11.	THE GJC/KBdGL APPROACHES – DISCUSSION AND SUMMARY	51
	11.1 (a) Intrinsic SNR Assessment	51
	11.2 (b) Baseline Length Assessment	52
12.	OTHER OVLBI REQUIRED SUBSYSTEMS – CLASSICAL AND QUANTUM	53
13.	QUANTUM MEMORIES	55
	13.1 Quantum Memory Banks	55
	13.2 Coherent Quantum Memories	56
	13.3 Quantum Memory CNOTs and Scaling for VLBI	58
14.	SUMMARY AND SUGGESTIONS	59
15.	REFERENCES	60

TABLE OF CONTENTS
(Continued)

Page

APPENDIX 1 – MATHEMATICAL MODEL 65

APPENDIX 2 – MATHEMATICAL ANALYSIS OF FAR-FIELD CORRELATIONS – THE VAN CITTERT-ZERNIKE THEORY 73

APPENDIX 3 – MATHEMATICAL ANALYSIS OF (DIRTY) IMAGE GENERATION VIA CLASSICAL FIELD-TRANSFORMATION 77

APPENDIX 4 – SIMPLIFIED QUANTUM ANALYSIS OF GJC - BINARY 79

APPENDIX 5 – SIMPLIFIED QUANTUM ANALYSIS OF GJC – M-ARY 83

APPENDIX 6 – PERFORMANCE ANALYSIS OF VC-Z WITH DIRECT DETECTION 85

APPENDIX 7 – PERFORMANCE ANALYSIS OF VC-Z WITH HETERODYNE DETECTION 87

APPENDIX 8 – PERFORMANCE ANALYSIS OF VC-Z WITH GJC MEASUREMENTS 89

APPENDIX 9 – QUANTUM LOGIC ANALYSIS OF KBdGL HERALDING 91

APPENDIX 10 – QUANTUM LOGIC ANALYSIS OF KBdGL MEMORY COMPRESSION 93

APPENDIX 11 – PERFORMANCE ANALYSIS OF (DIRTY) IMAGE FORMATION 95

APPENDIX 12 – CALCULATION OF (DIRTY) IMAGE FORMATION FROM QFT 97

APPENDIX 13 – CALIBRATION ANALYSIS OF (DIRTY) IMAGE FORMATION FROM FIELD TRANSFORMS 99

This page intentionally left blank.

LIST OF ILLUSTRATIONS

Figure No.		Page
1	Desired angular imaging resolution.	4
2a	Diffraction-limited resolution vs. wavelength as a function of maximum baseline distances, with several existing VLBI systems. Also note the black body radiation of the sun.	5
2b	Diffraction-limited resolution vs. wavelength and some future design goals.	6
3	Above - Photon flux density from a black body source with “apparent magnitude” zero, corresponding to Vega. Also shown (in red) is flux as transmitted through a typical atmosphere, all with the optical band definitions ([21].) Below – Translation from nm (pm) of wavelength to GHz of bandwidth.	7
4	Typical apparent magnitude ranges for classes of objects.	7
5	NPOI layout.	9
6	CHARA array.	10
7	Depiction of an interferometric array.	11
8	Major parts of OVLBI.	12
9	Left: NPOI static delay lines; right: CHARA variable delay lines.	12
10	Flow diagrams for two imaging approaches: vC-Z and field-transformed.	16
11	Heterodyne, “local” architecture.	17
12	Hanbury-Brown and Twiss intensity interferometer.	18
13	Classical, standard pairwise direct detection approach.	19
14	The GJC architecture.	22
15	A quantum network-enabled GJC system.	24

LIST OF ILLUSTRATIONS
(Continued)

Figure No.		Page
16	Depiction of success and timing in the two quantum network feeder paths, with delayed readout.	24
17	Photons/m^2/temporal mode vs. wavelength (in nm) for a 10-th magnitude object (through atmosphere).	27
18	KBdBL architecture.	28
19	Comparison of the GJC and KBdGL heralding approaches.	29
20	KBdGL data compression architecture.	30
21	Performing a 2-D DFT with multiple 1-D DFTs.	40
22	Transforming a 2-D DFT into a larger 1-D transformation.	41
23	Quantum-inspired classical field transforming.	43
24	Two approaches for implementing a unitary transformation on a PIC.	44
25	Example Photonic Integrated Circuit of an optical interferometer array.	44
26	Flux density and some relevant processing bands. The colored bands are the widely used optical fiber bands.	47
27	Depiction of a parallel quantum network construction of a KBdGL system. Such a system would need to have all the array telescopes on it.	48
28	Phase-coherent photon capture for VLBI is shown.	57
29	Heralding step for the array of quantum memories.	58
A-1	Geometry and math of the sky object and the telescope array.	67
A-2	Geometry of the planes of the sky object and the telescope array.	68

1. INTRODUCTION AND BRIEF HISTORY OF VLBI

Single aperture signal collectors, whether in radio or optical bands, when tasked with creating a 2-D image, can provide angular resolution only inversely proportional to the aperture diameter. The rule of thumb is that the smallest angular feature in a created image can be no smaller than $\frac{\lambda}{d}$ radians where λ is the wavelength and d is the aperture diameter. (This is the so-called diffraction limit.)

In the 19th and early 20th centuries, ([5], [6]) it was realized and demonstrated that interferometric combining of two small (sub)apertures a distance D apart can actually provide a measurement of phenomena at that narrow $\frac{\lambda}{D}$ angle. This coherent processing was understood to work even if the source of the energy is spatially incoherent.

Then, since the 1930s, ([7], [8]) it was realized that similar pairwise interferometric measurements between elements in a distributed aperture 2-D array can potentially be processed to provide a full 2-D image with angular features as small as $\frac{\lambda}{B}$ where B is the longest baseline; i.e., B is the distance between the antennas or telescopes. Although such a very sparse array obviously collects much less energy than a potential single large aperture of that diameter, it can be designed so that enough energy can be collected to perform adequately high-resolution imaging while having the chance of actually being feasible and affordable.

The first single-aperture astronomical radio receivers were built and used in the 1930s to measure single point sources, ([9], [10]) and the first radio interferometer was built in 1946 ([11].) But it took much technological creativity and a major new technique for calibration ([12]) before the first radio interferometric images were formed in 1967 ([13].) Since then, many developments have led to more and more capable radio Very Long Baseline Interferometers (VLBIs) culminating in the recent global-scale array—the Event Horizon Telescope (EHT), which famously produced an image in 2019 of a black hole ([14]).

In the optical bands, other than those initial stellar interferometers ([5], [6]) it was not until 1975 ([15]) that Labeyrie was first able to take the outputs from two separate telescopes and interferometrically combine them. Several years later, ([16], [17]) more practical methods were devised to lock the interference fringes between telescopes, even as the Earth turns and the object moves in the sky. The infrared optical bands were also considered ([18].) All that work set the stage for the present state of the art. (Some general references include [26]-[31].)

Two of the largest existing optical arrays for OVLBI are the NPOI (Navy Prototype Optical Interferometer, [20], 1994) and the CHARA (Center for High Angular Resolution Astronomy, [19], completed 2003) array, each with maximum baselines over 300 meters.

Needless to say, it is a technological challenge to build arrays of even those sizes. (See [26]-[31] also for general discussions of the relevant technologies.)

Relatively recently, there have been some OVLBI ideas using quantum techniques that have garnered much attention in the quantum community. Gottesman et al. ([1],[2]) and then Khabiboulline et al. ([3], [4]) devised new protocols that, they claimed, have the potential to allow optical OVLBI to grow longer or perhaps even to give improved signal-to-noise ratio (SNR) performance.

Over the past several years, our team at MIT Lincoln Laboratory has performed a study investigating these claims. During the period of the study, quite a few detailed internal memoranda were written and several lengthy summary briefings were prepared and given. This report summarizes all that work.

We first examine and quantify the phenomena we would like to be able to image. This will motivate the sizing of a future array.

To assess and compare a number of classical and quantum architectures, we then present a mathematical signal model that we use for calculating performance. Several performance metrics will be presented. We will use that model to assess each proposed architecture as well as to motivate the several basic imaging algorithms. We will also use it to introduce and assess the special signal processing required to operate a large Earth-bound array, as well as a space-based one.

We then look at the designs of the proposed quantum approaches, and compare their potential performance with classical techniques. We also size their technological needs.

2. DESIRED PERFORMANCE

We are interested in two basic classes of phenomena – near-Earth objects and Deep Space natural phenomena. We can state, arbitrarily, that we would be interested in centimeter-class or better resolution on images of structures at geosynchronous orbit. As can be seen in Figure 1, that corresponds to resolution about 0.25 nrad. We also observe that Pluto has a diameter that corresponds to between 0.32 and 0.56 urad as seen from Earth, so if we wanted to make an image with a resolution of, say, one-thousandth of that, we would need an angular resolution similar to the GEO need. Of course, since we already have images of Pluto, taken from near the planet, we would really like to look farther, and make images of the relatively close exoplanets. The very nearest stars are known to be about 10^4 times farther than Pluto, and so putting at least a few pixels across an image of such an object would need an angular resolution of at least 0.01 nrad.

In the figure, we can also observe that the EHT image of the black hole was stated to have a resolution of about 25 micro-arcsec, which corresponds to about 0.1 nrad. The EHT team has also announced that they would like to increase their maximum baseline by going to space, and so their goal is similar to our exoplanet goal of 0.01 nrad.

We next investigate diffraction-limited resolution limits according to $\frac{\lambda}{B}$, where B is the longest baseline, in frequencies from radio to optical. In Figure 2a, we show a range of resolution over these wavelengths, with baselines from one meter to one million kilometers. On this chart, we have placed the two OVLBI systems mentioned above ([19], [20]) as well as several radio-wave VLBI systems. Then, in Figure 2b, we augment that chart with the desired future resolutions. We can see that our goal for an optical system is at least several kilometers, if not many tens of kilometers.

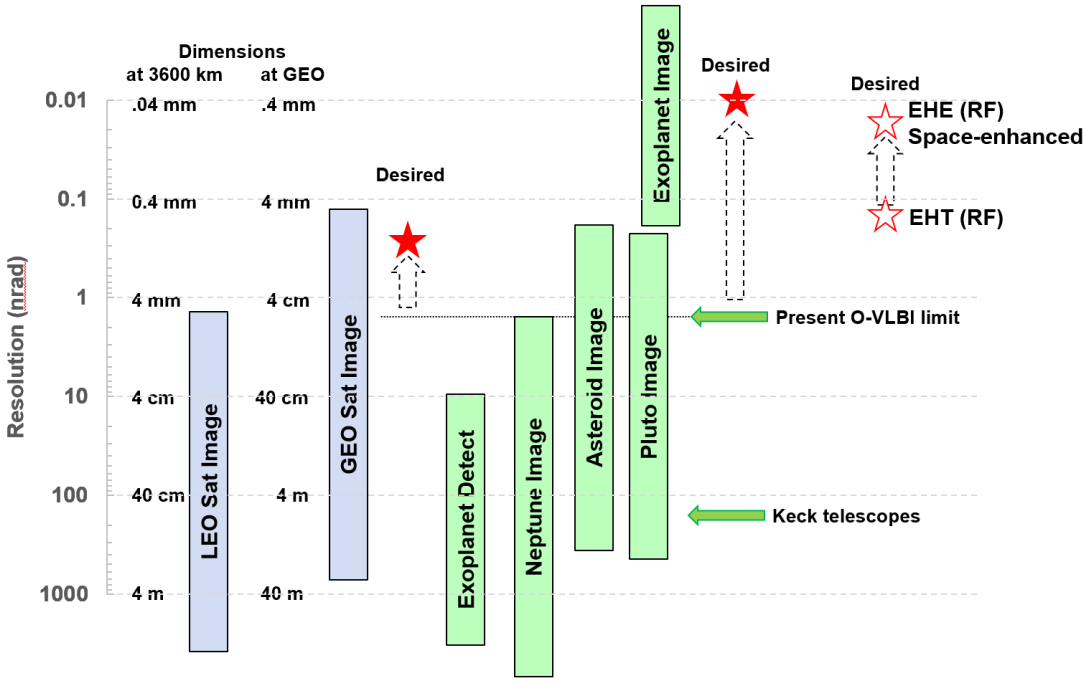

Figure 1. Desired angular imaging resolution.

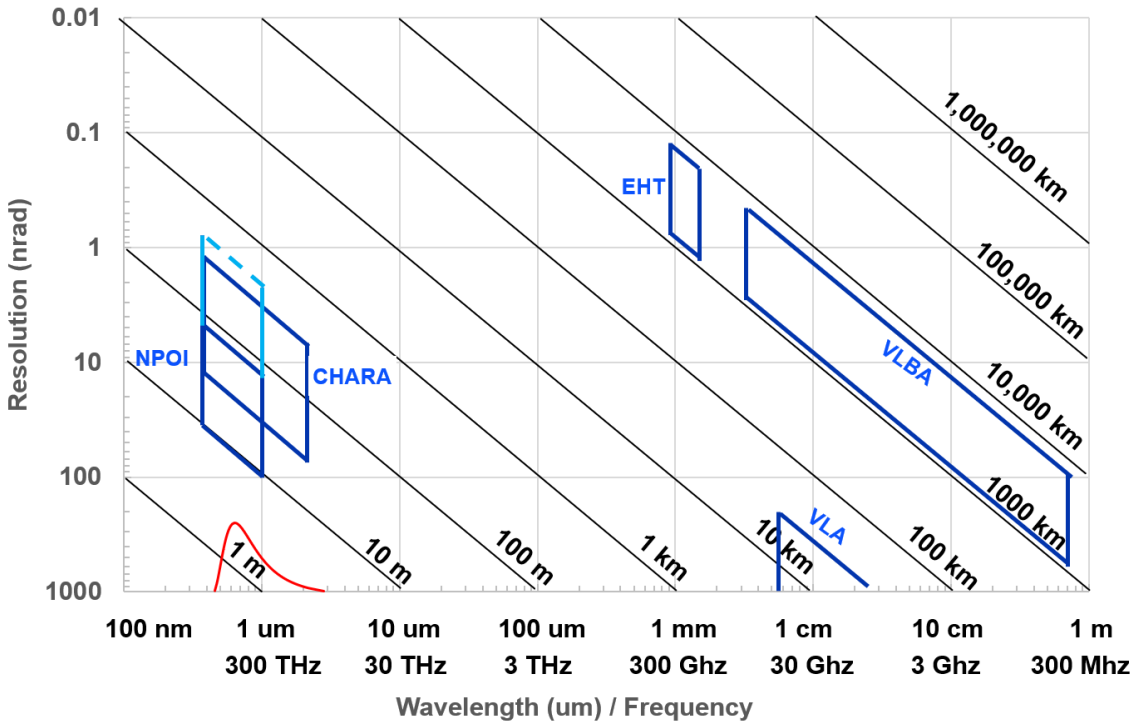

Figure 2a. Diffraction-limited resolution vs. wavelength as a function of maximum baseline distances, with several existing VLBI systems. Also note the black body radiation of the sun.

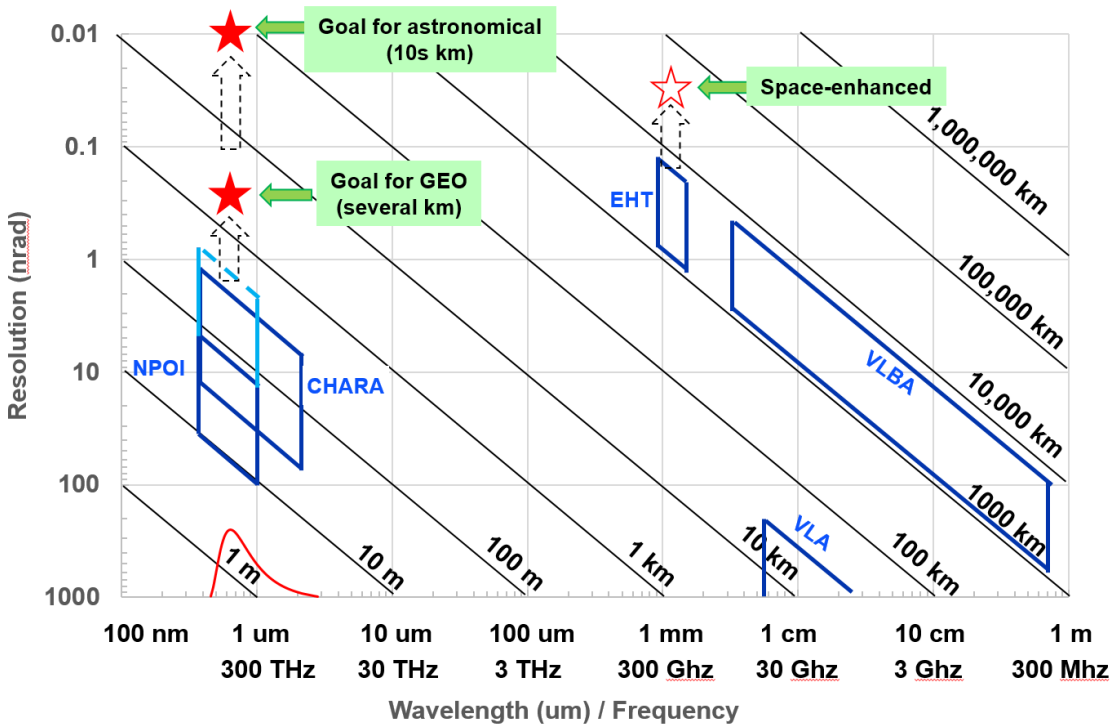

Figure 2b. Diffraction-limited resolution vs. wavelength and some future design goals.

We will also be interested in the range of brightnesses of interesting objects. In Figure 3, we show black body radiation from an object with "apparent magnitude" zero, corresponding to the brightness of Vega. Apparent magnitude is a reverse-logarithmic scale with each defined magnitude being exactly 4.0 dB dimmer. M_V is that magnitude defined in the optical V-band, shown in the figure.

Some approximate ranges of the brightnesses of interesting objects are shown in Figure 4, including many geosynchronous Earth orbit (GEO) objects and various astronomical objects. We will use Figures 3 and 4 in assessing the performance of arrays.

Figure 3. Above - Photon flux density from a black body source with "apparent magnitude" zero, corresponding to Vega. Also shown (in red) is flux as transmitted through a typical atmosphere, all with the optical band definitions ([21].) Below – Translation from nm (pm) of wavelength to GHz of bandwidth.

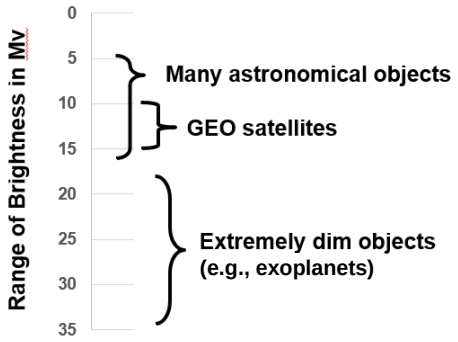

Figure 4. Typical apparent magnitude ranges for classes of objects.

This page intentionally left blank.

3. SOME EXISTING OVLBI SYSTEMS

3.1 NAVAL PRECISION OPTICAL INTERFEROMETER (NPOI)

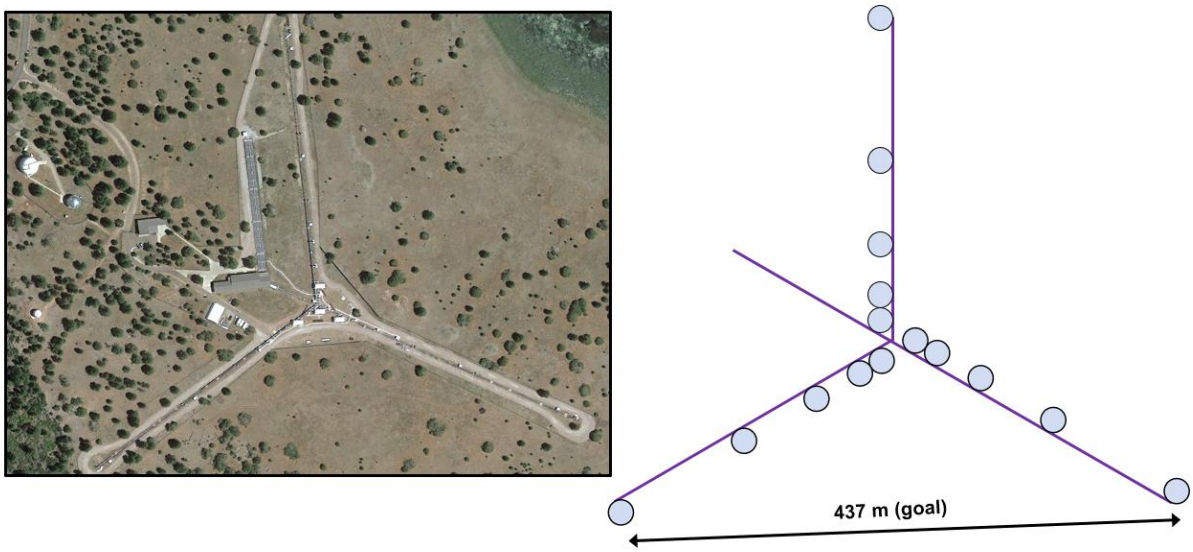

Figure 5. NPOI layout.

The NPOI—originally known as the NPOI, and then the Navy Optical Interferometer, but now known as the Kenneth J Johnston Navy Precision Optical Interferometer (still NPOI)—is situated in Flagstaff, AZ. It is only partially filled. It includes 0.5 m, 1.4 m, and 1.8 m telescopes and operates in V, R, and I bands. Its longest operational baseline to date is 89 meters although the goal is 437 meters.

3.2 CHARA (CENTER FOR HIGH ANGULAR RESOLUTION ASTRONOMY)

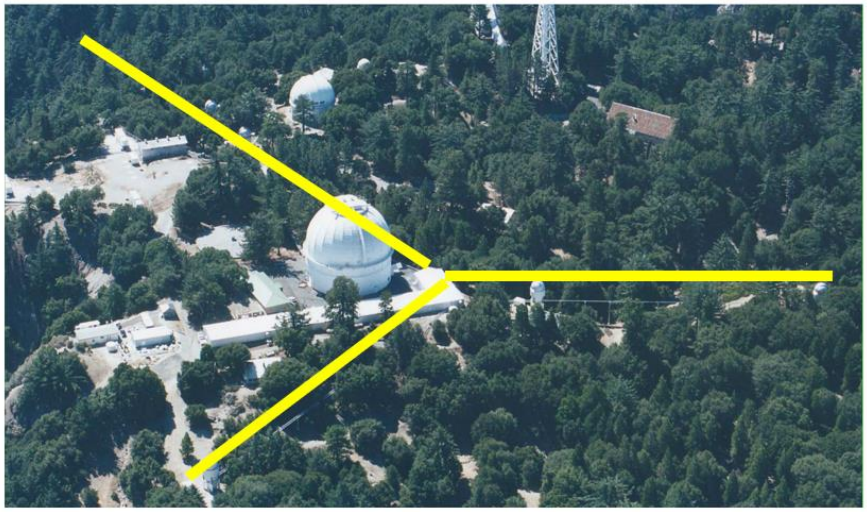

Figure 6. CHARA array.

The CHARA array is situated on Mt. Wilson, California, and is owned by Georgia State University. It consists of six one-meter telescopes with baselines from 31 m to 331 m and operates in the V, R, I, J, H, and K bands.

4. SIMPLIFIED CONCEPT OF OVLBI

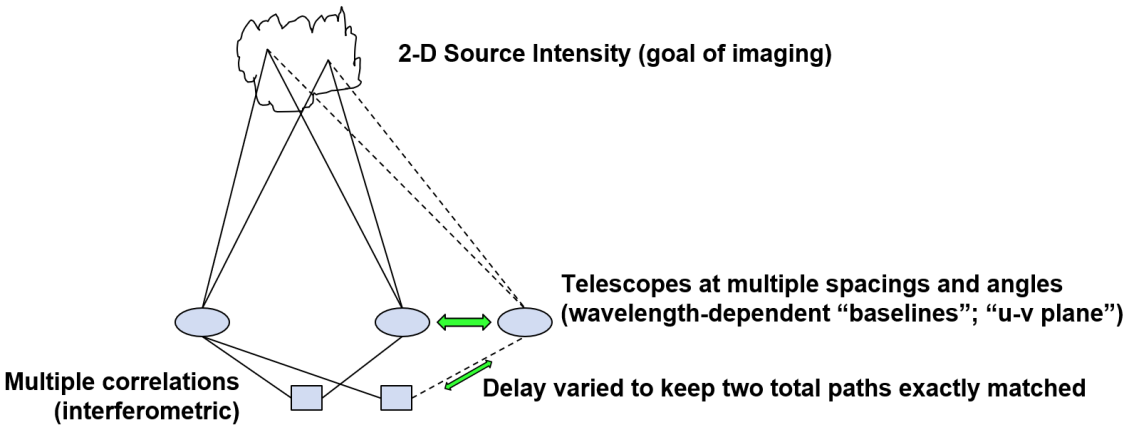

Figure 7. Depiction of an interferometric array.

In Figure 7, we depict a celestial 2-D source. All the telescopes in the array aim at its center. (We will be assuming that the telescopes are too small to resolve any details on the object, and so they all point at the dot in the sky that is the object.) They are placed at various positions on the array. The telescopes from each pair sends their light to a central place, where interference fringes are to be formed. In order for that to happen, the total light paths, from the source through the telescopes to the interferometer, must be matched (to within the coherence length of the bandwidth being examined) and then held steady to a fraction of a wavelength during the measurement. Since the object might not be exactly overhead, the paths from the two telescopes must have a delay added, and the delay must continuously vary as the object moves in the sky. We can see that, for a long baseline, the variable delay must be able to vary by nearly that full length. It must also be kept stable enough to find and lock onto interference fringes. Polarization must also be maintained throughout.

We indicate in Figure 8 some of the required components—active adaptive optics systems so that the beams from the separate telescopes are single spatial modes and thus can be interfered in that single spatial mode; long fixed delays; long variable delays; fringe trackers; and various kinds of beam combiners.

The long fixed and variable delays need to transmit with as little loss as possible, as we will see in our performance analyses. We know, though, that low-loss optical fiber is optimized for telecom wavelengths, and not the V and R bands. For instance, a recent Corning spec sheet shows that their PM1550 fiber has 0.5 dB/km loss while their PM630 has 12 dB/km. For that reason, as well as the need to compensate for any differential dispersion, present-day OVLBI systems send the beams through evacuated pipes. Some examples of these are depicted in Figure 9.

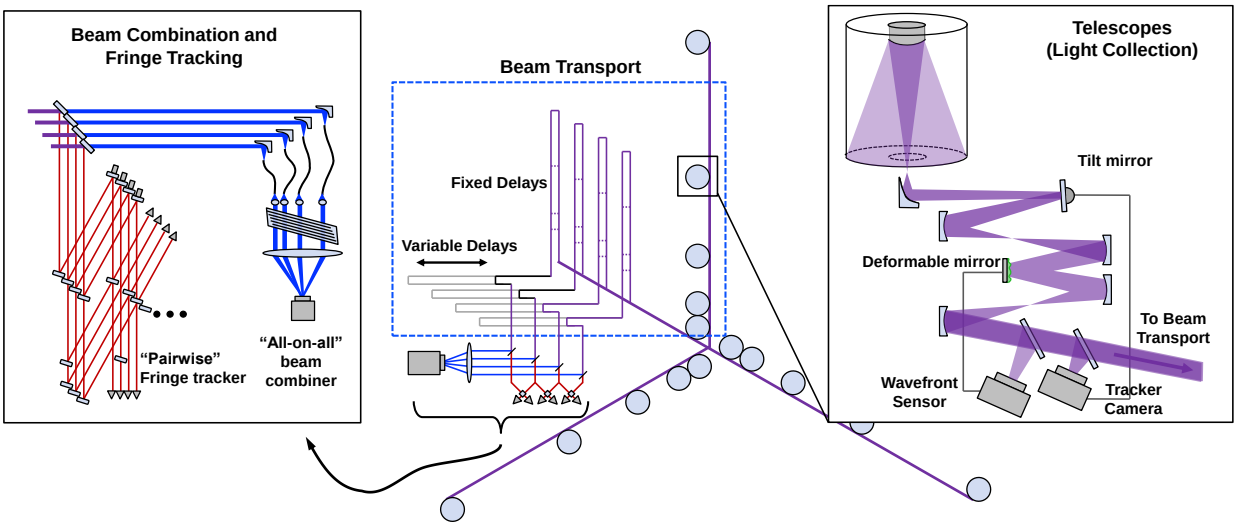

Figure 8. Major parts of OVLBI.

Figure 9. Left: NPOI static delay lines; right: CHARA variable delay lines.

The present simple designs would not easily be able to extend to multiple kilometers, and would certainly incur appreciable loss. (We note that, as part of our study, we have investigated a design variant where the beam pupils could be relayed every few hundred meters. Our analysis shows that such an approach could extend the delay out to several kilometers with "only" perhaps 4 to 6 dB loss.)

5. MAJOR ARCHITECTURE TRADEOFF – 1 – CORRELATIONS VS. FIELDS

5.1 INTRODUCTION OF MATHEMATICAL MODELS

We will now examine two basic approaches to array-based imaging: interferometric processing and optical field processing. (They will both be needed in order to understand the two quantum-inspired approaches.) To begin, we will create a single consistent mathematical model of the signals. (Most of the details of the derivation are shown in Appendix 1.) We will first find a classical description. In the sequel, we will find a quantum description.

The relation between the field as captured in telescope K in the array with the field as it is leaving the sky object is (with some irrelevant terms removed—see (A1-22))

$$E_K(t) \equiv \frac{\sqrt{A_K}}{j\lambda Z} \int_{\mathcal{A}_S} d^2\boldsymbol{\rho}\, E_s(\boldsymbol{\rho}, t) e^{-j\frac{2\pi \boldsymbol{\rho}_K \cdot \boldsymbol{\rho}}{\lambda \; Z}} \tag{1}$$

As described in Appendix 1, we have

- $\boldsymbol{\rho}$ is the 2-D vector describing the position of the sky object in its plane, defined to be centered at (0,0)
- $E_s(\boldsymbol{\rho}, t)$ is the scalar field of the sky object in the plane of the object
- Z is the distance from the sky object to the sub-object point on the Earth
- $\boldsymbol{\rho}_K$ is the 2-D vector describing the position of the Kth telescope in the plane of the array (See Figure A-1 and A-2)
- A_K is the area of the Kth telescope
- λ is the center wavelength of the "quasimonochromatic" band of interest. Optical filtering with center wavelength λ and bandwidth $\Omega \ll \lambda$ is to be performed at the telescopes. Without loss of generality, this filtering can be assumed to occur at the astronomical objects so that the astronomical light can be modeled as quasimonochromatic on the carrier ω_0 where $c = \lambda\, \omega_0/2\pi$.
- $E_K(t)$ is the single-spatial-mode field as captured by the telescope

5.2 PAIRWISE INTERFEROMETRIC PROCESSING: VAN CITTERT-ZERNIKE THEORY

For interferometric and general imaging needs, we model the source field envelope as a zero-mean, Gaussian random field that is completely characterized by its phase-insensitive correlation function, (see (A1-8)

$$\langle E^*{}_s(\boldsymbol{\rho}, t+\tau) E_s(\boldsymbol{\rho}', t) \rangle = \lambda^2 N_S I_s(\boldsymbol{\rho}) R_s(\tau) \delta(\boldsymbol{\rho} - \boldsymbol{\rho}') \tag{2}$$

where $\langle . \rangle$ denotes ensemble average. Here:

- $I_s(\boldsymbol{\rho}) \geq 0$ is the source's (sky-centered) normalized spatial distribution.
- N_S is the source brightness (in photons/s-Hz);
- $\delta(\boldsymbol{\rho}) = \delta(x)\,\delta(y)$ is the 2-D delta function with dimension 1/m^2;
- $R_s(\tau)$ is the normalized temporal correlation function such that $N_S R_s(0)$ is the source's average photon flux, and $N_S I_s(\boldsymbol{\rho}) R_s(0)$ is its average photon flux density at location $\boldsymbol{\rho}$ and time t.

The source's associated dimensionless spectral density is then defined

$$S_s(\omega) = \int d\tau R_s(\tau) e^{-j\omega\tau}$$

which has bandwidth Ω due to filtering as described earlier.

We can then calculate the correlation between the complex fields at telescopes k and j to find (see A2-1)

$$\langle E_k{}^*(t+\tau) E_j(t) \rangle = e^{j\frac{2\pi(|\boldsymbol{\rho}_K|^2 - |\boldsymbol{\rho}_J|^2)}{2\lambda Z}} \left\{ \frac{\sqrt{A_K A_J}}{Z^2} N_S R_s(\tau) \right\} \int_{\mathcal{A}_S} d^2\boldsymbol{\rho}_1 \; I_s(\boldsymbol{\rho}_1) e^{j\frac{2\pi(\boldsymbol{\rho}_K - \boldsymbol{\rho}_J)\cdot\boldsymbol{\rho}_1}{\lambda Z}} \tag{3}$$

This mutual coherence term is sometimes called the "visibility." The out-front phase term is a very small constant that can either be calculated and removed or merely ignored, so we find (see A2-2)

$$\langle E_K{}^*(t) E_J(t) \rangle = \left\{ \frac{\sqrt{A_K A_J}}{Z^2} N_S R_s(0) \right\} \int_{\mathcal{A}_S} d^2\boldsymbol{\rho} \; I_s(\boldsymbol{\rho}) e^{j\frac{2\pi(\boldsymbol{\rho}_K - \boldsymbol{\rho}_J)\cdot\boldsymbol{\rho}}{\lambda Z}} \tag{4}$$

Calculating and removing or normalizing the term in brackets, we have the van Cittert-Zernike (vC-Z) theorem ([7],[8], in its deep far-field quasimonochromatic version): the complex correlation between the fields collected at two telescopes is proportional to the 2-D spatial Fourier transform of the spatial distribution we want to image as calculated at a spatial frequency related to the vector between the telescopes (i.e., the baseline.) From this observation, we are motivated to try to measure this correlation value at many spatial frequencies (i.e., baselines) and then try to calculate an inverse (and discrete) 2-D Fourier Transform to recover the image.

In Appendix 2, we walk through the steps of inverting this Fourier Transform. We first rewrite the visibility, (4) (again, with $\tau = 0$ and with the bracketed term removed) in its 2-D form as

$$g\left(\frac{\Delta x_{jk}}{\lambda}, \frac{\Delta y_{jk}}{\lambda}\right) = \int_{-\infty}^{\infty} \int \tilde{I}_S(\xi, \eta) \, exp\left[j2\pi \left(\frac{\Delta x_{jk}}{\lambda} \xi + \frac{\Delta y_{jk}}{\lambda} \eta \right) \right] d\xi d\eta \tag{5}$$

where g(.,.) is the measured correlation; $(\Delta x_{jk}, \Delta y_{jk})$ are the x,y coordinates of the baseline between the centers of telescopes j and k; $\tilde{I}_S(\xi, \eta)$ is the source's normalized distribution in angular coordinates; and (ξ, η) are the x, y coordinates of the angles to the sky object.

We then perform the Inverse Discretized Fourier Transform of this set of values for N telescopes to get:

$$\tilde{\tilde{I}}_s(\hat{\xi},\hat{\eta}) \approx \frac{1}{N^2}\sum_j\sum_k g\left(\frac{\Delta x_{jk}}{\lambda},\frac{\Delta y_{jk}}{\lambda}\right) exp\left[-j2\pi\left(\frac{\Delta x_{jk}}{\lambda}\hat{\xi}+\frac{\Delta y_{jk}}{\lambda}\hat{\eta}\right)\right] \tag{6}$$

$$= \frac{1}{N^2}\int_{-\infty}^{\infty}\int \tilde{I}_S(\xi,\eta)\left\{\sum_j\ \sum_k\ exp\left[j2\pi\left(\frac{\Delta x_{jk}}{\lambda}[\xi-\hat{\xi}]+\frac{\Delta y_{jk}}{\lambda}[\eta-\hat{\eta}]\right)\right]\right\} d\xi d\eta$$

Note that the summations are over the pairs of telescopes. Here we see the result of having only a sparsely sampled set of Fourier-plane values. (This plane is sometimes called the u-v plane because in some references, $(\frac{\Delta x_{jk}}{\lambda},\frac{\Delta y_{jk}}{\lambda})$ is defined as (u,v).) We will have calculated $\tilde{\tilde{I}}_s$, often called the "dirty image," which is seen here to be the convolution of the correct image, $\tilde{I}_s$, with the term in brackets, commonly known as the "dirty beam."

Note also that, if there are N telescopes, then there are $\binom{N}{2}$ unique pairs, and there are thus $\binom{N}{2}$ unique terms (plus their complex conjugates) as well as N identities in the double summation of the 2-D Inverse Discretized Fourier Transform.

We will examine several ways to measure these correlations in the sequel. We will also examine the calculation of the Fourier transform.

5.3 FIELD PROCESSING

As we will see, pairwise correlation of signals, followed by vC-Z -motivated Fourier transforming constitute the standard classical VLBI approach. We can also observe, though, that equation (1) is

$$E_K(t) \equiv \frac{\sqrt{A_K}}{j\lambda Z}\int_{\mathcal{A}_S} d^2\boldsymbol{\rho}\ E_s(\boldsymbol{\rho},t)e^{-j\frac{2\pi\boldsymbol{\rho}_K\cdot\boldsymbol{\rho}}{\lambda\ \ Z}} \tag{7}$$

which tells us that, similar to but different from the vC-Z theorem, the set of received fields at the telescopes are samples of the spatial 2-D Fourier Transform of the field at the source. In Appendix 3, we find, first, the Inverse Discretized Fourier Transform of this field (A3-3)

$$\tilde{\tilde{E}}_s(\hat{\xi},\hat{\eta},t) \approx \frac{1}{N}\sum_k E_k(t)\ exp\left[-j2\pi\left(\frac{x_k}{\lambda}\hat{\xi}+\frac{y_k}{\lambda}\hat{\eta}\right)\right] \tag{8}$$

where the summation is over the telescopes. We can observe that, for an N-telescope array, this Inverse Fourier Transform has only N terms in the sum.

We will be interested in the image, though, so we calculate the squared magnitudes of this transformed field to find

$$\left\langle \left| \tilde{\tilde{E}}_s(\hat{\xi},\hat{\eta},t) \right|^2 \right\rangle \approx \frac{1}{N^2} \int_{-\infty}^{\infty} \int \tilde{I}_S(\xi,\eta) \left\{ \sum_{j,k} exp\left[j2\pi \left(\frac{\Delta x_{jk}}{\lambda} [\xi - \hat{\xi}] + \frac{\Delta y_{jk}}{\lambda} [\eta - \hat{\eta}] \right) \right] \right\} d\xi d\eta \quad (9)$$

which is seen to be the same result as (6), the dirty image of the vC-Z approach. This is an important result. (As in (5),(6), we have omitted the bracketed term shown in (4).)

We have thus learned that there are two approaches to finding the interferometric dirty image: we can first perform pairwise correlations, integrate these up over the measurement integral, and then take the Inverse Discretized Fourier Transform; or we can first capture the 2-D fields and take their Inverse Discretized Fourier Transform, find their square-law values, and then integrate those values up. These two approaches are depicted in Figure 10.

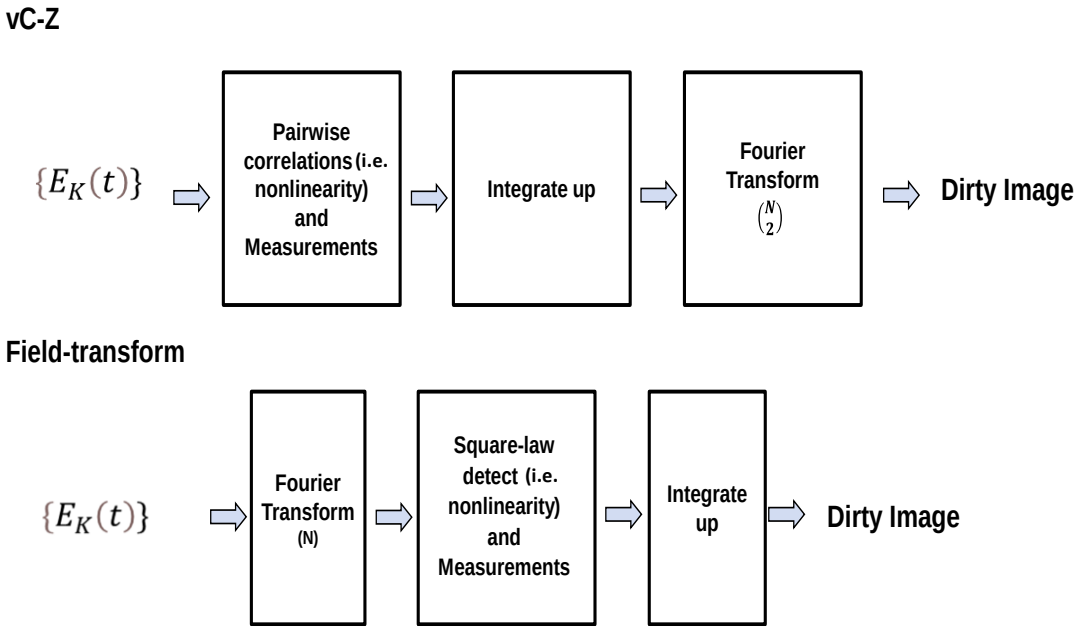

Figure 10. Flow diagrams for two imaging approaches: vC-Z and field-transformed.

Each approach has its pluses and minuses, which we will investigate further. And they will both be shown to have analogs in the quantum-enabled approaches.

6. MAJOR ARCHITECTURE TRADEOFF – 2 – LOCAL VS. NON-LOCAL PROCESSING

6.1 LOCAL CLASSICAL PROCESSING

We will now briefly investigate architectures of so-called "local" processing and "non-local" processing. (See [22] for a first-principles view.) By "local" processing, we mean that any manipulation of the received electro-magnetic energy happens in or behind the telescope (or antenna,) and only the measurement values are sent on classically to a central processor. The local processing method used by RF VLBI systems is the heterodyne approach. In this, a single local oscillator (LO) is split and sent to each of the telescopes. At each telescope, this (high signal power) LO is mixed with the incoming energy, and, at the Nyquist frequency of the processor, measurements of the in-phase and quadrature values of the beat signal are recorded. This architecture is depicted in Figure 11.

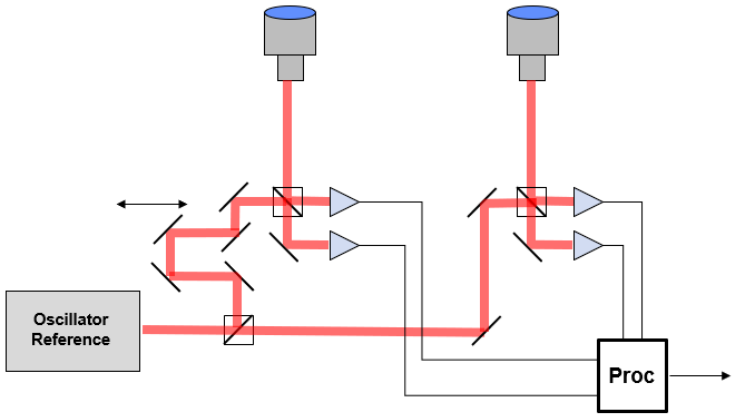

Figure 11. Heterodyne, "local" architecture.

We show a controlled variable delay on the delivered LO, because we want the LO to arrive at all the telescopes so that a received plane wave would produce a measured linear phase slope across the array. Of course, this whole system could instead be implemented with locally generated oscillators that are synchronized and time-offset somehow. We will see in the sequel that there are methods to correct any near-constant phase errors as seen in the array of telescopes, so a system architect might opt to omit the variable delay in a heterodyne system.

Since the measurement is made locally, the bandwidth that can be measured must be small enough that the heterodyne beat signal is within the bandwidth of the detection and measurement system. Likely, a very-wide band total measurement will need to be split into a number of parallel narrower-band and simultaneous measurements.

We see that we will have captured a replica of the fields at the telescopes. These can then either be used to create pairwise correlations with vC-Z Inverse DFTs, or they can be Inverse DFTed as fields with processing as shown in Figure 10.

This heterodyne approach is also valid for optical bands, but we will see in our analysis sections that it gives poor SNR performance there.

We can see that, since it is a known classical signal that is to be sent to the telescopes for their "local" heterodyne measurements, that signal can be amplified before and/or after the transmission, and so losses in the transmission are unimportant, although any added noise would need to be filtered out. Such a system could then have very large baselines.

6.2 TWO-PHOTON/HANBURY-BROWN AND TWISS INTENSITY INTERFEROMETER

In 1956, Hanbury-Brown and Twiss ([23], [24], [25]) devised a method whereby direct detections are performed locally, and the correlations of the measured photon detection statistics are performed non-locally (see Figure 12). Their so-called "intensity interferometer" requires no phase reference, but only a time reference. It is known that their approach does not work well on dim targets, though, since it requires pairs of photons to be detected, and photons are known to be sparse for the kinds of targets we are interested in.

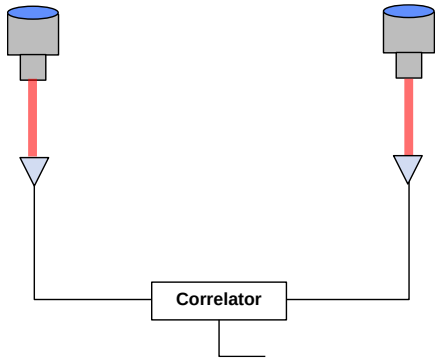

Figure 12. Hanbury-Brown and Twiss intensity interferometer.

6.3 NON-LOCAL CLASSICAL PROCESSING

6.3.1 Classical Interferometer

Motivated by the van Cittert-Zernike formulas of Section 5.2, the standard method of VLBI in the optical bands is non-local, pairwise interferometry. See Figure 13 for a depiction.

In this approach, the received light signals from each pair of telescopes, spaced by some baseline, are sent to a central location where they are interfered and photons are measured/counted. To perform interferometry, both beams need to be in the same spatial mode, so either an active adaptive optics subsystem must be part of each telescope, or the telescopes must be smaller than the atmosphere's coherence length. As mentioned earlier, the beamsplitter performing the interferometry needs to be equidistant from the source via both paths. So if the object is not straight overhead and/or the central station is not equally distant from the telescopes, one path from a telescope to the beamsplitter needs to have extra delay inserted. For many hours of continuous measurement of a sky object from a rotating Earth, then, that means that the inserted variable delay might need to grow to be almost as long as the delay itself. The mechanism also needs to be stable enough that interference fringes are created and stay stable, even as the system follows the sky object. We showed some real-world systems that accomplish this difficult task in Figures 8 and 9.

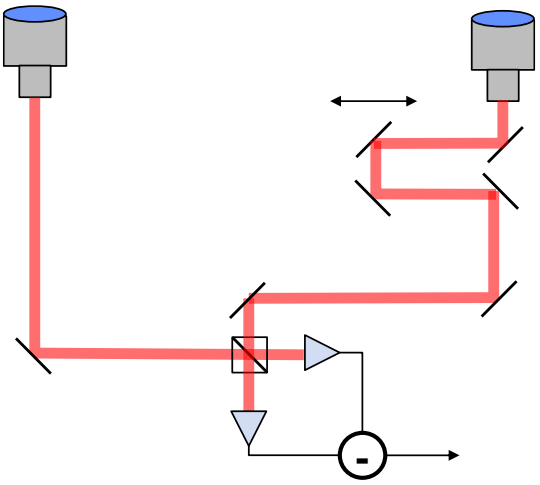

Figure 13. Classical, standard pairwise direct detection approach.

It is this complex non-local system that is generally lossy, thus seeming to preclude extensions of OVLBI to multiple kilometer lengths.

This page intentionally left blank.

7. MAJOR ARCHITECTURE TRADEOFF – 3 – CLASSICAL VS. QUANTUM-ENABLED

The third major architecture tradeoff finally brings us to the motivation for this study—the pure classical approaches vs. several new approaches requiring quantum techniques.

7.1 CLASSICAL

All the approaches suggested so far have been "classical." That is, processing of the received light consists of undistorted transmission, beam-splitters, filtering, and detection. (We admit that we invoke single-photon detectors which can be considered "quantum," but they really just implement classical direct detection operating in the most efficient way possible.) Any assisting light fields (such as local oscillators) are also classical. That is, the heterodyne approach would use a narrow-line classical laser as the means of both referencing the phase and providing a means of adding gain into the measurement of the weak signals. Finally, and perhaps most importantly, the classical approaches do not depend on any entanglement properties of pairs of signals.

7.2 QUANTUM ENABLED

In 2012, ([1], [2]) Gottesman, Jennewein, and Croke (GJC) proposed a quantum-enabled approach for measuring the correlations required in the vC-Z approach. Motivated by this work, Khabiboulline, Borregaard, De Greve, and Lukin (KBdGL) ([3], [4]), subsequently proposed a related approach, making direct use of quantum memories. In this section, we will describe their approaches. In a later section, we will investigate their performance, and compare them with the classical approaches.

The goals of both these approaches were to:

a) improve the SNR, and/or
b) allow longer baselines

We will create metrics to allow us to investigate if either or both of these goals can actually be achieved.

7.2.1 The GJC Approach: Binary, Photonic Implementation

The GJC approach first presented a two-telescope concept. When the incoming light is very weak (and we will quantify this property in the next section) one can approximately model the incoming, deep-far-field signal as a tilted plane wave with at most one photon across the two telescopes in a particular time bin and frequency window. The quantum signal at the two telescopes (when a photon is present in the array) can thus be denoted

$$\frac{1}{\sqrt{2}}\left[|0\rangle_{LT}|1\rangle_{RT} + e^{j\emptyset}|1\rangle_{LT}|0\rangle_{RT}\right]$$

The GJC concept is to transmit, in each possible time bin, an entangled qubit created by putting a single photon into a beam splitter, resulting in a signal denoted

$$\frac{1}{\sqrt{2}}\left[|1\rangle_{LN}|0\rangle_{RN} + e^{j\delta}|0\rangle_{LN}|1\rangle_{RN}\right],$$

This signal is sent across the "Network" to the two telescopes as shown in Figure 14. These are interfered with the incoming state in two beamsplitters. Both this approach and the classical approach of Figure 13 are analyzed in Appendix 4. We observe that the classical approach is "non-local," but the GJC approach can be considered "local."

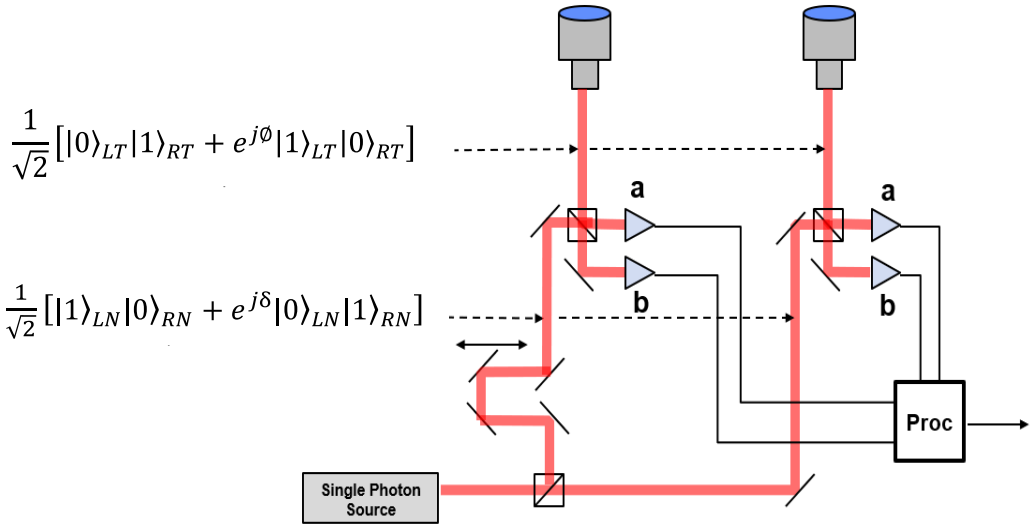

Figure 14. The GJC architecture.

There are four possible measurement results in each time bin in GJC:

1. Only one photon is measured (and it must have been from the network,) and so the time bin is ignored
2. Two photons are measured on one side or the other, and that time bin is ignored (and this occurs half the time that a sky photon is received)
3. One photon is measured on each side as ab or ba, with probability

$$(1 - |V|\cos(\Theta - \delta))/2) \tag{10}$$

4. One photon is measured on each side as aa or bb, with probability
$$(1 + |V|\cos(\Theta - \delta))/2) \tag{11}$$

Also shown in Appendix 4 is the fact that these two probabilities are the same as in the classical case of Figure 13, although the classical case does not have the 50% loss that the GJC case has.

7.2.2 The GJC Approach – Binary, Qubit Implementation

We can see that trying to send the entangled photons over a transmission line would result in losses (whose performance we will quantify in the next section) very similar to the signal-transmission losses inherent in the classical case shown in Figure 13. GJC states that this transmitted signal, encoded as an entangled qubit could, instead, be sent losslessly (even over a lossy fiber) using quantum repeaters in a quantum network. This would be possible if the qubit receivers at the two telescopes could independently and then jointly herald the successful receptions of the entangled qubit. With quantum memories and the capability to create and transmit the qubits at a rate higher than the measurement rate, this might, indeed, be possible. A qubit in the form of the single, beam-split photon, however, cannot be independently heralded at the two telescopes without giving away where the photon is or utilizing some other pre-distributed entanglement.

One could, instead, transmit a polarization qubit such as VH or HV. Steps would be

1. Create and transmit
$$\left(|H\rangle_{LN}|V\rangle_{RN} + e^{j\delta}|V\rangle_{LN}|H\rangle_{RN}\right)/\sqrt{2} \tag{12}$$
2. Receive, herald the success of, and then store the photons in quantum memories
3. Using classical communications, compare the heralds and keep the qubits only if they both were successful
4. Perform this fast enough so that, even after lost qubits, there are enough in memory to match the desired measurement rate
5. Store the qubits until measurement time, when the VH qubits are coherently read out and translated into a sky-photon-matched optical qubit
$$\left(|0\rangle_{LN}|1\rangle_{RN} + e^{j\delta}|1\rangle_{LN}|0\rangle_{RN}\right)/\sqrt{2} \tag{13}$$

and the GJC measurement is then performed.

This concept is depicted in Figure 15. Such an approach would solve several problems: allow the heralding required for the quantum repeater function, choose a transmission modality matched to the quantum memory, and select wavelengths for the best network/memory design.

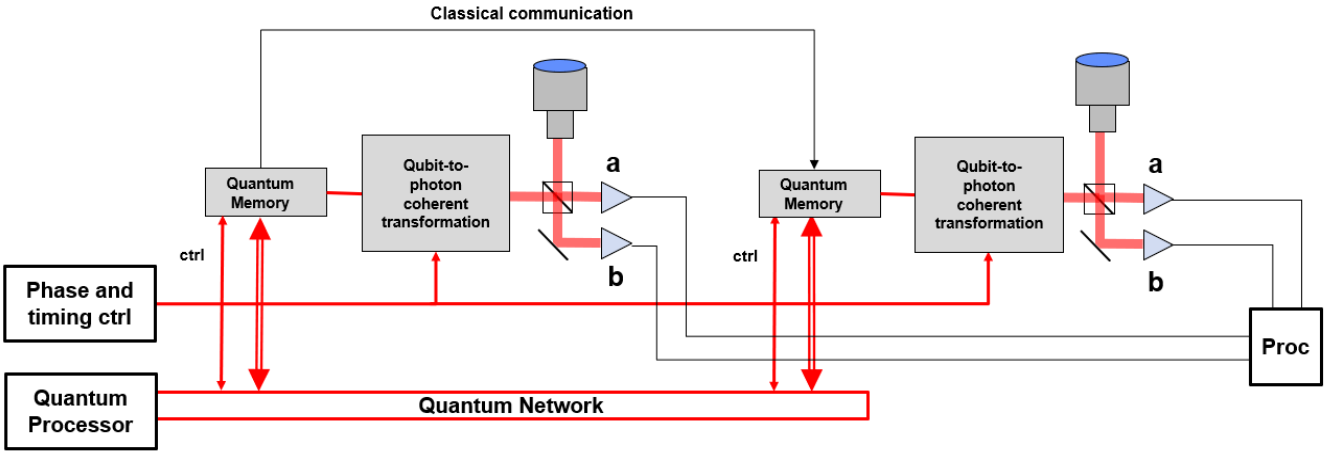

Figure 15. A quantum network-enabled GJC system.

In Figure 16, we depict how the timing of the quantum memories could be used to make use of somewhat lossy transmission. Only when both telescopes have heralded the successful receipt of the qubit do they make use of the entangled pair. Of course, the network and memories would need to run faster than the measurements in order to make up for losses. Also, the memories would need to have a long enough duration to deal with all the delays in the system, including the classical comparison of heralds.

Then, that wideband transmitted and stored qubit would need to be read out and transformed to a lower-bandwidth (and carefully phase-controlled) sky photon. Almost certainly, the sky photons would need to be narrow-band filtered and processed in a wavelength-division-multiplexed manner in order to make measurements over a wide enough band to detect enough photons.

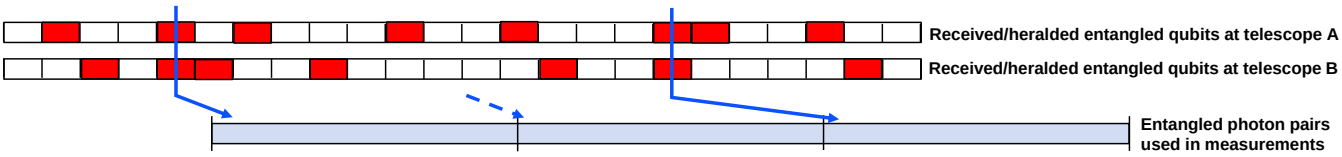

Figure 16. Depiction of success and timing in the two quantum network feeder paths, with delayed readout.

An interesting feature of this quantum memory bank approach is that all the variable delay-compensation required by the array could be implemented with carefully and dynamically re-timed readouts of the qubits in the quantum memories instead of physically delayed signals. This feature of adequately large quantum memories could possibly result in a big cost-saving for OVLBI.

7.2.3 The GJC approach – M-ary

We saw that the GJC approach, using either photons or qubits, has an inherent 50% loss due to the created photon "landing on" the same telescope as where the sky photon lands. GJC pointed out that this loss could be reduced by sending the entangled qubit to more than two telescopes at a time. Similar to the previous sections, this could be implemented either by

1. Creating a single photon and sending it through an M-ary splitter, denoted

$$|\varphi\rangle = \frac{1}{\sqrt{M}}\left[|1_0\rangle + e^{j\delta_1}|1_1\rangle + e^{j\delta_2}|1_2\rangle + e^{j\delta_3}|1_3\rangle + \cdots\right] \tag{14}$$

where we let $|1_k\rangle$ be the ket with a 1 at the k'th position and 0 elsewhere. This state is known as a "W-state". Or we can create, similar to our binary version,

2. an M-ary W-state dual-rail qubit such as

$$|\varphi\rangle = \frac{1}{\sqrt{M}}\left[|\text{HVVV ...}\rangle + e^{j\delta_1}|VHVV..\rangle + e^{j\delta_2}|VVHV..\rangle + \cdots\right] \tag{15}$$

Similar to the binary quantum network case, these would all need to be heralded and stored, have their heralds compared to identify those cases where all M were received, and then translated to photons matched to the sky photons.

In Appendix 5, we investigate the mathematics of an array system with M telescopes.

Here is a simple analysis of the benefit of the W-state M-ary approach:

Suppose we had 2M telescopes, each with a (very small) probability ε of receiving a sky photon in a particular time-frequency bin. If we were to use the pairwise GJC approach simultaneously on M pairwise systems, then each of the pairs would have a 2ε probability of having a photon, so the array will have had a probability of $2M\varepsilon$ of receiving a single sky photon. The 50% GJC loss would mean that the entire array would then have a probability of $M\varepsilon$ of making a successful pairwise measurement. Such a system would require M parallel disseminated entangled qubits.

If, instead, we could create and disseminate a dimension-2M W-state, there would be the same $2M\varepsilon$ probability that a sky photon is received somewhere in the array, but then a (1-1/2M) probability of the W-

state photon landing on an empty telescope. Thus, the probability of making a successful GJC pairwise measurement would be $2\varepsilon(\mathrm{M}-\frac{1}{2})$, which gets closer and closer to fully picking up the lost factor of 2 as M gets larger.

We note, though, that this approach produces a single pairwise measurement, but with a randomly selected pair. The designer thus has a little less control on what gets measured at any one time. Of course, many total photons need to be measured in any case, and the randomness should not be a problem given a long enough measurement period. Ultimately, all the pairs will have been measured.

We also note that a Quantum Network would need to be able to transmit these 2M-mode W-states in a lossless (or lossless via heralding/retransmit) fashion. In [1], [2] the GJC authors propose a few methods to accomplish this, without full details, but they do observe it would take more resources and more complexity.

We briefly note here that the total rate of delivered qubits needs to be equal to the bandwidth of the desired OVLBI measurements. As we will discuss further, this number is tens to hundreds of terahertz.

7.3 HOW MANY PHOTONS?

Throughout this discussion, we have pointed out that there are few photons arriving from sky objects of interest. Here, we put some numbers on this. In Figure 3, we had shown flux for a Magnitude-0 object in terms of photons/sec-m^2-nm. In Figure 4, we had shown the magnitudes of typical objects of interest.

Flux is often measured in Ph/s/m^2/nm, but here we would like to know how many photons there will be in each discrete quantum measurement. Each probing photon can be thought of approximately as having a time duration and a bandwidth corresponding to about the inverse of that duration. We call the parameter-less value “sec-Hz” a “temporal mode”. By multiplying the flux curve in Figure 3 by the nm/GHz curve shown below it, we can find how many photons/temporal-mode-m^2 to expect. We show such values for a magnitude 10, V-band object in Figure 17.

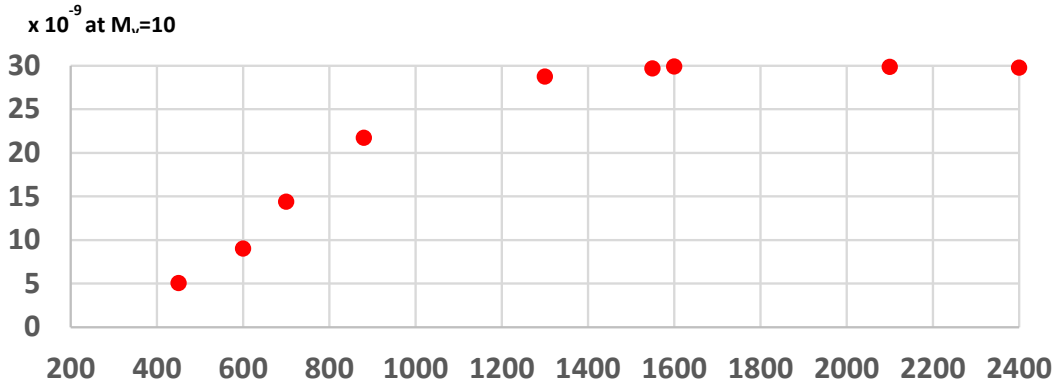

Figure 17. Photons/m^2/temporal mode vs. wavelength (in nm) for a 10-th magnitude object (through atmosphere).

What we observe is that, even for a relatively bright 10-th magnitude object, and in the V-band, there will be fewer than one photon in 10^8 temporal modes in a square meter of collector. It is important to underline that this value is independent of the bandwidth over which any measurements are made—it is an intrinsic photon rate per mode, and can only be increased by having a larger receive aperture.

It is fair to say that it would take some very excellent engineering to build a system that does not make errors or noise that might degrade the system at the level of -80 to -90 dB.

We also observe that a telecom wavelength measurement system will detect about three times more photons per measurement than a V-band measurement. This certainly suggests that the large technology base of the telecom bands might actually lead to better designs than the present-day visible-bands systems.

7.3.1 The KBdGL Approach

Motivated by the technological difficulty of probing many THz of bandwidth with the GJC approach, one probe photon at a time, Khabiboulline et al. ([3], [4], called KBdGL here) have proposed using quantum memories as storage and compression systems acting directly on the sky photons. Their idea actually consists of four separate ideas

1. An array of coherent quantum memories for coherently storing the sky photons
2. Disseminated quantum GHZ states for heralding the presence of a sky photon in the array
3. Quantum logic for compressing the stored photon information
4. Quantum Fourier Transforms on the stored (quantum) fields to create the image

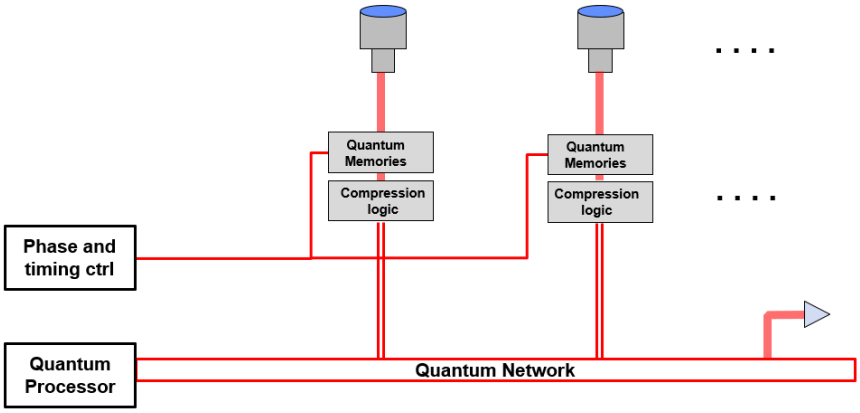

Figure 18. KBdBL architecture.

We will investigate each of these in turn. We can see that this approach is a kind of local/non-local hybrid, in that the phase-referenced signal-captures happen locally, but the captured signals—and not their measurements—are then teleported to be processed non-locally to form the image.

The KBdGL approach 1 – Coherent quantum memories

In each time bin, the optical outputs of all the telescopes are to be simultaneously and coherently stored in local quantum memories. The act of capturing and storing the photons must be controlled by a disseminated phase-controlled signal that assures that the telescope delays are correctly accounted for. That is, the control of the memory array must be as good as classical OVLBI fringe-tracking.

We will see that these captured states, stored in ionic, atomic, or some other memory modality, can either be subsequently processed in a quantum computer as qubits or can be read out optically for further processing. Any such optical processing would likely also require a transformation in wavelength or bandwidth.

The KBdGL approach 2 – GHZ states for array heralding

In both the GJC and the KBdGL approach, we have seen that there are very few time-frequency bins with sky photons. One way to reduce the amount of further processing or the size of required memories in KBdBL would be to somehow herald only those time bins that have a photon somewhere in the array, but without announcing where. To this end, and similar to the W-state approach used by GJC, KBdBL propose disseminating an M-mode GHZ state,

$$|\varphi\rangle = \frac{1}{\sqrt{2}}\left[|0000\ldots\rangle + e^{j\delta_1}|1111\ldots\rangle\right] \tag{16}$$

We will first examine its performance in a pairwise architecture; i.e., M=2. (See Appendix 9.) If we first use the stored sky qubits as the controls in local controlled-phase (CZ) quantum logic gates against this disseminated GHZ state, and then apply a Hadamard transformation to the possibly transformed state, (see Figure 19) we find that any zero-photon (or two-photon) term produces an even count across the two telescopes, but the single-photon term produces an odd count. So by using classical communication of the two measured outputs, we can deduce (i.e., herald) whether the sky photon appears in one or the other of the two telescope qubit memories in that time bin, but leaving the sky photon in their memories.

Both the similarities of and differences between the GJC and the KBdGL approaches are depicted in Figure 19. The GJC's W-state heralds a photon, but then measures it. The KBdGL's GHZ-state heralds a photon in the array, but does not destroy the sky qubit.

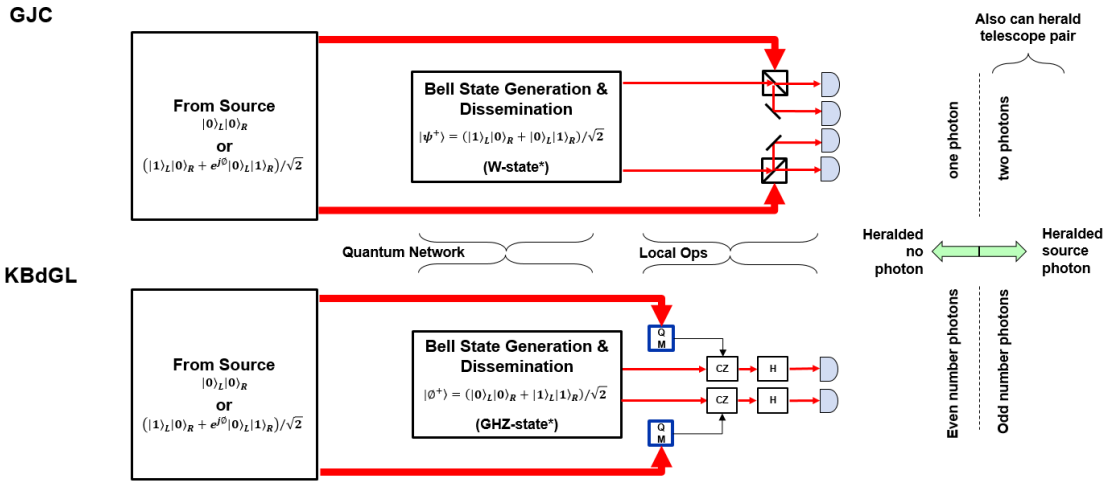

Figure 19. Comparison of the GJC and KBdGL heralding approaches.

The KBdGL approach 3 – Memory compression using quantum logic

Although the heralding approach of the previous section could allow us to greatly reduce the number of remaining qubits for further processing, it still requires transmitting a GHZ state in every time bin, which we know is a gigantic number. To this end, KBdGL invented a means of greatly compressing the number of qubits for which we would need disseminated GHZ states.

As depicted in Figure 20, we start with the pre-knowledge that there will be only a single photon in K time bins. As described in Appendix 10, a $\log_2(K+1)$ memory bank at each telescope can then be used to encode and store both the array photon and the address of the time slot in which it arrived.

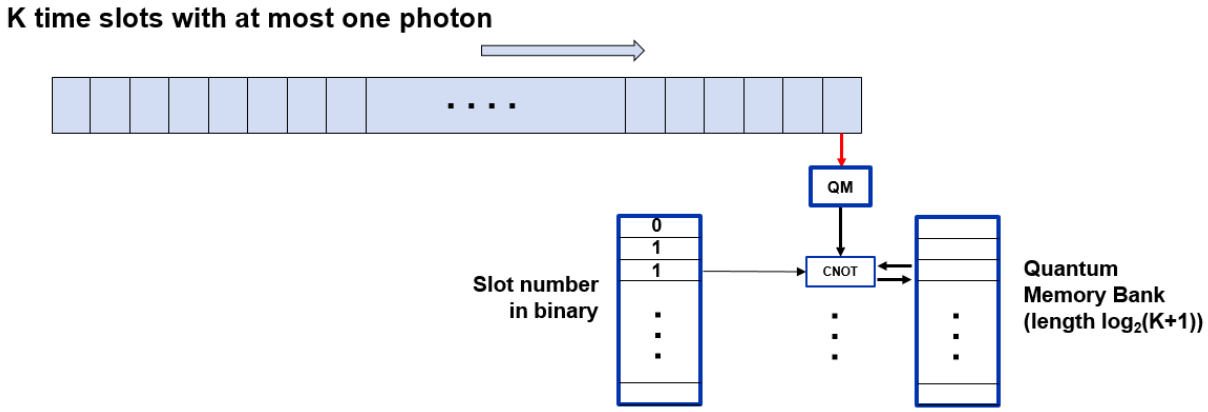

Figure 20. KBdGL data compression architecture.

Therefore, after the K slots have been examined, only $\log_2(K+1)$ states remain in memory. Thus $\log_2(K+1)$ GHZ states need to be disseminated to herald the fact of a photon from these K slots and also to learn in which time bin it fell. (As described in the Appendix, we need to know in which time bin it fell because part of the quantum logic processing sometimes flips the sign of the qubit. Knowledge of the time bin address allows us to correct the sign flips.) As by design, this number of GHZ states would be much much less than K. For instance, for K=1,000,000, we have that $\log_2(K+1)=20$. We must note, though, that 20,000,000 logic gates would need to have been operated to perform the compression. And although they are only local gates, that is still a lot of quantum processing. (See Appendix 10 for details on the processing.) And remember that our OVLBI system will need to measure tens to hundreds of THz of bandwidth.

After GHZ-heralding, the array photon would then be teleported from all M telescopes to a central quantum processor.

We know that creating and successfully disseminating a large GHZ state is quite complex. A simpler approach we now present might be to disseminate only $\log_2(K+1)$ Bell *pairs* to each telescope and teleport the entire $\log_2(K+1)$ memory bank from each telescope to the central processor. Those could be telescope-independent processes. At the central processor, it would then be much easier to perform the GHZ heralding locally.

The KBdGL approach 4 – Quantum Fourier Transforming of the fields

In their papers, KBdGL pointed out that the stored, memory-compressed, and heralded qubits can, similar to GJC, be used to produce pairwise correlations, using a disseminated W-state. These correlations could then be processed to form an image following the vC-Z theorem.

However, since it is a representation of the field across the entire array that is really stored, one could, instead, apply a 2D Inverse Fourier Transform to those states, as shown in equations (8),(9). Furthermore,

KBdGL propose applying this directly to the qubits as a Quantum Fourier Transform (QFT)—that is, one would first teleport the array states for each time bin in the coherent memories to a central processor. Then, a quantum processor would perform the QFT operator, and the outputs would be detected to form the image (see Figure 10.) Although we will see that this approach gives a much-improved SNR, we also see that it requires the quantum computer to perform a new QFT for each heralded photon.

We will investigate more deeply the QFT and other field-processing in the sequel.

This page intentionally left blank.

8. PERFORMANCE ANALYSIS RESULTS

We now investigate the performance of the several architectures we have introduced. For each architecture, we first find the SNR of pairwise measurements of the complex visibility. We then investigate the SNR of the calculated dirty images. Most of the details can be found in the Appendices.

8.1 PAIRWISE MEASUREMENT SNR – CLASSICAL DIRECT DETECTION

As we show in Appendix 6, a classical OVLBI interferometer, as depicted in Figure 13, integrates the correlation of the delay-compensated signals for a time period, and then subsequently integrates the correlation of the signals with one of them phase shifted by 90 degrees for a second period. Each measurement takes the difference of the two detector outputs shown in the figure, and the two 90-degree offset (I&Q) measurements are combined (see (A6-3)) to form an estimate of the complex correlation. We show in (A6-7) that this direct detection correlation estimate has SNR

$$SNR\hat{g}_{nm,DD} = \frac{|\langle \hat{g}_{nm} \rangle|^2}{Var\hat{g}_{nm}} = \frac{T}{2}\{\mathcal{N}_S R_S(0)\} \left| \int \; d^2\boldsymbol{\alpha} \; \tilde{I}_s(\boldsymbol{\alpha}) e^{j2\pi\left[\frac{(\boldsymbol{\rho_n}-\boldsymbol{\rho_m})}{\boldsymbol{\lambda}}\right]\cdot\boldsymbol{\alpha}} \right|^2 \qquad (17)$$

where the term in brackets, with $\mathcal{N}_S$ being the source's apparent brightness, describes the total in-band photon flux received in each aperture, T is the total integration time, and the last term is the source distribution's Fourier Transform, calculated here in angular coordinates (see Appendix 1).

This calculation assumed that all the optical power in each of the two telescopes was used for this calculation, and that the transmission was lossless. A full performance metric will also include:

1. Loss due to using each telescope's output to perform multiple simultaneous pairwise correlations. If there are N telescopes, we can imagine splitting each output into as many as (N-1) signals, each supporting a pairwise correlation. For a fixed time, such splitting would reduce the pairwise SNR by a factor of (N-1).
2. Loss due to lossy transmission media between the two telescopes and the interferometer. If we model both arms as having the same loss, we find that the SNR is degraded by exactly that power loss. (For different losses, the SNR loss is the geometric mean of the two losses.)
3. Loss, η, due to non-unit-efficiency detectors. As the outputs of the two detectors are only subtracted, we find that the SNR reduces as η.

8.2 PAIRWISE MEASUREMENT SNR – CLASSICAL HETERODYNE

We show in Appendix 7 that a heterodyne system calculates a correlation with SNR

$$SNR\hat{g}_{nm,het} = \frac{\left|\langle \hat{g}_{nm,het} \rangle\right|^2}{Var\hat{g}_{nm,het}} = 2r\, \mathcal{N}_S SNR\hat{g}_{nm,DD} \tag{18}$$

The factor of 2 comes from the classical system's need to make two separate measurements for I and Q. (In the case of non-unity detection efficiency, η, there will also be two factors of η in this balanced heterodyne system, and only one in the vC-Z approach.) The value r is the ratio of the total measurement bandwidths. The bandwidth allowed by a single heterodyne system is likely only a few to tens of GHz. To match the total bandwidth of a classical system, (i.e., to get r=1) hundreds to thousands of parallel heterodyne systems would need to be operating.

The big intrinsic difference, though, is the $\mathcal{N}_S$ term that is the apparent brightness of the sky object, as measured by a telescope, with units photons/sec-Hz (or photons/mode.) We showed earlier that a 10th magnitude object, through the atmosphere, delivers fewer than 10^{-8} photons per mode in the V-band. Heterodyne measurement SNR is thus *much* less than the SNR with the direct measurement approach, at least in the optical bands of interest to us.

8.3 PAIRWISE MEASUREMENT SNR – GJC

As we discuss in Appendix 8, the pairwise GJC architecture, depicted in Figure 14, sends an entangled qubit to the two telescopes, where, in its photonic form, it is interfered with a single temporal mode of the sky signal. We can model either the transmitted photon version or the transmitted qubit version, (where the qubits are then locally translated to photons,) using the same approach. In Appendix 8, we analyze this with a full quantum operator approach and find:

$$SNR\hat{g}_{nm,GJC} = \frac{T_M(\mathcal{N}_S R_S(0))}{2}\left\{\frac{d_f {M_t}^2}{2}\right\}\left|\int d^2\boldsymbol{\alpha}\ \tilde{I}_s(\boldsymbol{\alpha}) e^{j2\pi\left[\frac{(\boldsymbol{\rho_n}-\boldsymbol{\rho_m})}{\boldsymbol{\lambda}}\right]\cdot\boldsymbol{\alpha}}\right|^2 \tag{19}$$

where $d_f = t_s/T_p$ is the single photon source's duty factor, and

$$M_t \equiv \frac{\int_{-\frac{t_s}{2}}^{\frac{t_s}{2}} dt \int_{-\frac{t_s}{2}}^{\frac{t_s}{2}} du\, \phi(t) R_S(t-u) \phi^*(u)}{t_s R_S(0)} \tag{20}$$

is the temporal mismatch factor between the single-photon source's temporal mode and the temporal characteristics of the sky photons arriving at the telescopes. Our model of the GJC on-demand photon source is

$$\hat{E}(t) = \sum_{m=0}^{M-1} \hat{a}_m \, \phi\left(t - mT_p\right) + \widehat{vacuum} \tag{21}$$

where $\hat{a}_m$ is the photon annihilation operator for that field's excited modes; $\phi(t)$ is a unit-normalized temporal-mode function time-limited to $|t| \leq t_S/2 \leq T_p/2$ where T_p is the pulse repetition period; and $M = T_M/T_p \gg 1$ is assumed to be even (so an integer number of pulses fall in both the I and Q measurement periods).

We note the second 2 in the denominator of the SNR that comes about because of the 50% chance that the two photons fall on the same side. As we discussed, this factor could possibly be improved with dissemination of a multi-mode W-state.

Similar to the classical case, any non-repeatered transmission of the single photon will incur a further loss that directly reduces the SNR. Different from classical, though, is the fact that GJC requires two simultaneous photon measurements, so this SNR is actually reduced by η^2 where η is the detection efficiency of a single detector.

We can design $\phi(t)$ to maximize M_t by examining (20), which is a standard Fredholm integral, known to be optimized if we expand $R_S(t)$ as a sum of orthogonal functions and then select $\phi(t)$ to be that function corresponding to the largest eigenvalue, all of which are known to be positive. M_t is then the ratio of this largest eigenvalue to the sum of all the eigenvalues, and $M_t \leq 1$.

The SNR for GJC is thus strictly smaller than the classical version by $\eta \frac{d_f M_t}{2}$, if the transmission losses are the same. (Depending on the complexity of the electro-optical circuits used to maximize this factor, we would guess that $d_f M_t$ would likely result in at least several decibels of loss.) For this performance hit and huge complexity, GJC would only be worth considering if the classical version has lossy transmission and we could design a low-loss (or even lossless) quantum network delivering the GJC qubits at rate, followed by translating them into well-matched photons.

This page intentionally left blank.

9. IMAGE CREATION

So far, we have shown the relationships between our desired images and the signals we need to capture or measure. We have investigated several means of making these measurements and have examined their SNR performance.

We will now look more closely at the processing of those measurements to create the dirty image. First we will look at the vC-Z approach, based on measurements of correlations/visibilities. Then, we will examine the direct processing of the optical fields, both via the quantum memories and then more directly.

9.1 CORRELATION-BASED IMAGE CREATION

We have examined a number of architectures for measuring correlations between signals arriving at pairs of telescopes in the array: classical direct detection, classical heterodyne, classical intensity interferometry, quantum enabled GJC-style, and quantum enabled KBdGL-style. Each of these methods produces a set of complex numbers we denoted as $g\left(\frac{\Delta x_{jk}}{\lambda}, \frac{\Delta y_{jk}}{\lambda}\right)$ in (5) which are the "visibilities" or the complex correlations between the signals as seen at telescopes j and k. We would like to perform their Inverse Discretized Fourier Transform as in (6)

$$\tilde{\tilde{I}}_s(\hat{\xi}, \hat{\eta}) \approx \frac{1}{N^2} \sum_j \sum_k g\left(\frac{\Delta x_{jk}}{\lambda}, \frac{\Delta y_{jk}}{\lambda}\right) exp\left[-j2\pi\left(\frac{\Delta x_{jk}}{\lambda}\hat{\xi} + \frac{\Delta y_{jk}}{\lambda}\hat{\eta}\right)\right] \tag{22}$$

As we pointed out, for N telescopes, there are as many as $\binom{N}{2}$ unique pairs. However, depending on the geometry of the array, some pairs may actually have the same baselines as others—both in distance and angle—and can be considered redundant.

At this point, we must admit that making completely general statements about image creation performance is difficult because exact formulas depend on the array layout, the set of baselines measured, and the resultant dirty image itself. For our calculations, we will presume a square KxK filled array with telescopes equally spaced. (We note that such an array includes many redundant baselines.) We then show in Appendix 11 that the SNR of a 2-D image at grid point $\boldsymbol{j}$ in the calculated dirty image estimate for the classical vC-Z measurements is

$$SNR_C(\boldsymbol{j}) = \frac{K^6 T}{2(K^2-1)^2}\{\mathcal{N}_S R_S(0)\}\mathcal{I}(\boldsymbol{j})^2 \tag{23}$$

where $\mathcal{I}(\boldsymbol{j})$ is the dirty image at grid point $\boldsymbol{j}$ and which is normalized as $\sum \sum_{\boldsymbol{j}} \mathcal{I}(\boldsymbol{j}) = 1$. We recall that a Gaussian-shaped spectrum gives $R_S(0) = \frac{1}{2\sqrt{\pi}t_S}$ where t_S is the coherence time of the source (psec-class).

The SNR for the GJC approach is shown to be smaller than this by the bracketed term found in (19)

$$SNR_{GJC}(\boldsymbol{j}) = \frac{K^6 T}{2(K^2-1)^2}[\mathcal{N}_S R_S(0)]\left\{\frac{d_f M_t^{\,2}}{2}\right\}\mathcal{I}(\boldsymbol{j})^2 \tag{24}$$

Losses due to signal transmission and non-unit-detection efficiency further decrease these SNRs.

9.2 ARRAY GEOMETRY REQUIREMENTS

Before we examine field and Quantum Fourier Transforms, we will examine the mathematics of what we have been calling Inverse Discretized Fourier Transforms. As we stated, we can numerically calculate this double summation exactly

$$\tilde{\tilde{I}}_s(\hat{\xi},\hat{\eta}) \approx C\sum_j\sum_k g\left(\frac{\Delta x_{jk}}{\lambda},\frac{\Delta y_{jk}}{\lambda}\right)exp\left[-j2\pi\left(\frac{\Delta x_{jk}}{\lambda}\hat{\xi}+\frac{\Delta y_{jk}}{\lambda}\hat{\eta}\right)\right] \tag{25}$$

with *arbitrary* placements of telescopes and the summations being over the j=0,1…..,K-1; k=0,1,…. K-1 positions. For many telescopes, though, we would wonder if we could use a 2-D Discrete Fourier Transform (DFT) which is known to have a fast algorithm for implementation (i.e., the Fast Fourier Transform, the FFT.) The DFT could be applied if all the baselines fell on a grid, and that would be possible if the antennas themselves were positioned on a grid, perhaps with some or many grid points left empty. That is, suppose

$$\frac{\Delta x_{jk}}{\lambda} = \frac{(x_j - x_k)}{\lambda} \equiv (n_j - n_k)\Delta_x;\ \ \frac{\Delta y_{jk}}{\lambda} = \frac{(y_j - y_k)}{\lambda} \equiv (m_j - m_k)\Delta_y \tag{26}$$

where telescope j is positioned at $(n_j\Delta_x, m_j\Delta_y)$, with (n_j, m_j) being integers. Let us similarly discretize the image plane (i.e., the tiny angles describing the source intensity function) as

$$(\hat{\xi},\hat{\eta}) = (l\Delta_\xi, r\Delta_\eta) \tag{27}$$

If we can design the system so that

$$\Delta_x\Delta_\xi = \Delta_y\Delta_\eta = 1/K \tag{28}$$

and where $0 \le n_k \le K-1$ and $0 \le m_k \le K-1$

then we can rewrite the phasor in (25) as

$$exp\left[-\frac{j2\pi}{K}\left((n_j - n_k)l + (m_j - m_k)r\right)\right] \tag{29}$$

which can be seen to be the elements in a 2-D DFT phasor. (We will also change the constant out front to be $\left(\frac{1}{K^2}\right)^2$.) We need to remember to include 0s on those grid points where there are no telescopes.

To fully show the 2-D nature of this DFT, we rewrite (25) as (with an obvious reformulation of both the visibilities and the image, and this time, summed over dimensions instead of telescopes)

$$\tilde{I}_s(l,r) \approx \frac{1}{K^4}\sum_{n_x=0}^{K-1} exp\left[-\frac{j2\pi}{K}n_x l\right]\sum_{n_y=0}^{K-1} exp\left[-\frac{j2\pi}{K}n_y r\right]\sum_{m_x=0}^{K-1} exp\left[\frac{j2\pi}{K}m_x l\right]\sum_{m_y=0}^{K-1} exp\left[\frac{j2\pi}{K}m_y r\right] g(n_x - m_x, n_y - m_y) \tag{30}$$

where we see that vC-Z is really equivalent to four 1-D (I)DFTs, although only $\binom{N}{2}$ terms will be non-zero. If our KxK grid is filled ($N = K^2$,) then there are $\frac{K^2(K^2-1)}{2}$ terms.

Since we are allowed to choose $\Delta_x \neq \Delta_y$, we note that we can use this approach to model some telescope arrays that do not fall on square grids. For instance, OVLBI arrays are sometimes placed on triangular grids. We know that triangular grids have points on $1, 2, and\ \sqrt{3}$ grid spacings, so, if we do not mind having the angular resolutions in the image be different in the two dimensions, we can use such an approach.

There are also variants of the 2-D DFT, such as over hexagonal regions ([32] or other shapes ([33],[34],[35].)

Finally, we note that we can always define a large sparse grid where the arbitrary telescope placements fall very near grid points. Such an approach could accommodate an arbitrary geometry, but might require many more calculations.

Remember, though, that the vC-Z approach does not require any DFTs or regular grids, since we can always calculate (25) exactly. This DFT discussion is only relevant if efficient or fast calculations are needed.

9.3 FIELD-BASED IMAGE CREATION

We now turn our attention to the 2-D transform required for the field transformation approach (equation (8)):

$$\tilde{\tilde{E}}_s(\hat{\xi},\hat{\eta},t) \approx \frac{1}{N}\sum_k E_k(t)\, exp\left[-j2\pi\left(\frac{x_k}{\lambda}\hat{\xi}+\frac{y_k}{\lambda}\hat{\eta}\right)\right] \tag{31}$$

where the single summation here is over the telescopes. If the fields, E_k, have been measured and digitized, such as in a heterodyne system, then this summation can be numerically calculated exactly, as in the previous discussion. Also similarly to above, if the array positions fall on a grid, we can transform this equation to a 2-D DFT (where $E(j,k)$ is the field at grid point j,k which we may have to fill with zero.)

$$\tilde{\tilde{E}}_s(r_x,r_y,t) \approx \frac{1}{K^2}\sum_{m_y=0}^{K-1} exp\left[-\frac{j2\pi}{K}m_y r_y\right]\sum_{m_x=0}^{K-1} exp\left[-\frac{j2\pi}{K}m_x r_x\right] E(m_x,m_y) \tag{32}$$

As above, this version sums over dimensions. This equation shows us explicitly that a 2-D DFT is usually performed with K 1-D transforms in x, and then K 1-D transforms in y, as depicted in Figure 21.

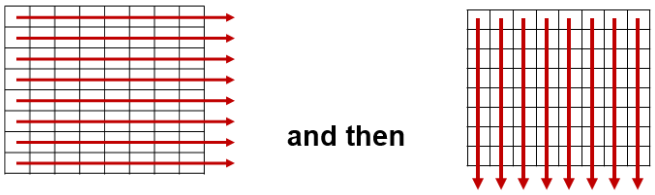

Figure 21. Performing a 2-D DFT with multiple 1-D DFTs.

We note now, though, that if we define

$$m \equiv Km_x + m_y;\ \ and \quad\ r \equiv r_x + Kr_y \tag{33}$$

which is inverted as

$$m_y = m_{modK};\ \ m_x = \frac{m - m_{modK}}{K}\ ;\ r_y = r_{modK};\ r_x = \frac{r - r_{modK}}{K} \tag{34}$$

we see that the multiple 1-D DFTs can be replaced with a reordering and then a single, size K^2 1-D transform as

$$\tilde{\tilde{E}}_s(r,t) \approx \frac{1}{K^2}\sum_{m=0}^{K^2-1} exp\left\{-\frac{j2\pi}{K^2}[(m-m_{modK})r_{modK} + m_{modK}(r-r_{modK})]\right\} E\left(m_{modK},\frac{m-m_{modK}}{K}\right) \tag{35}$$

Although this is not a standard DFT, it is a related unitary transformation (see Figure 22).

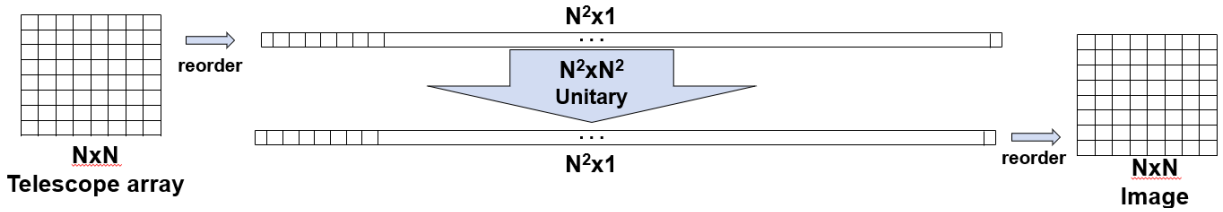

Figure 22. Transforming a 2-D DFT into a larger 1-D transformation.

KBdGL have suggested that the fields, as captured as qubits, could be transformed using the Quantum Fourier Transform (QFT). (We note that classical transforms would pad the data with zeros for missing components. In the quantum realm, we would need to fill empty grid slots with vacuum signals.) If we teleport the (already heralded) time bin of the telescope array to a central place, we can then perform the QFT on this joint, one-photon state. We know that the density operator for this K^2 – mode state is written (see Appendix 12)

$$\hat{\rho} = \frac{1}{K^2} \sum_{n_x=0}^{K-1} \sum_{n_y=0}^{K-1} \sum_{m_x=0}^{K-1} \sum_{m_y=0}^{K-1} g\left(n_x - m_x, n_y - m_y\right) |1_{n_x,n_y}\rangle\langle 1_{m_x,m_y}| \tag{36}$$

where we let $\left\{\left|1_{n_x,n_y}\right\rangle\right\}$ be the tensor product of all K^2 qubit states on the grid (in arbitrary order for now) but with the very specific one defined by 2-D grid point n_x, n_y containing exactly one photon, and the rest vacuum.

A 2-D QFT (which is a unitary operator) in this basis can be written

$$\hat{U}_{QFT} = \frac{1}{K} \sum_{n_x=0}^{K-1} \sum_{n_y=0}^{K-1} \sum_{m_x=0}^{K-1} \sum_{m_y=0}^{K-1} exp\left[-\frac{j2\pi}{K}\left(n_x m_x + n_y m_y\right)\right] |1_{n_x,n_y}\rangle\langle 1_{m_x,m_y}| \tag{37}$$

It is shown in Appendix 12 that the density of the output after applying the operator is

$$\hat{\rho}_{output} = \hat{U}_{QFT} \hat{\rho} \hat{U}_{QFT}{}^{\dagger} \tag{38}$$

It is this state that we will measure, and whose diagonals give the image values. We show this in the Appendix as

$$\langle 1_{l_x,l_y}|\hat{\rho}_{output}\left|1_{l_x,l_y}\right\rangle = \tag{39}$$

$$= \frac{1}{K^4}\sum_{n_x=0}^{K-1}\sum_{n_y=0}^{K-1}\sum_{m_x=0}^{K-1}\sum_{m_y=0}^{K-1} \quad exp\left\{-\frac{j2\pi}{K}\left[(n_x-m_x)l_x+\left(n_y-m_y\right)l_y\right]\right\}$$

$$x\ g\left(n_x-m_x,n_y-m_y\right)$$

We can see that this is exactly the same dirty image as the one that formed from the correlations (see (30)).

To implement this QFT, we can use the multiple 1-D QFT approach as shown in Figure 21. However, we predict that it will be easier to perform the reordering of (33)-(34) and then apply a single size-K^2 unitary transformation shown in (35) and Figure 22 , which is also relevant to the QFT.

(If it is of interest, it can be shown that the hexagonal-based FT of Mersereau ([32]) is a unitary transformation.)

Before we leave this section, we return to the design of the array. Although the digital, correlation-based approach can deal with arbitrary telescope placements, any approach that requires the transformation to be unitary, such as the QFT one, puts constraints on the placements. Typically, there must be a regular grid. A number of authors have investigated non-standard spacing, however (see, e.g., [32]-[37]).

9.4 FIELD-BASED IMAGE PERFORMANCE

It is shown in Appendix 11 and 12 that the SNR for the KBdGL field-based approach is (for large K)

$$SNR_{KBdGL}(\boldsymbol{j}) = \frac{T\mathcal{N}_S K^2}{2\sqrt{\pi}t_S}\mathcal{I}(\boldsymbol{j}) \tag{40}$$

which at first glance seems to be similar to the GJC SNR, although it does not suffer the extra 3 dB penalty. (Note we have omitted here the transmission losses, detector efficiency, and the temporal mismatch factor.) *However*, importantly, we see that the magnitude term including the normalized image is not squared in this architecture. Thus, in our KxK image, the KBdGL SNR is on the order of K^2 times *bigger*. A similar performance improvement was predicted by KBdGL.

(We can note here that KBdGL demonstrated their QFT algorithm on a *linear*, equally spaced array. Although it correctly suggested some properties of their approach, it sidestepped many of the important details we have investigated here.)

The processing depicted in the bottom of Figure 10, then, has the potential of being much more efficient in terms of SNR produced with a fixed number of photons. As we pointed out, though, it requires a QFT processing step for each photon that is captured, as opposed to a single DFT processor at the end of the correlation measurements. A real system would need to trade off the extra complexity with the improved

performance. (Of course, the need for quantum memories and GHZ-based heralding would already add huge amounts of complexity.)

9.5 QUANTUM-INSPIRED CLASSICAL FIELD-BASED IMAGE CREATION

The great performance improvement from field-based processing motivates us to question whether there is a simpler, classical analog. The answer is "yes." It is straightforward to show that we would get the same field-based image performance if we could perform the 2-D Fourier Transform directly on the received optical fields. That is, we would transmit the received fields from the telescopes, (see Figure 23) through delay-equalized paths, to a central processor where Fourier Transform phases would be applied, as in (7). (Similar to the quantum approach, empty grid positions would need to include vacuum signals.)

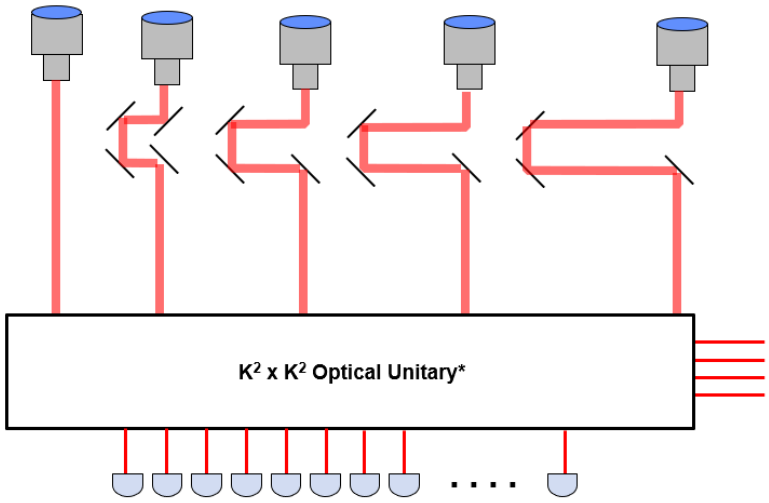

Figure 23. Quantum-inspired classical field transforming.

We note that the "hypertelescope" concept ([26]) does something very similar. Beams are sent to a central processor where they are, as a group, fed through a lens to form an image, simulating as if they had all been received in one telescope. People have investigated various geometries with such an approach.

What we propose here matches well into the new technology of Photonic Integrated Circuits (PICs,) which have been created to, among other things, implement arbitrary unitary transformations on banks of optical signals using modulators and beamsplitters. Our K^2 reordering and unitary transformation concept, depicted in Figure 22, is directly relevant since the PIC can be configured to implement an arbitrary unitary operator. There has been recent work on architectures for photonically implementing arbitrary unitary transformations. ([38],[39]; see Figure 24.) Also, a photograph of a PIC performing a unitary transformation is shown in Figure 25.

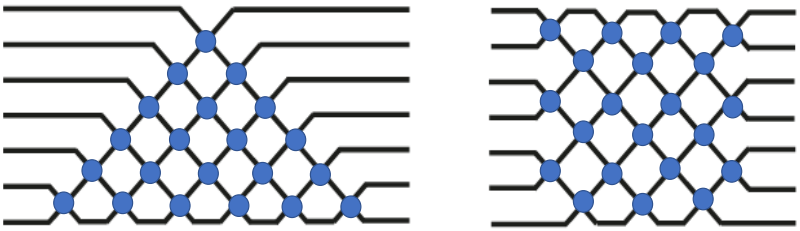

Figure 24. Two approaches for implementing a unitary transformation on a PIC. A blue dot corresponds to a beam-splitter-phase-shifter element. Different factoring approaches to the unitary matrix result in the different architectures. See [38], [39].

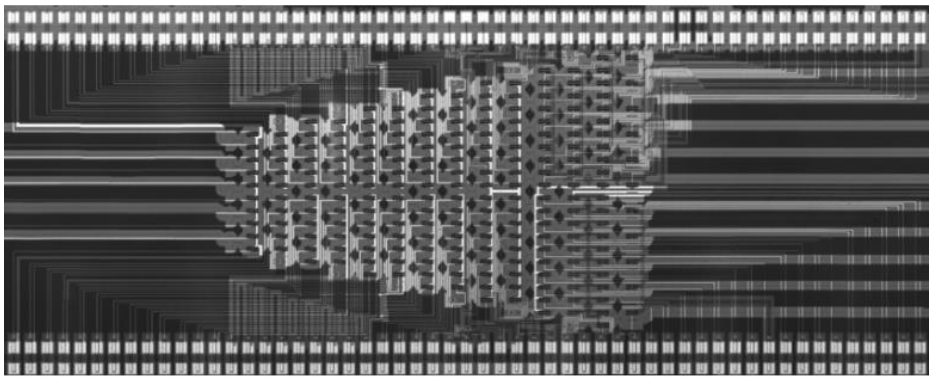

Figure 25. Example Photonic Integrated Circuit of an optical interferometer array. (Taken from [40])

We do recall, though, that lossy transmission of the weak signals was a motivation to investigate the quantum approach in the first place, and this classical technique would suffer those. Whether the improved performance would be worth it is TBD.

We observe that the KBdGL quantum memory-based approach could also, after its heralding step, coherently transform the stored states back to optical signals and transmit and process them in this classical, PIC-based way, thus precluding the need for a quantum processor performing QFTs. We also remember that adequately large memories would allow us to remove the need for physical delay equalization, so using the memory and heralding approach with an optical follow-on could possibly lead to an interesting architecture.

9.6 TURBULENCE AND CALIBRATION

A very real problem remains, in that these mathematical formulas so far presume that the telescopes all have the same undistorted view of the object and that their optical systems are identical. In fact, terrestrial telescopes separated by even small distances look through air paths seeing different turbulence (and thus

piston and tilt, leading to phase errors, as well as different higher-order aberrations) and they and their transmission media might even have somewhat different optical responses.

In 1958, Jennison ([12]) showed how redundancy in the correlation measurements taken on the array could be used to solve for and then mathematically remove the unwanted distortions. More recently, others ([41]-[44]) have generalized the technique, but they, too, depend on measured correlations, each of which has been affected by two telescopes and their optical paths.

In the field-transform approach, which we further examine in Appendix 13, we can try to include the effects of telescopes by alternately learning them and then measuring the density matrix and correcting its QFT by applying a telescope-based operator (see (A13-2)). The learning step, though, will either be a correlation-based measurement of pairs of telescopes from the fields, or some TBD optical reference-based calibration and learning phase.

In either case, not making intrinsic redundant measurements, as the correlation method can, forces us to add complexity to any field-transform method. However, the potential for higher SNR in the field-transform approaches should motivate the community to investigate this path.

This page intentionally left blank.

10. SIZING/PERFORMANCE EXAMPLES

We are interested in assessing the difficulty of implementing some of these approaches. To that end, we repeat here the flux curve shown earlier, along with some telecom-wavelength bands. This time, we also show some bandwidths in Hz., and see the frequency distortion inherent in a wavelength-based spectrum.

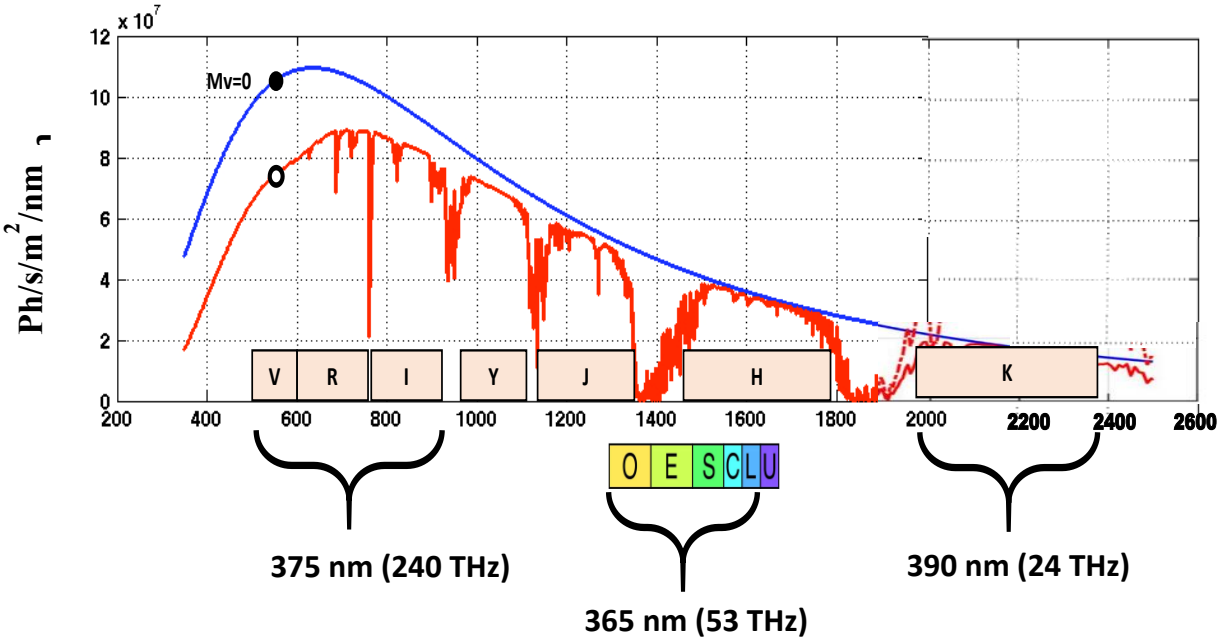

Figure 26. Flux density and some relevant processing bands. The colored bands are the widely used optical fiber bands.

Suppose we aim to process 20 THz of bandwidth, possibly in the H or K bands, which can be seen to be the kind of bandwidths that a classical, full-band system might enable. In Figure 17, we can see that a 10th magnitude object would be delivering (through the atmosphere) 3 x 10^{-8} photons per mode per meter-squared (in those bands.) A 20 THz processor, then, would be receiving 600 photons per millisecond per meter-squared of aperture.

We first examine the GJC approach.

Suppose our goal is to build an array with a maximum transmission loss of 2 dB. (For, say, a 5 kilometer baseline and variable-length telecom fiber transmission.) The quantum network would need to transmit about 1.5 x 20 = 30 THz of entangled qubits to each telescope for each pairing (which includes the

extra rate to make up for the transmission loss). Aiming for 10 GHz operation of an individual quantum network, that would mean we would need 3000 parallel repeatered channels (parallelism possibly at least partly via WDM.) The total number of quantum channels for the array then needs to further grow to service all the telescopes as well as each of the pairings. Each of these channels would require quantum memories at both ends in order to implement the lossless repeater function via heralding. (The memory requirement may mean that the bandwidth of each repeatered quantum network would likely be forced to be much lower than 10 GHz, but we will proceed for now. See Section N.) In fact, to achieve the heralding, there would also need to be a classical comm system for each quantum network, operating at a rate proportional to 30 THz (although coding of that information could reduce the required rate, at the cost of some delay.) Finally, we remember that each measurement will have a success probability of only about Nx3 x 10^{-8} if we assume N 1-meter-diameter telescopes.

Next, suppose we tried to build a KBdGL system for an array of, say, eight telescopes. With near-term quantum memories, we might envision 100 MHz operation. (See Section N.) Our 20 THz measurements thus mean we would need 200,000 WDMed memories at each telescope. (We might need to wavelength-convert the incoming photons in each of the 200,000 channels in order to be able to utilize a single fixed memory technology.) See Figure 27 for a much-simplified illustration of such a system.

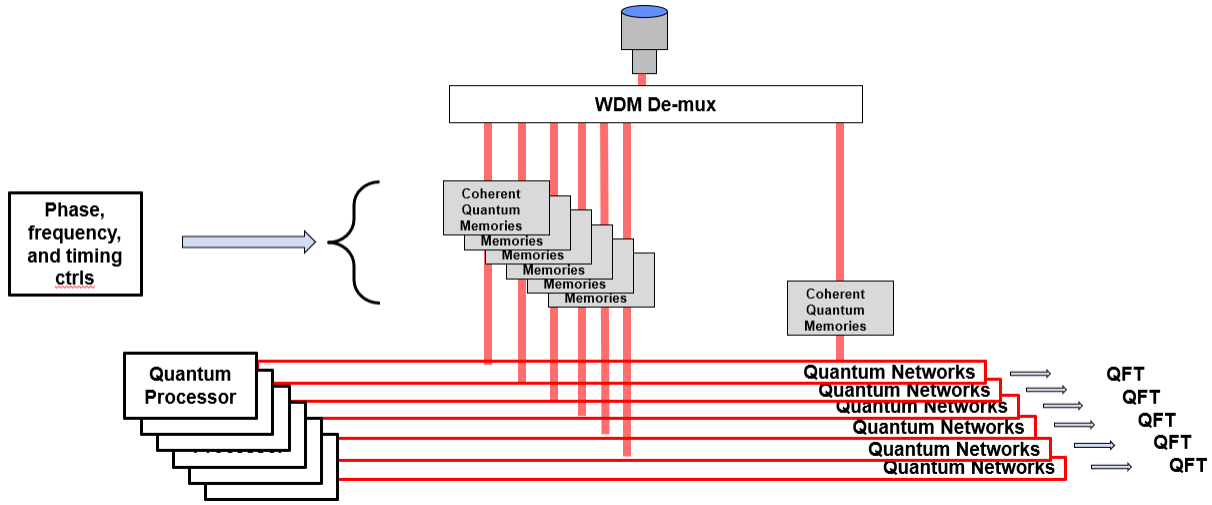

Figure 27. Depiction of a parallel quantum network construction of a KBdGL system. Such a system would need to have all the array telescopes on it.

Our array of eight telescopes (assume 1-meter) would thus be seeing 4.8 photons/microsecond, or 24 photons/sec-channel. That is about 40 msec between photons in each channel. That is somewhat beyond the state of the art of memory duration today, so let us choose 1 msec to define a bank of 100,000 cells for

each channel. That would compress to 17 cells, but would only detect a photon every 40th block. (Remember, though, that there would be 200,000 of these running in parallel.)

The quantum logic would need to run at 17x100 MHz = 1.7 GHz in each channel (or perhaps only 100 MHz in some kind of pipelined architecture.) The GHZ states would then need to be delivered by the quantum network at 17 KHz (to the complete array of eight, here, and to each of the 200,000 channels.) Successful heralding (that is, the photon arrival rate) then sets the required teleportation rate. The heralding subsystem would need a parallel classical communication system running at similar rates.

Once teleported, each photon would have a QFT applied. These would then be detected and all the time slots and parallel channels would then be integrated up.

If we were to implement, instead, the variant we proposed earlier, we would not transmit any GHZ states, but would teleport the full 17-block by transmitting a two-mode Bell state for each memory cell. That would require the transmission of the same number of Bell pairs as GHZ states, and would then require 17 times more teleportations. However, it is felt that the Bell pair approach would be much less complex than the eight-mode GHZ state approach, whose dissemination details are TBD.

We can note here that there are (up to) four somewhat different types of quantum memories required for KBdGL:

- "Interface" coherent memories to catch the sky photons
- "Working" coherent memories to enable the quantum logic steps
- "Memory bank" coherent memories to store the compressed qubits and then enable the GHZ-based heralding
- Network memories to enable the lossless operation of the quantum network that is used to deliver the GHZ states and the Bell pairs for the teleportation

We will discuss these in the upcoming section dedicated to quantum memories.

Before we leave this section though, we should see if there is utility for any of these ideas if the object were particularly bright. For instance, let us examine a very bright satellite, some of which have had glints measured to be M_V at 2.0 or even brighter. If we assume we would like to build our systems near 1.55 um, we can see from Figure 26 that we would be receiving about $4x10^7$ photons/sec/nm/m^2 divided by 8 dB (6.3, for M_V=2.0) or about $6.3x10^6$ photons/sec/nm/m^2 (and this is in space, where there is no extra atmospheric loss). To match the 600,000 photons/sec/m^2 of our previous sizing, we would need to process "only" 0.1 nm (or about 12.5 GHz at our wavelength) per m^2. We can already see, though, that compared to the 20 THz required above, this value is much closer to reasonable. Furthermore, with no atmospheric time constants to worry about, we might be able to integrate longer, and thus accept much lower flux. If we processed this band using a telescope of 0.1 m^2 (i.e., approximately 32 cm) we would be receiving "only" 60,000 photons/sec/telescope, but that might actually be enough if the object and the sensor were

stable. In fact, with adequate stability, we might be able to get away with even narrower-band measurements or dimmer targets.

If this proposed performance motivated us to construct such a space-based OVLBI system, we would need to implement the time-delayed correlators (for vC-Z), but a variable delay line in space would be difficult. However, we remind the reader of the great benefit of quantum memories—the ability to implicitly create delay lines by reading out of the memories at delay-compensated times. Thus, the KBdGL approach (likely with free-space inter-satellite connections) might be worth pursuing. Remember, too, that in space, an as-yet uninvented means of correcting for turbulence would not be required.

Although this sizing is much closer to feasibility than the sizing for dim objects, with 100 MHz memories, we would still be requiring a parallel construction of 125 channels.

11. THE GJC/KBdGL APPROACHES – DISCUSSION AND SUMMARY

Let us now try to summarize our understanding of the operation of the two quantum-enabled approaches we have examined. The questions we had started out with were – do these systems:

(a) improve the SNR?

and/or

(b) allow longer baselines?

We now try to answer these questions.

11.1 (A) INTRINSIC SNR ASSESSMENT

We have shown that the intrinsic SNR performance of GJC is no better than that of the standard classical non-local, correlation-based approach. In fact, it has several extra losses unique to the single-temporal-mode approach.

Our interpretation of this approach is that it is very like a heterodyne "local" approach, except that the entangled "single-photon local oscillator" allows us to herald away all the non-productive time slots, thus giving some of the non-local benefits of heterodyne without adding nearly as much extra noise.

We then showed that the intrinsic SNR performance of KBdGL is the same as we would have in a classical field-transforming (and non-local) approach (except for the several single-temporal-mode losses we noted above.) Either of these field-transforming methods has the potential to be quite a bit more efficient than the pairwise approaches.

As we noted, however, both these field-transformation systems have the as yet unsolved problem of dealing with turbulence. They would do very well, though, in the vacuum channel of outer space. And we believe some solutions to this calibration problem can likely be devised.

Unlike GJC, the KBdGL approach uses the disseminated entangled state not to improve SNR, but, instead, to reduce the number of states required to be teleported. And it is the local CNOT gates that perform most of the data compression. As we have pointed out, one *could* teleport the mostly compressed data (using the disseminated entanglement only in a pairwise fashion between the telescopes and the central processor) and then use a centrally generated GHZ state to do the final data compression locally after teleportation. In fact, as we have also pointed out, one could even take the mostly compressed data and transform it back to optical for direct-detection processing.

11.2 (B) BASELINE LENGTH ASSESSMENT

The GJC approach has no baseline length advantage if the entangled qubits are sent as in-band photons. (If the entangled photons could be sent in a lower-loss transmission band, and then efficiently wavelength-converted to the measurement band, one might find a performance advantage to GJC.) If the photonic qubit delivery is replaced with a repeatered quantum network, there is a potential to make the transmission be lossless, but, as we showed in the last section, the technological demands for that would be truly huge.

The KBdGL approach, as described in their papers, requires quantum memories and a capable quantum network, and could lead to a lossless implementation. Although their design does reduce the number of required disseminated entangled qubits over GJC (and we have proposed a version that further simplifies that step) it still requires a technologically complex system of memories, as well as a huge rate of quantum logic steps. The hybrid nature of the local/non-local view, though, suggests that the more difficult part of the entire process is local and (near) lossless. (Remember, there will be a mode mismatch in the photon capture.)

A very great benefit of banks of quantum memories holding sky photons, though, is that they could allow the OVBLI designer to do away with all the expensive, variable-delay optical transmission systems.

12. OTHER OVLBI REQUIRED SUBSYSTEMS – CLASSICAL AND QUANTUM

We have so far only discussed the core functions required by OVLBI. Real systems would need to include a number of support subsystems, such as: preserving/delivering/stabilizing optical phase across the array; active acquisition and tracking of the interference fringes; spatial adaptive optics; measuring real-time metrics of performance; measuring metrics of machine status and health; etc.

Each of these almost certainly requires dedicated or tapped signals that might not be available in the pure OVLBI architectures discussed herein. If it turns out that any or most of them require a parallel optical path at each telescope, such extra complexity would need to be included in the assessment of the already-huge technological complexity some of these ideas would require. There may also be signal power thus lost to the imaging operations.

This page intentionally left blank.

13. QUANTUM MEMORIES

As quantum memories play important roles in both GJC and KBdGL, we include here a brief discussion of the state of the art.

We have identified two distinct quantum memory use cases for VLBI applications. (We have actually noted four detailed uses in Section K.) The first use case has (a) a quantum memory bank at each telescope location, all of which are tied together via a quantum network. The network distributes entangled states to the various memory banks, thereby establishing shared stored entanglement. In GJC, these would interact locally with signal photons received by the telescopes. In KBdGL, they would be used to assist in the heralding and teleporting steps.

The second use case, in KBdGL, has (b) quantum memories that coherently capture the relevant optical phase difference information of the signal photons themselves as received by the telescopes. This stored quantum information can then be analyzed as we have discussed. (The other more detailed use cases we listed add further requirements onto these signal-filled memories.)

13.1 QUANTUM MEMORY BANKS

Establishing banks of shared stored entanglement for controlled use is a challenging task that goes far beyond simply distributing large entangled states between telescopes. Indeed, for the memory system to be of use, the network must be able to distribute entanglement between telescopes, provide a herald signal that indicates entanglement was successfully distributed and stored at a specific time and between specific memory cells, and then store the entanglement for use in the VLBI protocol. For GJC, this stored entangled state, likely not a photon, would need to be read out and transformed into a photon with the correct wavelength, phase, and timing.

A straightforward manner of establishing memories that achieve this is to use emission-mode quantum memories connected by an entanglement swap gate. The emission-mode quantum memories generate entanglement between the memory qubit and an emitted photonic qubit. Unfortunately, in present designs, this is not a deterministic process. The entanglement swap gate then takes the emitted photons from two or more memories, performs photonic Bell-state measurements on them, and thereby swaps the entanglement from between memories and photons, to between the memories themselves. This, too, is a probabilistic step in present architectures.

Emission mode quantum memories have been demonstrated using atomic ensembles ([45],[46]) where a single collective atomic excitation is entangled with the presence of an emitted photon. This scheme, however, must be operated at very low internal efficiencies in order to avoid multiple excitation events, which do not produce a useful quantum memory state. Typically, these memories must generate photons with less than 5% efficiency. Emission mode quantum memory operation with single emitters such as a single trapped ion ([47]) or a single diamond color center ([48],[49]) offer the benefit that they can, in

principle, be operated at higher efficiencies in a scheme where the energy level of an emitter's valence electron is entangled with the polarization state or the time-bin state of an emitted photon. They have the limitation, however, that they rely upon atomic resonance lines and are therefore limited to tens to hundreds of megahertz of spectral bandwidth. As we showed in our sizing exercise in Section K, such relatively narrow bandwidths mean that a complete VLBI system gathering adequate numbers of photons would need many of these in parallel.

The entanglement swap between multiple emitted photons can be performed with linear optics systems ([56]) or with qubit modalities ([60]), using single photon detectors at the back end. The information of which detector registers a photodetection event, and when it happens can then be used to herald the generation of shared stored entanglement between the remote memory systems. This herald information is sent classically to the memory banks. Memories and Bell state measurement devices have been incorporated into heralded entangled memory systems for atomic ensembles ([51]), ions ([47]), and diamond color centers ([52]), across optical fiber channels at distances of up to a few kilometers and at rates of up to a few hertz.

To develop these quantum memory bank systems for use in VLBI applications, many single-emitter-based emission mode quantum memory would need to be spectrally multiplexed to cover much more than the 10–100 MHz bandwidth of an individual memory. Additionally, huge improvements of system efficiencies and overall operating rates would be needed to bring the currently state-of-the-art hertz-class entanglement distribution rates up to the required THz rates.

We finally note, as we did in Section 7, that the entangled states that are best transmitted and heralded would likely not be single, beam-split photons, but, instead, dual-rail qubits (as shown in (12).) Furthermore, the stored entangled qubits would need to be transformed from their likely dual-rail form back to single photon formats, as prescribed by GJC. Such a step would need development.

13.2 COHERENT QUANTUM MEMORIES

Quantum memories that coherently capture the phase information from received photons, the function required by the KBdGL approach, have been investigated. To build a full array, though, we must distribute an optical phase reference to be used to control all the local operations, including storing and further processing. In addition, for our VLBI array to operate correctly, there cannot be a herald at each telescope's memory. As discussed, KBdGL propose a disseminated GHZ state to be used to herald a photon somewhere in the array, but this quantum logic step must be careful not to disturb the optical phase information held in the stored qubit. As we pointed out, the KBdGL data compression algorithm can be done locally at each telescope.

Phase-coherent storage of single photon optical pulses has been investigated in several atomic ensemble-based modalities, including doped solids ([53]) and warm atomic vapors ([54]), as well as individual emitter-based systems ([55].) These systems generally rely upon three-level atomic arrangements, such as lambda-type structures that are pumped with a strong local oscillator. The local

oscillator drives a coherent pump-probe interaction and acts as phase reference. The phase of the weak stored signal can be referenced to this strong local oscillator, which can act as a common reference by being distributed to all observation stations.

Atomic ensemble-based systems are attractive due to their inherent scalability capabilities, with demonstrated scaling up to more than 100 individually addressable memory cells ([56].) However, the memory's function for these demonstrated ensemble systems has mostly been as an optical delay line with no clear path forward to incorporate multi-qubit logic capabilities.

Individual-emitter-based phase-coherent quantum memories offer the capability to couple memory qubits to secondary qubits that enable quantum logic operations on stored qubits.

In the context of VLBI applications, this takes the form as described in [1],[2]. As shown in Figure 28(a), a single input photon in a superposition of spatial modes is captured across multiple memory qubits (the spatial modes correspond to the capture mode of each of the multiple memories). This capture process is performed via a stimulated Raman adiabatic passage (STIRAP) process as shown in Figure 28(b).

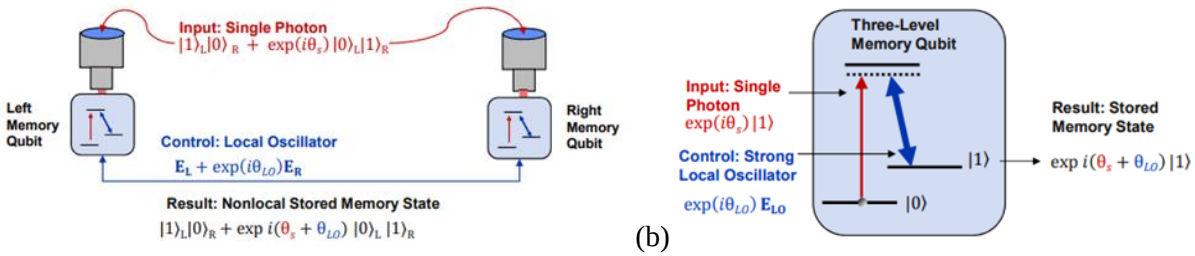

Figure 28. Phase-coherent photon capture for VLBI is shown. (a) shows the multi-memory architecture capturing a multi-spatial-mode single photon. (b) shows the basic stimulated Raman adiabatic passage (STIRAP) process at each memory that enables phase-coherent photonic capture.

The relative phase information of the photon capture mode between the memories is stored by linking each memory with a phase-coherent distributed local oscillator that acts as the STIRAP control beam.

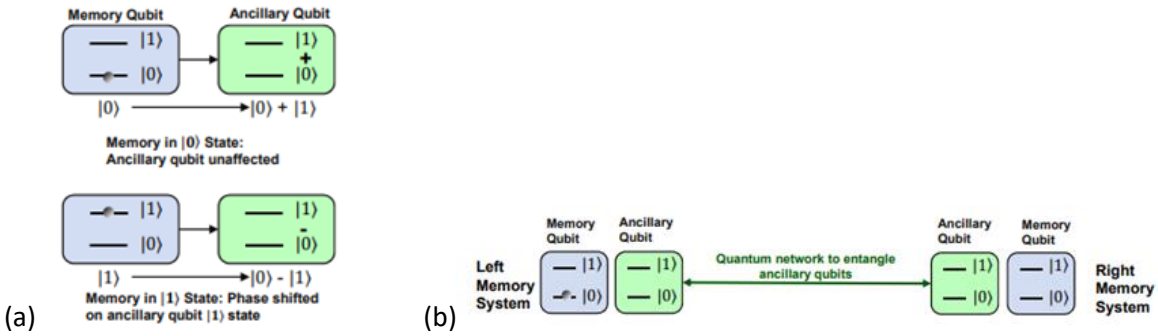

Figure 29. Heralding step for the array of quantum memories.

The phase-coherent distributed qubits corresponding to the captured single-photon state are then each coupled to local ancillary qubit, as shown in Figure 29(a). These ancillary qubits have been pre-entangled across a quantum network (such as the GHz state used by KBdGL), as shown in Figure 29(b), and multi-qubit parity measurement on these ancillary then reveals whether or not a photon was captured in the memories, but crucially does not measure which memory the photon has been stored in, thereby preserving the phase-coherent superposition that is the signal of interest. When done correctly, this multi-qubit process enables phase-coherent photonic capture and storage in the memory qubit, without destroying the photon's relative phase information. They have the inherent limitation of only operating across tens to hundreds of MHz of spectral bandwidth associated with atomic resonance lines. Additionally, this type of individual emitter-based phase-coherent measurement has, to now, only been demonstrated with a single memory cell and at low efficiencies, near 4%. The multi-qubit heralding architecture has not been demonstrated.

13.3 QUANTUM MEMORY CNOTS AND SCALING FOR VLBI

Considerable engineering and development effort is need to realize photonic memory systems that have the required capabilities of (1) having photonically addressable communication qubits that interact with a local register of one or more ancillary qubits, (2) being able to perform CNOT operations between the communication and ancillary qubits, and (3) integration of these capabilities into a highly scaled memory system. Nevertheless, significant progress has recently been made in these areas. Indeed, single qubit registers interacting with photonically addressable communication qubits have been realized in nitrogen-vacancy, silicon-vacancy, and tin-vacancy in diamond systems [57-59]. Moreover, several of these systems have been used to demonstrate CNOT gates between the communication qubit and ancillary qubit [57,58], and multi-qubit register systems are being developed and demonstrated [60]. Parallel efforts have developed the scalability of communication qubits, realizing up 16 communication qubits in a single system [60,61].

14. SUMMARY AND SUGGESTIONS

In this report, we have tried to create a framework for analyzing, understanding, assessing, and comparing a number of classical and quantum-inspired Optical Very Long Baseline Interferometer architectures. We have compared pairs of classical and quantum approaches that each have nearly the same intrinsic performance. The two quantum approaches, however, hold the potential for transmitting known quantum signals across a future quantum network in a manner that can trade high complexity and extra speed for low loss and potentially high performance even with long baselines.

We showed that several classes of quantum memories, all still in early development phases, would be central to the quantum-inspired approaches. We also showed that there are a number of support subsystems and techniques that do not yet exist. Therefore, we feel that it would be fruitful to pursue the development of the following:

- Phase-controlled coherent writing to and reading from an array of quantum memories
- Coherent quantum memories with photon capture that is well spectrally matched
- Well spectrally matched photons for GJC-type measurements
- Efficient qubit conversion from quantum memories to spectrally matched photons
- Efficient, extremely low-noise wavelength conversion to allow low-loss fiber transmission and/or to enable very wide-band operation using narrower-band quantum memories
- Calibration and turbulence mitigation approaches for field-transform OVLBI
- Quantum memories that enable high-speed quantum logic
- Fringe-tracking approaches for the quantum-inspired systems
- Quantum memory banks with variable readout times to enable variable-delay OVLBI functions
- Creation and photonic array dissemination of W-states and GHZ states

We have argued, too, that one might actually find the best solution by operating in the telecom bands. These were shown to have very good delivered photon flux. Low-loss fiber and the high performance components available there, including modern photon detectors, may allow efficient, long-baseline OVLBI, with or without the quantum techniques.

In the References, we list a number of other relevant resources ([63]-[72].)

15. REFERENCES

[1] D. Gottesman, T. Jennewein and S. Croke, "Longer-Baseline Telescopes Using Quantum Repeaters," Phys Rev Letters, vol. 109, p. 070503, 2012.

[2] D. Gottesman, T. Jennewein and S. Croke, "Supplemental Material: Longer-Baseline Telescopes Using Quantum Repeaters," Phys Rev Letters, vol. 109, 2012.

[3] E. T. Khabiboulline, J. Borregaard, K. De Greve, and M. D. Lukin, "Optical Interferometry with Quantum Networks," Phys. Rev. Lett. 123, 070504 (2019)

[4] E. T. Khabiboulline, J. Borregaard, K. De Greve, and M. D. Lukin, "Quantum-assisted telescope arrays," PRA, 100, 022316 (2019).

[5] Fizeau, H., C.R. Acad. Sci. (Paris), 66, 934 (1868)

[6] Michelson, Albert Abraham; Pease, Francis G. (1921). "Measurement of the diameter of alpha Orionis with the interferometer". Astrophysical Journal. 53: 249–59.

[7] P.H. van Cittert, "Die Wahrscheinliche Schwingungsverteilung in Einer von Einer Lichtquelle Direkt Oder Mittels Einer Linse Beleuchteten Ebene". Physica. 1 (1–6): 201–210, (1934)

[8] F. Zernike, "The concept of degree of coherence and its application to optical problems, Physica, Volume 5, Issue 8, August 1938, Pages 785-795

[9] Jansky, Karl G. (1933). "Radio waves from outside the solar system". Nature. 132 (3323): 66

[10] Grote Reber built the world's first astronomical parabolic radio antenna in 1937.

[11] M. Ryle & D. Vonberg, (1946) "Solar radiation on 175Mc/s," Nature 158, pp 339

[12] R.C. Jennison, "A phase sensitive interferometer technique for the measurement of the Fourier transforms of spatial brightness distributions of small angular extent," Monthly Notices of the Royal Astronomical Society, 1958.

[13] N. W. Broten, T. H. Legg, J. L. Locke, C. W. McLeish, R. S. Richards, R. M. Chisholm, H. P. Gush, J. L. Yen and J. A. Galt, "Long baseline interferometry: A new technique," Science, vol. 156, pp. 1592-1593, 1967,

[14] The Event Horizon Telescope Collaboration, "First M87 Event Horizon Telescope Results. I. The Shadow of the Supermassive Black Hole," The Astrophysical Journal Letters, 875:L1 (17pp), 2019 April 10.

[15] Labeyrie, A. Interference fringes obtained on VEGA with two optical telescopes , 1975, 196, L71-L75

[16] M Shao, D H Staelin, "First fringe measurements with a phase-tracking stellar interferometer," Appl Opt. 1980 May 1;19(9):1519-22

[17] Shao, M., Colavita, M. M., Hines, B. E., Staelin, D. H., Hutter, D. J., "The Mark III stellar interferometer," 1988, Astron. Astrophys., 193, 357.

[18] Townes, C.H., "Spatial Interferometry in the Mid-Infrared Region," J. Astrophys. Astr. (1984) 5, 111-130.

[19] ten Brummelaar, T. A. ; McAlister, H. A. ; Ridgway, S. T. ; Bagnuolo, W. G., Jr. ; Turner, N. H. ; Sturmann, L. ; Sturmann, J. ; Berger, D. H. ; Ogden, C. E. ; Cadman, R. ; Hartkopf, W. I. ; Hopper, C. H. ; Shure, M. A., "First Results From the CHARA Array. II. A Description of the Instrument," The Astrophysical Journal, 628: 453-465 (2005)

[20] Armstrong, J. T., Mozurkewich, D., Rickard, L. J., Hutter, D. J., Benson, J. A. et al., "The Navy Prototype Optical Interferometer," 1998, Astrophys. J., 496, 550.

[21] Ashcom, J.B., Allured, R.A., "Performance Analysis of the Magdalena Ridge Observatory Interferometer for Space Situation Awareness," MITLL Project Report TR-1252, 14 May 2020

[22] Tsang, M., "Quantum Nonlocality in Weak-Thermal-Light Interferometry," PRL 107, 270402, (2011)

[23] Hanbury Brown, R. and Twiss, R.Q., "A New Type of Interferometer for Use in Radio Astronomy," Phil. Mag., 45, 663 (1954).

[24] Hanbury Brown R and Twiss R, "Correlation between photons in the two coherent beams of light," Nature, 177, 27–9

[25] Hanbury Brown R and Twiss R, "A test of a new type of stellar interferometer on Sirius," Nature, 178, 1046–8.

[26] A. Labeyrie, S. G. Lipson, and P. Nisenson, *An Introduction to Optical Stellar Interferometry*, (Cambridge Univ., Cambridge 2006).

[27] M.A. Nielsen, I.L. Chuang, Quantum Computation and Quantum Information, 2000, Cambridge University Press.

[28] Jankov, S., "Astronomical Optical Interferometry. I. Methods and Instrumentation," Serb. Astron J. No 181 (1020), 1-17 (2010)

[29] Frank Eisenhauer , John D. Monnier and Oliver Pfuhl, "Advances in Optical / Infrared Interferometry," arXiv:2303.00453v1

[30] D. F. Buscher, M. Creech-Eakman, A. Farris, C. A. Haniff and J. S. Young, "The Conceptual Design of the Magdalena Ridge Observatory Interferometer," J. Astron. Instr., Vol 2, No 2, (2013) 1340001-1-1340001-19

[31] Monnier, J.D., "Optical interferometry in astronomy," Rep. Prog. Phys, 66 (2003) 789-857

[32] R.M. Mersereau, "The Processing of Hexagonally Sampled Two-Dimensional Signals," Proc IEEE, Vol 67, No 6, Jun 1979, pp 930-953.

[33] J.C. Erhardt, “Hexagonal Fast Fourier Transform with Rectangular Output,” IEEE Trans Sig Proc, Vol 41, N 3, March 1993, pp 1469-1472.

[34] A. Dutt, V. Rokhlin, “Fast Fourier Transforms for Nonequispaced Data, II,” Appl and Comp Harmonic Anal, V 2, pp85-100 (1995.)

[35] D. Potts, G. Steidl, M. Tasche, “Fast Fourier transforms for nonequispaced data: A tutorial,” Modern Sampling Theory, Chapter I.

[36] D. Coppersmith, “An Approximate Fourier Transform Useful in Quantum Factoring,” 12 Jul 1994, IBM Research Report.

[37] L Gyongyosi, S. Imre, “An Improvement in Quantum Fourier Transform,” 18 July 2012, 1207.4464

[38] M. Reck, A. Zeilinger, H.J. Bernstein, P. Bertani, “Experimental Realization of Any Discrete Unitary Operator,” PRL Vol 73, No 1, 4 July 1994, 58-61.

[39] B.A. Bell, I.A. Walmsley, “Further compactifying linear optical unitaries,” APL Photon. 6, 070804 (2021)

[40] Nicholas C. Harris , Gregory R. Steinbrecher , Jacob Mower , Yoav Lahini , Dirk Englund, “Quantum Random Walks in a Programmable Nanophotonic Processor,” Optica 2014.

[41] B.G. Kurien, V. Tarokh,Y. Rachlin, V.N. Shah, J.B. Ashcom, “Resolving phase ambiguities in the calibration of redundant interferometric arrays: implications for array design,” MNRAS 461, 3585–3597 (2016)

[42] B.G. Kurien, J.B. Ashcom, V.N. Shah, Y. Rachlin, V. Tarokh, “Robust interferometric imaging via prior-less phase recovery: redundant spacing calibration with generalized-closure phases,” MNRAS 464, 2356–2376 (2017).

[43] Wieringa, M., “An investigation of the telescope based calibration methods ‘redundancy’ and ‘self-cal’,” 1992, Exp. Astron., 2, 203.

[44] A. Liu, M. Tegmark, S. Morrison, A. Lutomirski, M. Zaldarriaga, “Precision calibration of radio interferometers using redundant baselines,” Mon. Not. R. Astron. Soc. 408, 1029–1050 (2010).

[45] Duan, LM., Lukin, M., Cirac, J. et al. Long-distance quantum communication with atomic ensembles and linear optics. Nature 414, 413–418 (2001). https://doi.org/10.1038/35106500

[46] Nicolas Sangouard, Christoph Simon, Hugues de Riedmatten, and Nicolas Gisin, Quantum repeaters based on atomic ensembles and linear optics, Rev. Mod. Phys. 83 (2011).

[47] P. Maunz, S. Olmschenk, D. Hayes, D. N. Matsukevich, L.-M. Duan, and C. Monroe, Heralded Quantum Gate between Remote Quantum Memories, Phys. Rev. Lett. 102, 250502 (2009).

[48] C. T. Nguyen, D. D. Sukachev, M. K. Bhaskar, B. Machielse, D. S. Levonian, E. N. Knall, P. Stroganov, R. Riedinger, H. Park, M. Lončar, and M. D. Lukin, Quantum Network Nodes Based on Diamond Qubits with an Efficient Nanophotonic Interface, Phys. Rev. Lett. 123, 183602 (2019).

[49] Bernien, H., Hensen, B., Pfaff, W. et al. Heralded entanglement between solid-state qubits separated by three metres. Nature 497, 86–90 (2013).

[50] Bhaskar, M.K., Riedinger, R., Machielse, B. et al. Experimental demonstration of memory-enhanced quantum communication. Nature 580, 60–64 (2020).

[51] Xi-Yu Luo, Yong Yu, Jian-Long Liu, Ming-Yang Zheng, Chao-Yang Wang, Bin Wang, Jun Li, Xiao Jiang, Xiu-Ping Xie, Qiang Zhang, Xiao-Hui Bao, and Jian-Wei Pan, Postselected Entanglement between Two Atomic Ensembles Separated by 12.5 km, Phys. Rev. Lett. 129, 050503 (2022).

[52] Hensen, B., Bernien, H., Dréau, A. et al. Loophole-free Bell inequality violation using electron spins separated by 1.3 kilometres. Nature 526, 682–686 (2015).

[53] Mikael Afzelius, Christoph Simon, Hugues de Riedmatten, and Nicolas Gisin, Multimode quantum memory based on atomic frequency combs, Phys. Rev. A 79, 052329 – Published 21 May 2009

[54] Ma, L., Lei, X., Yan, J. et al. High-performance cavity-enhanced quantum memory with warm atomic cell. Nat Commun 13, 2368 (2022).

[55] A. D. Boozer, A. Boca, R. Miller, T. E. Northup, and H. J. Kimble, Reversible State Transfer between Light and a Single Trapped Atom, Phys. Rev. Lett. 98, 193601 – Published 8 May 2007

[56] Jiang, N., Pu, YF., Chang, W. et al. Experimental realization of 105-qubit random access quantum memory. npj Quantum Inf 5, 28 (2019).

[57] Unconditional quantum teleportation between distant solid-state quantum bits, W. Pfaff, B. J. Hensen, H. Bernien, S. B. van Dam, M. S. Blok, T. H. Taminiau, M. J. Tiggelman, R. N. Schouten, M. Markham, D. J. Twitchen, and R. Hanson, Science 345, 532-535 (2014)

[58] An integrated nanophotonic quantum register based on silicon-vacancy spins in diamond, C. T. Nguyen, D. D. Sukachev, M. K. Bhaskar, B. Machielse, D. S. Levonian, E. N. Knall, P. Stroganov, C. Chia, M. J. Burek, R. Riedinger, H. Park, M. Lončar, and M. D. Lukin, Phys. Rev. B 100, 165428 (2019)

[59] A diamond nanophotonic interface with an optically accessible deterministic electronuclear spin register, R. A. Parker, J. A. Martínez, K. C. Chen, A. M. Stramma, I.B. Harris, C. P. Michaels, M. E. Trusheim, M. H. Appel, C. M. Purser, W. G. Roth, D. Englund, and M.Atatüre, arXiv:2305.18923 [quant-ph] (2023)

[60] A Ten-Qubit Solid-State Spin Register with Quantum Memory up to One Minute, C. E. Bradley, J. Randall, M. H. Abobeih, R. C. Berrevoets, M. J. Degen, M. A. Bakker, M. Markham, D. J. Twitchen, and T. H. Taminiau, Phys. Rev. X 9, 031045 (2019)

[61] Large-scale integration of artificial atoms in hybrid photonic circuits, N. H. Wan, T. Lu, K. C. Chen, M.l P. Walsh, M. E. Trusheim, L. De Santis, E. A. Bersin, I. B. Harris, S. L. Mouradian, I. R. Christen, E. S. Bielejec, and D. Englund, Nature, 583, 226–231 (2020)

[62] Fully Packaged Multichannel Cryogenic Quantum Memory Module, D. J. Starling, K. Shtyrkova, I. Christen, R. Murphy, L. Li, K. C. Chen, D. Kharas, X. Zhang, J. Cummings, W. J. Nowak, E. Bersin, R. J. Niffenegger, M. Sutula, D. Englund, S. Hamilton, and P. B. Dixon, Phys. Rev. Applied 19, 064028 (2023)

[63] P. Stankus, A. Nomerotski, and A. Slosar, "Two-photon amplitude interferometry for precision astrometry," arXiv:2010.09100 [astro-ph.IM].

[64] Matthew Brown, Valerian Thiel, Markus Allgaier, Michael Raymer, Brian Smith, Paul Kwiat, and John Monnier, " Long-baseline interferometry using single photon states as a non-local oscillator," SPIE OPTO, 2022, San Francisco, CA.

[65] J. Bland-Hawthorn, M. J. Sellars, J. G. Bartholomew, "Quantum memories and the double-slit experiment: implications for astronomical interferometry," J. Opt. Soc. Am. B 38, A86–A98 (2021)

[66] A. Lannes and E Anterrieu, "Redundant spacing calibration: phase restoration methods," J. Opt. Soc. Am. A/ Vol. 16, No. 12/December 1999, pp 2866-2879.

[67] Robert Czupryniak, John Steinmetz, Paul G. Kwiat, and Andrew N. Jordan, "Optimal photonic gates for quantum-enhanced telescopes ," arXiv:2108.01170v1 [quant-ph] 2 Aug 2021.

[68] Siddhartha Santra, Brian T. Kirby, Vladimir S. Malinovsky, and Michael Brodsky, "Quantum-scheme for improving interferometric visibility with imperfect distributed entangled-states," 2017 IEEE Photonics Society Summer Topical Meeting Series (SUM)

[69] Zixin Huang ,1,* Gavin K. Brennen ,1,† and Yingkai Ouyang, "Imaging Stars with Quantum Error Correction," PRL 129, 210502 (2022)

[70] Marta Maria Marchese and Pieter Kok, "Large baseline optical imaging assisted by single photons and linear quantum optics," arXiv:2212.08516v1, 16 Dec 2022.

[71] Crawford, Jesse ; Dolzhenko, Denis ; Keach, Michael ; Mueninghoff, Aaron ; Abrahao, Raphael A. ; Martinez-Rincon, Julian ; Stankus, Paul ; Vintskevich, Stephen ; Nomerotski, Andrei, "Towards Quantum Telescopes: Demonstration of a Two-Photon Interferometer for Quantum-Assisted Astronomy," arXiv:2301.07042, 2023.

[72] David Diaz, Yujie Zhang, Virginia O. Lorenz, and Paul G. Kwiat, "Emulating Quantum-enhanced Long-Baseline Interferometric Telescopy," Frontiers in Optics, 2021.

APPENDIX 1 – MATHEMATICAL MODEL

Assumptions:

- The astronomical object, $\boldsymbol{\mathcal{A}_S}$, is centered at $\boldsymbol{\rho}_S$ in the $z = 0$ plane. It is convenient to define that as the origin of the plane, so we let $\boldsymbol{\rho}_S \equiv (0,0)$**.**
- We let $\boldsymbol{\rho} = (x, y)$ be the coordinate vector for an arbitrary point in the plane of the object. (See Figure A-1)
- The astronomical object radiates a scalar field that is spatially incoherent, statistically stationary in time, and cross-spectrally pure
    - with complex envelope, $E_S(\boldsymbol{\rho} + \boldsymbol{\rho}_S, t)$, $\boldsymbol{\rho}_S \equiv (0,0)$,
    - confined to a region $\boldsymbol{\rho} \in \mathcal{A}_S$ in the $z = 0$ plane
    - where $\mathcal{A}_S$ has diameter $D_S \equiv max_{(\boldsymbol{\rho_1}, \boldsymbol{\rho_2}) \in \mathcal{A}_S} |\boldsymbol{\rho_1} - \boldsymbol{\rho_2}|$. We take $E_S(\boldsymbol{\rho}, t)$ to have units $\sqrt{\frac{photons}{m^2 s}}$ so that $|E_S(\boldsymbol{\rho}, t)|^2$ is the short-time-average photon-flux density crossing the $z = 0$ plane at location $\boldsymbol{\rho}$ and time t.
- Optical filtering with center wavelength λ and bandwidth $\Omega \ll \lambda$ is to be performed at the telescopes. Without loss of generality, this filtering can be assumed to occur at the astronomical objects so that the astronomical light can be modeled as quasimonochromatic on the carrier ω_0 where $c = \lambda\, \omega_0 / 2\pi$.
- The point on the earth, a distance Z away, that sees the object straight overhead is also at $\boldsymbol{\rho}_S$ (again, we let $\boldsymbol{\rho}_S = (0,0)$) in the $z = Z$ plane. These planes are defined to be orthogonal to the ray between the center of the object and this point on the earth.
- The terrestrial telescopes will not necessarily fall on the defined plane, due to the curvature of the earth or other placement. The kth telescope sits at a position such that, when it is tilted to aim at the center of the object in the sky, a ray from its center up to the object passes through $\boldsymbol{\rho}_k$ in the $z = Z$ plane. (See Figures A-1 and A-2. If the telescope is in front of the plane, we can similarly project its ray back to the plane.)
- Telescope k in the array has a circular entrance pupil with diameter D_k and area $A_k = \pi \mathrm{D}_k{}^2/4$ (defined in the z=Z plane.) We can also define the maximum diameter of the entire array (as measured in the $z = Z$ plane) to be D_A.
- We assume deep far-field propagation:

$$\frac{\mathrm{D}_k{}^2}{Z} \ll \lambda \qquad \text{(A1-1)}$$

This means that any wavefront emanating from a point in the object has a curvature across a telescope much less than a wavelength. That is,

$$Z - \sqrt{Z^2 - \left(\frac{\mathrm{D}_k}{2}\right)^2} \approx \frac{{\mathrm{D}_k}^2}{8Z} < \frac{{\mathrm{D}_k}^2}{Z} \ll \lambda \tag{A1-2}$$

- We also assume

$$\frac{\mathrm{D}_S}{Z} \ll \frac{\lambda}{\mathrm{D}_k} \tag{A1-3}$$

which means that the angular extent of the object as seen from a telescope is much less than the beamwidth of that telescope, and so no individual telescope can discern any spatial details of the object. Of course, we will have designed the array so that

$$\frac{\lambda}{\mathrm{D}_A} < \frac{\mathrm{D}_S}{Z} \tag{A1-4}$$

which means that the resolution (beamwidth) created by the entire array is smaller than the object in order that we can resolve details in it. Suppose we design the array to result in N pixels across the object, or

$$\frac{\mathrm{D}_S}{Z} = N\frac{\lambda}{\mathrm{D}_A} \tag{A1-5}$$

This is equivalent to

$$\left(\frac{{\mathrm{D}_A}^2}{Z}\right)\left(\frac{{\mathrm{D}_S}^2}{Z}\right) = N^2\lambda^2 \tag{A1-6}$$

It is straightforward to show that the pointing angle of an outermost telescope in an array centered at (0,0) differs from the pointing angle of a telescope at the array center by $\left(\frac{\mathrm{D}_A}{2Z}\right)$. For arrays offset from the sub-object point by a distance X, the difference of pointing angles between outermost telescopes can be seen to be

$$tan^{-1}\left(\frac{\mathrm{D}_A}{Z + X\left[\frac{\mathrm{D}_A + X}{Z}\right]}\right) \approx \frac{\mathrm{D}_A}{Z} \ll \frac{\lambda}{\mathrm{D}_k}\frac{\mathrm{D}_A}{\mathrm{D}_S} \tag{A1-7}$$

If $\mathrm{D}_A < \mathrm{D}_S$, then that means that the difference between the pointing angles of all the telescopes is much less than the beamwidth of any single telescope, and so we can model the system as if all the telescopes point in exactly the same direction. (For extremely large arrays, one would

need to calculate $\frac{D_A}{Z}$ exactly, but the telescopes will almost certainly still be found to point in almost the same direction.)

- All these assumptions mean we can work with angles and phases and signals as seen on the z=0 and z=Z planes, as long as delays between the object center and the telescope centers are equalized via the addition of extra physical path delays. See Figure A-2.
- Finally, we will assume

$$\frac{{D_S}^2}{Z} \ll \lambda \tag{A1-1a}$$

We will use this to simplify the phase term in the incoming field. (We note that this may not quite be true for very large objects. However, replacing D_S with the maximum distance between object points that can be considered coherent will certainly be true and will lead to the same phase simplification in (A1-19).)

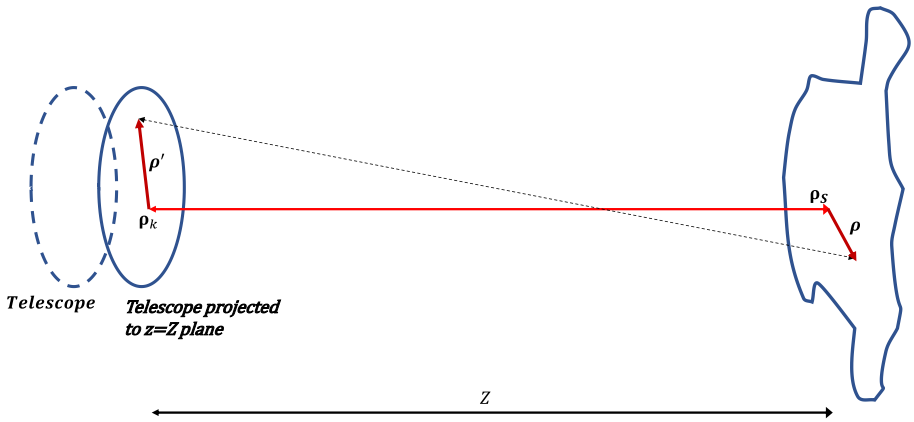

Figure A-1. Geometry and math of the sky object and the telescope array.

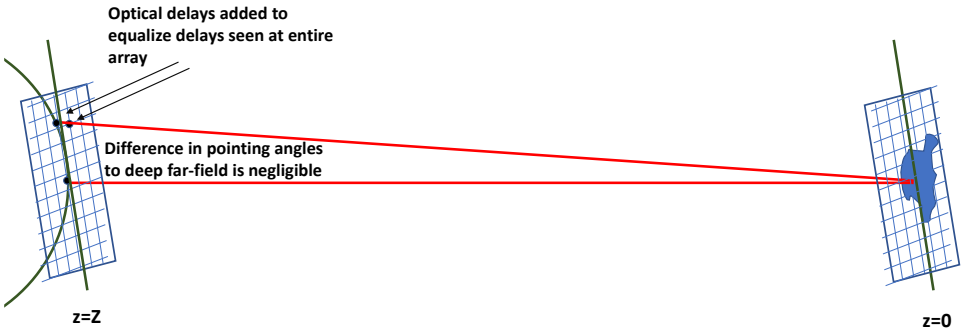

Figure A-2. Geometry of the planes of the sky object and the telescope array.

- We assume $E_s(\boldsymbol{\rho}, t)$ is a zero-mean, complex-valued Gaussian random process that is completely characterized by its temporal correlation function,

$$\langle E^*{}_s(\boldsymbol{\rho}, t+\tau) E_s(\boldsymbol{\rho}', t)\rangle = \lambda^2 N_S I_s(\boldsymbol{\rho}) R_s(\tau)\delta(\boldsymbol{\rho} - \boldsymbol{\rho}') \tag{A1-8}$$

  where $\langle . \rangle$ denotes ensemble average. Here:
  - $I_s(\boldsymbol{\rho}) \geq 0$ is the object's 2-D spatial distribution with units 1/m^2; and it is normalized such that

$$\int_{\mathcal{A}_S} d^2\boldsymbol{\rho} I_s(\boldsymbol{\rho}) = 1 \tag{A1-9}$$

  - N_S is the source brightness (in photons/s-Hz)
  - $\delta(\boldsymbol{\rho}) = \delta(x)\,\delta(y)$ is the 2-D delta function with dimension 1/m^2
  - $R_s(\tau)$ is the normalized temporal correlation function such that $N_S R_s(0)$ is the source's average photon flux and $N_S I_s(\boldsymbol{\rho}) R_s(0)$ is its average photon flux density at location $\boldsymbol{\rho}$ and time t
  - The source's associated dimensionless spectral density is then defined

$$S_s(\omega) = \int d\tau R_s(\tau) e^{-j\omega\tau} \tag{A1-10}$$

    which has bandwidth Ω due to filtering as described earlier

  - We sometimes have occasion to assume a Gaussian filtered spectral shape as

$$S_s(\omega) = e^{-\omega^2 {t_s}^2} \tag{A1-11}$$

$$R_s(\tau) = \frac{e^{-\frac{\tau^2}{4{t_s}^2}}}{\sqrt{4\pi {t_s}^2}} \tag{A1-12}$$

- The ray between an arbitrary point, $\boldsymbol{\rho}$, in the object and an arbitrary point, $\boldsymbol{\rho'}_k$, in telescope k has length

$$D(\boldsymbol{\rho_k} + \boldsymbol{\rho'}_k, \boldsymbol{\rho}_S + \boldsymbol{\rho}) = \sqrt{Z^2 + \left|\boldsymbol{\rho_k} + \boldsymbol{\rho'}_k - (\boldsymbol{\rho}_S + \boldsymbol{\rho})\right|^2} \tag{A1-13}$$

$$= Z\sqrt{1 + \frac{\left|\boldsymbol{\rho_k} + \boldsymbol{\rho'}_k - (\boldsymbol{\rho}_S + \boldsymbol{\rho})\right|^2}{Z}} \approx Z + \frac{\left|\boldsymbol{\rho_k} + \boldsymbol{\rho'}_k - (\boldsymbol{\rho}_S + \boldsymbol{\rho})\right|^2}{2Z}$$

We start from the quasimonochromatic form of Fresnel diffraction from a point $(\boldsymbol{\rho}_S + \boldsymbol{\rho})$ in the $z = 0$ plane at the astronomical object to point $\boldsymbol{\rho'}$ in the Kth telescope's entrance pupil in the $z = Z$ plane

$$E_k(\boldsymbol{\rho'}, t) = \int_{\mathcal{A}_S} d^2\boldsymbol{\rho}\, E_s\left(\boldsymbol{\rho}_S + \boldsymbol{\rho}, t - \frac{D(\boldsymbol{\rho_k} + \boldsymbol{\rho'}_k, \boldsymbol{\rho}_S + \boldsymbol{\rho})}{c}\right)\frac{e^{j\frac{2\pi}{\lambda}D(\boldsymbol{\rho_k} + \boldsymbol{\rho'}_k, \boldsymbol{\rho}_S + \boldsymbol{\rho})}}{j\lambda Z} \tag{A1-14}$$

The correctly-pointed telescope takes this plane wave and integrates over its area to find

$$E_k(t) \equiv \frac{1}{\sqrt{A_k}}\int_{\mathcal{A}_k} d^2\boldsymbol{\rho'}_k\, E_k\left(\boldsymbol{\rho'}_k, t\right)e^{-j\frac{2\pi}{\lambda Z}\boldsymbol{\rho_k}\cdot\boldsymbol{\rho'}_k} \tag{A1-15}$$

We include the phase term in order to show that we point exactly at the object, even though this phase term is tiny.

We will sometimes find it more useful to describe the source image and fields in terms of angles instead of distances, so let us define angular coordinates

$$\boldsymbol{\alpha} = \boldsymbol{\rho}/Z\,, \qquad d^2\boldsymbol{\rho} = Z^2 d^2\boldsymbol{\alpha} \tag{A1-16}$$

and the normalized (and centered) source distribution

$$\tilde{E}_s(\boldsymbol{\alpha}, t) \equiv ZE_s(Z\boldsymbol{\alpha}, t), \quad \tilde{I}_s(\boldsymbol{\alpha}) = Z^2 I_s(Z\boldsymbol{\alpha}), \qquad \int d^2\boldsymbol{\alpha}\, \tilde{I}_s(\boldsymbol{\alpha}) = 1 \tag{A1-17}$$

We can continue to write $\mathcal{A}$ when we integrate since either the angular extent or physical extent will be obvious.

It will be useful to assume $\boldsymbol{\rho}_S = \mathbf{0}$ so that the distance formula becomes:

$$D\left(\boldsymbol{\rho_k} + \boldsymbol{\rho'}_k, \boldsymbol{\rho}_S + \boldsymbol{\rho}\right) \approx Z + \frac{\left|\boldsymbol{\rho_k} + \boldsymbol{\rho'}_k - \boldsymbol{\rho}\right|^2}{2Z} \tag{A1-18}$$

$$= Z + \frac{\left|\boldsymbol{\rho'}_k\right|^2}{2Z} + \frac{|\boldsymbol{\rho}|^2}{2Z} - \frac{2\left(\boldsymbol{\rho'}_k\right)\cdot(\boldsymbol{\rho})}{2Z} + \frac{|\boldsymbol{\rho_k}|^2}{2Z} + \frac{2(\boldsymbol{\rho_k})\cdot\left(\boldsymbol{\rho'}_k - \boldsymbol{\rho}\right)}{2Z}$$

Then we know

$$\frac{|\boldsymbol{\rho'}_k|^2}{2Z} < \frac{\mathrm{D}_k{}^2}{2Z} \ll \lambda/2 \text{ , and } \frac{|\boldsymbol{\rho}|^2}{2Z} < \frac{\mathrm{D}_S{}^2}{2Z} \ll \lambda/2, \tag{A1-19}$$

$$\text{and } \frac{2\left(\boldsymbol{\rho'}_k\right)\cdot(\boldsymbol{\rho})}{2Z} < \frac{2\mathrm{D}_k\mathrm{D}_S}{2Z} \ll \lambda$$

and so the first three terms can be ignored in (A1-14) in both the temporal term (divided by c) and the phase term (multiplied by $\frac{2\pi}{\lambda}$.) Thus, we can approximate

$$D\left(\boldsymbol{\rho_k} + \boldsymbol{\rho'}_k, \boldsymbol{\rho}_S + \boldsymbol{\rho}\right) \approx Z + \frac{|\boldsymbol{\rho_k}|^2}{2Z} + \frac{2(\boldsymbol{\rho_k})\cdot\left(\boldsymbol{\rho'}_k - \boldsymbol{\rho}\right)}{2Z} \tag{A1-20}$$

We then have

(A1-21)

$$E_k(t) = \frac{e^{j\frac{2\pi}{\lambda}\left(Z + \frac{|\boldsymbol{\rho_k}|^2}{2Z}\right)}}{j\lambda Z\sqrt{A_k}} \int_{\mathcal{A}_k} d^2\boldsymbol{\rho'}_k \, e^{j\frac{2\pi(\boldsymbol{\rho_k})\cdot(\boldsymbol{\rho'}_k)}{\lambda \quad Z}} e^{-j\frac{2\pi}{\lambda Z}\boldsymbol{\rho_k}\cdot\boldsymbol{\rho'}_k} \int_{\mathcal{A}_S} d^2\boldsymbol{\rho}\, E_s\left(\boldsymbol{\rho}, t - Z/c - \frac{|\boldsymbol{\rho_k}|^2}{2cZ} + \frac{2(\boldsymbol{\rho_k})\cdot\left(\boldsymbol{\rho'}_k - \boldsymbol{\rho}\right)}{2cZ}\right) e^{-j\frac{2\pi\boldsymbol{\rho_k}\cdot\boldsymbol{\rho}}{\lambda \quad Z}}$$

In the temporal term, we see that

$$\left|\frac{2(\boldsymbol{\rho_k})\cdot(\boldsymbol{\rho'}_k-\boldsymbol{\rho})}{2cZ}\right| < \frac{\mathrm{D}_A(\mathrm{D}_k+\mathrm{D}_S)}{cZ}$$

is much smaller than the other temporal terms, and is, in addition, much less than temporal details of the process's narrow-band autocorrelation function, and so we can ignore it, giving

$$E_k(t) = \frac{e^{j\frac{2\pi}{\lambda}\left(Z+\frac{|\boldsymbol{\rho_k}|^2}{2Z}\right)}}{j\lambda Z\sqrt{A_k}}\int_{\mathcal{A}_k} d^2\boldsymbol{\rho'}_k\, e^{j\frac{2\pi(\boldsymbol{\rho_k})\cdot(\boldsymbol{\rho'}_k)}{\lambda\ \ Z}} e^{-j\frac{2\pi}{\lambda Z}\boldsymbol{\rho_k}\cdot\boldsymbol{\rho'}_k}\int_{\mathcal{A}_S} d^2\boldsymbol{\rho}\, E_s\left(\boldsymbol{\rho}, t-Z/c-\frac{|\boldsymbol{\rho_k}|^2}{2cZ}\right)e^{-j\frac{2\pi\boldsymbol{\rho_k}\cdot\boldsymbol{\rho}}{\lambda\ \ Z}} \tag{A1-22}$$

$$= \frac{\sqrt{A_k}e^{j\frac{2\pi}{\lambda}\left(Z+\frac{|\boldsymbol{\rho_k}|^2}{2Z}\right)}}{j\lambda Z}\int_{\mathcal{A}_S} d^2\boldsymbol{\rho}\, E_s\left(\boldsymbol{\rho}, t-Z/c-\frac{|\boldsymbol{\rho_k}|^2}{2cZ}\right)e^{-j\frac{2\pi\boldsymbol{\rho_k}\cdot\boldsymbol{\rho}}{\lambda\ \ Z}}$$

We can note that Z/c is a constant describing the constant time delay from the source (likely hundreds of thousands of years or more) and so can be ignored. Also, the term $\frac{|\boldsymbol{\rho_k}|^2}{2cZ}$, due to c and Z both being very large, is tiny and so can also be ignored.

This page intentionally left blank.

APPENDIX 2 – MATHEMATICAL ANALYSIS OF FAR-FIELD CORRELATIONS – THE VAN CITTERT-ZERNIKE THEORY

Using the model of Appendix 1, we examine the correlation between the complex fields at telescopes K and J to find

$$\left\langle E_K{}^*(t+\tau)E_J(t)\right\rangle = \left\langle \frac{e^{-j\frac{2\pi}{\lambda}\left(Z+\frac{|\boldsymbol{\rho}_K|^2}{2Z}\right)}\sqrt{A_K}}{\lambda Z}\int_{\mathcal{A}_S} d^2\boldsymbol{\rho}_1\, E_s{}^*\left(\boldsymbol{\rho}_1, t+\tau-Z/c-\frac{|\boldsymbol{\rho}_K|^2}{2cZ}\right)e^{j\frac{2\pi\boldsymbol{\rho}_K\cdot\boldsymbol{\rho}_1}{\lambda\ Z}}\right. \tag{A2-1}$$

$$\left. x\,\frac{e^{j\frac{2\pi}{\lambda}\left(Z+\frac{|\boldsymbol{\rho}_J|^2}{2Z}\right)}\sqrt{A_J}}{\lambda Z}\int_{\mathcal{A}_S} d^2\boldsymbol{\rho}_2\, E_s\left(\boldsymbol{\rho}_2, t-Z/c-\frac{|\boldsymbol{\rho}_J|^2}{2cZ}\right)e^{j\frac{-2\pi\boldsymbol{\rho}_J\cdot\boldsymbol{\rho}_2}{\lambda\ Z}}\right\rangle$$

$$= e^{-j\frac{2\pi(|\boldsymbol{\rho}_K|^2-|\boldsymbol{\rho}_J|^2)}{2\lambda Z}}\left\{\frac{\sqrt{A_K A_J}}{Z^2}N_S R_s(\tau)\right\}\int_{\mathcal{A}_S} d^2\boldsymbol{\rho}_1\ I_s(\boldsymbol{\rho}_1)e^{j\frac{2\pi(\boldsymbol{\rho}_K-\boldsymbol{\rho}_J)\cdot\boldsymbol{\rho}_1}{\lambda Z}}$$

where we were able to ignore a tiny temporal term.

The out-front phase term is a very small constant that can either be calculated and thus removed or merely ignored. Thus, the mutual coherence between the light collected at telescopes K and J is

$$\left\langle E_K{}^*(t)E_J(t)\right\rangle = \left\{\frac{\sqrt{A_K A_J}}{Z^2}N_S R_s(0)\right\}\int_{\mathcal{A}_S} d^2\boldsymbol{\rho}_1\ I_s(\boldsymbol{\rho}_1)e^{j\frac{2\pi(\boldsymbol{\rho}_K-\boldsymbol{\rho}_J)\cdot\boldsymbol{\rho}_1}{\lambda Z}} \tag{A2-2}$$

We can define the received signal strength (where we now assume all the telescopes have the same area) as

$$\mathcal{N}_S \equiv \frac{A}{Z^2}N_S$$

This is the apparent source brightness in photons/s-Hz.

We can also define the normalized mutual coherence as

$$\gamma_{KJ} \equiv \frac{\left\langle E_K{}^*(t)E_J(t)\right\rangle}{\sqrt{\langle|E_K(t)|^2\rangle\left\langle\left|E_J(t)\right|^2\right\rangle}} = \int_{\mathcal{A}_S} d^2\boldsymbol{\rho}\ I_s(\boldsymbol{\rho})e^{j\frac{2\pi(\boldsymbol{\rho}_K-\boldsymbol{\rho}_J)\cdot\boldsymbol{\rho}}{\lambda Z}} \tag{A2-3}$$

This normalized mutual coherence can also be written using the angle notation described in Appendix 1 as

$$\gamma_{KJ} = \int_{\mathcal{A}_S} d^2\boldsymbol{\alpha}\ \tilde{I}_s(\boldsymbol{\alpha}) e^{j2\pi(\frac{\boldsymbol{\rho}_K - \boldsymbol{\rho}_J}{\lambda})\cdot\boldsymbol{\alpha}} \tag{A2-4}$$

This is the (deep far-field version of the) quasimonochromatic van Cittert-Zernike (vC-Z) theorem ([3],[4].) That is, except for the bracketed term out front (in A2-2), and which can either be ignored or, if known, be calculated off-line, the complex correlation between the fields at two telescopes is proportional to the (inverse) 2-D spatial Fourier transform of the source's angular distribution as calculated at a spatial frequency related to the vector between the telescopes (ie, the baseline.) From this observation, we are motivated to try to measure this correlation at many spatial (ie, baselines) and then try to perform an inverse (discrete) 2-D Fourier transform (numerically) to obtain an image of that distribution.

Towards this goal, let us define the 2-D telescope position and sky angle vectors in terms of their x and y coordinates.

$$\begin{aligned} \boldsymbol{\rho}_k &= x_k \underline{e}_x + y_k \underline{e}_y \\ \frac{\boldsymbol{\rho}}{Z} &= \boldsymbol{\alpha} = \xi \underline{e}_x + \eta \underline{e}_y \end{aligned} \tag{A2-5}$$

(We remember from the discussion in Appendix 1 that the sky angle vectors are essentially the same for all the telescopes.) Then we can define the baselines in numbers of wavelengths as

$$\frac{\Delta x_{jk}}{\lambda} \equiv \frac{x_j - x_k}{\lambda}, \quad \frac{\Delta y_{jk}}{\lambda} \equiv \frac{y_j - y_k}{\lambda} \tag{A2-6}$$

and define a normalized correlation (from (A2-4)

$$g\left(\frac{\Delta x_{jk}}{\lambda}, \frac{\Delta y_{jk}}{\lambda}\right) = \int_{-\infty}^{\infty}\int \tilde{I}_S(\xi,\eta)\, exp\left[j2\pi\left(\frac{\Delta x_{jk}}{\lambda}\xi + \frac{\Delta y_{jk}}{\lambda}\eta\right)\right] d\xi d\eta \tag{A2-7}$$

Since we have only a sparsely-sampled plane of spatial frequencies (often called the u-v plane because in some references, $(\frac{\Delta x_{jk}}{\lambda}, \frac{\Delta y_{jk}}{\lambda})$ is defined as (u,v)) we see that we would be calculating the discretized Fourier Transform of this as:

$$\begin{aligned} \tilde{\tilde{I}}_s(\hat{\xi},\hat{\eta}) &\approx \frac{1}{N^2}\sum_j \sum_k g\left(\frac{\Delta x_{jk}}{\lambda}, \frac{\Delta y_{jk}}{\lambda}\right) exp\left[-j2\pi\left(\frac{\Delta x_{jk}}{\lambda}\hat{\xi} + \frac{\Delta y_{jk}}{\lambda}\hat{\eta}\right)\right] \\ &= \tfrac{1}{N^2}\int_{-\infty}^{\infty}\int \tilde{I}_S(\xi,\eta)\left\{\sum_j \sum_k exp\left[j2\pi\left(\tfrac{\Delta x_{jk}}{\lambda}[\xi - \hat{\xi}] + \tfrac{\Delta y_{jk}}{\lambda}[\eta - \hat{\eta}]\right)\right]\right\} d\xi d\eta \end{aligned} \tag{A2-8}$$

A name often given to $\tilde{\tilde{I}}_s$ is the "dirty image" which is seen here to be the convolution of the correct image, $\tilde{I}_s$, with the term in brackets, commonly known as the "dirty beam."

We will examine several ways to measure these correlations in the sequel. We will also examine the calculation of the Fourier transform.

This page intentionally left blank.

APPENDIX 3 – MATHEMATICAL ANALYSIS OF (DIRTY) IMAGE GENERATION VIA CLASSICAL FIELD-TRANSFORMATION

We begin with equation (A1-15) (and we recall that this model assumed that the paths have been delay-equalized)

$$E_k(t) \equiv \frac{1}{\sqrt{A_k}} \int_{\mathcal{A}_k} d^2\boldsymbol{\rho'}_k \, E_k(\boldsymbol{\rho'}_k, t) e^{-j\frac{2\pi}{\lambda Z}\boldsymbol{\rho_k}\cdot\boldsymbol{\rho'}_k} \tag{A3-1}$$

Similar to the steps in Appendix 2, we can rewrite the exponent (with obvious nomenclature, and remembering that $\boldsymbol{\rho'}_k/Z$ is the same for all telescopes)

$$\frac{2\pi}{\lambda Z}\boldsymbol{\rho_k}\cdot\boldsymbol{\rho'}_k = 2\pi\left(\frac{x_k}{\lambda}\xi + \frac{y_k}{\lambda}\eta\right) \tag{A3-2}$$

so our Inverse Discrete Fourier Transform would calculate (for all N telescopes the same size and where we have ignored their area, *A*)

$$\tilde{\tilde{E}}_s(\hat{\xi},\hat{\eta},t) \approx \frac{1}{N}\sum_k E_k(t)\, exp\left[-j2\pi\left(\frac{x_k}{\lambda}\hat{\xi} + \frac{y_k}{\lambda}\hat{\eta}\right)\right] \tag{A3-3}$$

We will be interested in the image, though, so we calculate the squared magnitudes of this transformed field to find (normalized here)

$$\left\langle\left|\tilde{\tilde{E}}_s(\hat{\xi},\hat{\eta},t)\right|^2\right\rangle \approx \frac{1}{N^2}\sum_k\sum_j \langle {E_k}^*(t)\, E_j(t)\rangle \quad exp\left[-j2\pi\left(\left[\frac{x_j - x_k}{\lambda}\right]\hat{\xi} + \left[\frac{y_j - y_k}{\lambda}\right]\hat{\eta}\right)\right] \tag{A3-4}$$

$$= \frac{1}{N^2}\int_{-\infty}^{\infty}\int \tilde{I}_S(\xi,\eta)\left\{\sum_j\sum_k exp\left[j2\pi\left(\frac{\Delta x_{jk}}{\lambda}[\xi - \hat{\xi}] + \frac{\Delta y_{jk}}{\lambda}[\eta - \hat{\eta}]\right)\right]\right\} d\xi d\eta$$

which is the same as (A2-8), the dirty image of the vC-Z approach.

This page intentionally left blank.

APPENDIX 4 – SIMPLIFIED QUANTUM ANALYSIS OF GJC - BINARY

In the simplest form, we can model the state, when it contains one photon, of the signal impinging on the two telescopes (Left Telescope, LT, and Right Telescope, RT) as

$$\frac{1}{\sqrt{2}}\left[|0\rangle_{LT}|1\rangle_{RT} + e^{j\emptyset}|1\rangle_{LT}|0\rangle_{RT}\right] \tag{A4-1}$$

where $\emptyset$ is the phase difference between the signal at the two telescopes, due to the beam's slight tilt with respect to the telescopes' pointing angle. That is, the photon is modeled as coming from a point other than the sky object's center.

A more complete quantum model allows for thermal light to have come from anywhere on the distant source and is thus better modeled with the mixed-state density matrix

$$\rho = \frac{1}{2}\begin{bmatrix} 1 & V^* \\ V & 1 \end{bmatrix} \tag{A4-2}$$

where the basis vectors here are $|01\rangle, |10\rangle$, and the so-called complex visibility, V, is a function of the distance (baseline) between the telescopes as well as the off-axis angle of the particular source, and presumes that the image is resolvable by the baseline separation. (A more complete set of basis vectors would be $|00\rangle, |01\rangle, |10\rangle, |11\rangle$, plus kets with 2 or more photons, but we will here ignore the cases with no photons and also with more than one. That is, the no-photon term and the multiple-photon terms are assumed to have coefficients 0 in this model.)

It will be useful to perform a Singular Value Decomposition (SVD, ie, eigenvalue/eigenvector factorization) of this matrix. We can thus find (by solving the characteristic equation) that

$$\rho = \frac{1}{2}\begin{bmatrix} 1 & V^* \\ V & 1 \end{bmatrix} = \frac{1}{2} P \Lambda P^{\dagger} \tag{A4-3}$$

where

$$\Lambda = \begin{bmatrix} 1+|V| & 0 \\ 0 & 1-|V| \end{bmatrix}, \qquad V = |V|e^{j\emptyset} \tag{A4-4}$$

and

$$P = \frac{1}{\sqrt{2}}\begin{bmatrix} 1 & 1 \\ e^{j\emptyset} & -e^{j\emptyset} \end{bmatrix} \tag{A4-5}$$

This means that we can represent the density matrix (again, just the component with exactly one photon) as

$$\hat{\rho} = \frac{1}{2}\{(1+|V|)|\psi_{\emptyset}^{+}\rangle\langle\psi_{\emptyset}^{+}| + (1-|V|)|\psi_{\emptyset}^{-}\rangle\langle\psi_{\emptyset}^{-}|\} \tag{A4-6}$$

where the new orthonormal eigen-basis is

$$|\psi_{\emptyset}^{\pm}\rangle = \frac{1}{\sqrt{2}}\left[|0\rangle_{LT}|1\rangle_{RT} \pm e^{j\emptyset}|1\rangle_{LT}|0\rangle_{RT}\right] \tag{A4-7}$$

as can be seen from the two columns of P.

With this model, we can first see how the classical, non-local architecture displayed in Figure 13 works. If we let the variable delay correspond to a phase shift of δ radians, and model the beamsplitter as

$$\begin{aligned} |01\rangle &\rightarrow [|01\rangle + |10\rangle]/\sqrt{2} \qquad \text{and} \\ |10\rangle &\rightarrow [|01\rangle - |10\rangle]/\sqrt{2} \end{aligned} \tag{A4-8}$$

then we find the output density matrix:

$$\rho = \frac{1}{2}\begin{bmatrix} 1+Re\left(Ve^{-j\delta}\right) & jIm\left(Ve^{-j\delta}\right) \\ -jIm\left(Ve^{-j\delta}\right) & 1-Re\left(Ve^{-j\delta}\right) \end{bmatrix} \tag{A4-9}$$

which means that the probability of measuring $|01\rangle$ in this direct detection architecture is $\left[1+Re\left(Ve^{-j\delta}\right)\right]/2$, and of measuring $|10\rangle$ is $\left[1-Re\left(Ve^{-j\delta}\right)\right]/2$. We can remove the "pedestal" by taking the difference of these measurements.

GJC proposes creating and disseminating the following entangled state over the network (N), as shown in Figure 14.

$$|\varphi\rangle = (|1\rangle_{LN}|0\rangle_{RN} + e^{j\delta}|0\rangle_{LN}|1\rangle_{RN})/\sqrt{2} \tag{A4-10}$$

We thus have the joint state $|\psi_{\emptyset}^{\pm}\rangle|\varphi\rangle$. When we put these states into two beamsplitters, with outputs A and B, we find (ignoring the cases with two photons in a mode)

$$|\mathrm{z}^{\pm}\rangle = \tag{A4-11}$$

$$= \left(e^{j\delta}[|1\rangle_{LA}|0\rangle_{LB} + |0\rangle_{LA}|1\rangle_{LB}][|0\rangle_{RA}|1\rangle_{RB} - |1\rangle_{RA}|0\rangle_{RB}]/2 \right.$$
$$\left. \pm e^{j\Theta}[|0\rangle_{LA}|1\rangle_{LB} - |1\rangle_{LA}|0\rangle_{LB}][|1\rangle_{RA}|0\rangle_{RB} + |0\rangle_{RA}|1\rangle_{RB}]\right)/2$$

$$\equiv \frac{(e^{j\delta} \mp e^{j\Theta})}{\sqrt{2}}|x_1\rangle + \frac{(e^{j\delta} \pm e^{j\Theta})}{\sqrt{2}}|x_2\rangle$$

where

$$|x_1\rangle = [|1\rangle_{LA}|0\rangle_{LB}|0\rangle_{RA}|1\rangle_{RB} - |0\rangle_{LA}|1\rangle_{LB}|1\rangle_{RA}|0\rangle_{RB}]/\sqrt{2} \tag{A4-12}$$

and

$$|x_2\rangle = [|0\rangle_{LA}|1\rangle_{LB}|0\rangle_{RA}|1\rangle_{RB} - |1\rangle_{LA}|0\rangle_{LB}|1\rangle_{RA}|0\rangle_{RB}]/\sqrt{2}$$

Plugging these back into the density operator (and ignoring the 2-photon terms), we find

$$\hat{\rho} \to \frac{1}{2}\{(1 + |V|)|z^+\rangle\langle z^+| + (1 - |V|)|z^-\rangle\langle z^-|\} \tag{A4-13}$$

$$= [1 - |V|\cos(\Theta - \delta)]|x_1\rangle\langle x_1| + [1 + |V|\cos(\Theta - \delta)]|x_2\rangle\langle x_2|$$

We see that we will measure $|x_1\rangle$, i.e.,

$$[|1\rangle_{LA}|0\rangle_{LB}|0\rangle_{RA}|1\rangle_{RB} \; or \; |0\rangle_{LA}|1\rangle_{LB}|1\rangle_{RA}|0\rangle_{RB}] \tag{A4-14}$$

with probability $[1 - |V|\cos(\Theta - \delta)]/2$

and $|x_2\rangle$, i.e.,

$$[|0\rangle_{LA}|1\rangle_{LB}|0\rangle_{RA}|1\rangle_{RB} \; or \; |1\rangle_{LA}|0\rangle_{LB}|1\rangle_{RA}|0\rangle_{RB}] \tag{A4-15}$$

with $[1 - |V|\cos(\Theta + \delta)]/2$

Of course, we will need to account for the fact that we will find two photons half the time.

This page intentionally left blank.

APPENDIX 5 – SIMPLIFIED QUANTUM ANALYSIS OF GJC – M-ARY

Let us try to extend our mathematical structure to N telescopes at 2-D positions, $\left\{\underline{\rho_i}\right\}$. (Some more general descriptions sometimes include the third dimension as well.) The density matrix can be represented

$$\rho = \frac{1}{N} G = \left\{\frac{1}{N} g_{i,k}\right\} \tag{A5-1}$$

where the visibilities

$$g_{ik} = g\left(\frac{\underline{\rho_i} - \underline{\rho_k}}{\lambda}\right) = |g_{ik}| e^{j\emptyset_{ik}} \quad ; \; i \neq k; \tag{A5-2}$$

$$\text{and } g_{ki} = g\left(\frac{\underline{\rho_k} - \underline{\rho_i}}{\lambda}\right) = \; g\left(-\left[\frac{\underline{\rho_i} - \underline{\rho_k}}{\lambda}\right]\right) = {g_{ik}}^*$$

are functions of the baselines between the 2-D vectors, and so we see $g_{i,k} = g^*_{k,i}$, and $g_{i,i} = g(0) = 1$. (We note that in some references, the N and λ terms might not be included explicitly in the definition of g.) The basis quantum vector-states $\{|1_i\rangle\}$ i=0,1,…..N , were defined in the report. Written out, the density operator is

$$\hat{\rho} = \frac{1}{N} \sum_{i=0}^{N-1} \sum_{k=0}^{N-1} g_{ik} |1_i\rangle\langle 1_k| \tag{A5-3}$$

$$= \frac{1}{N} I + \frac{1}{N} \sum_{i=0}^{N-2} \sum_{k>i}^{N-1} \{g_{ik} |1_i\rangle\langle 1_k| + {g_{ik}}^* |1_k\rangle\langle 1_i|\}$$

We can once again try to find the SVD of this Hermitian operator in the form

$$G = P \Lambda P^{\dagger}$$

where P is a unitary matrix defined on those same basis vectors, and which defines N new orthonormal eigen-states $|\psi_j\rangle$ based on its columns. This equation would then be equivalent to (again, ignoring the all-zero states)

$$\hat{\rho} = \frac{1}{N}\sum_{j=0}^{N-1} \lambda_j \, |\psi_j\rangle\langle\psi_j| \tag{A5-4}$$

where λ_j are the elements of the diagonal matrix, Λ.

Unfortunately, we have been unable to find a simple closed-form solution to this SVD factorization, even for as few as 3 telescopes, for arbitrary $\{g_{i,j}\}$. However, by analogy with the N=2 case, one can show the *potentially* useful form

$$\hat{\rho} = \frac{1}{N}\sum_{i=0}^{N-2}\sum_{k>i}^{N-1}\left(\frac{1}{(N-1)} + |g_{ik}|\right)|\psi_{ik}^{+}\rangle\langle\psi_{ik}^{+}| + \left(\frac{1}{(N-1)} - |g_{ik}|\right)|\psi_{ik}^{-}\rangle\langle\psi_{ik}^{-}| \tag{A5-5}$$

if we define the states (for $i \neq k$)

$$|\psi_{ik}^{\pm}\rangle = \frac{1}{\sqrt{2}}\left[|1_i\rangle \pm e^{j\emptyset_{ik}}|1_k\rangle\right] \tag{A5-6}$$

We see that $|\psi_{ij}^{+}\rangle$ and $|\psi_{ij}^{-}\rangle$ are orthogonal, and $|\psi_{ij}^{\pm}\rangle$ and $|\psi_{kl}^{\pm}\rangle$ are orthogonal for i,j,k,l all different, but $|\langle\psi_{ij}^{\pm}|\psi_{kl}^{\pm}\rangle| = \frac{1}{2}$ if one of the i,j pair is the same as one of the k,l pair, so this is not a true SVD. Note that there are 2x $\binom{N}{2}$ such states.

APPENDIX 6 – PERFORMANCE ANALYSIS OF VC-Z WITH DIRECT DETECTION

The receiver for the classical approach takes the delay-equalized fields ((A1-14,15)) from a pair of telescopes n and m and combines them on a 50-50 beamsplitter as

$$\left[e^{j\theta}E_n(t) \pm E_m(t)\right]/\sqrt{2} \tag{A6-1}$$

The outputs are fed to ideal (unit quantum efficiency, zero dark counts) photodetectors. Half of a T_M-second measurement interval is devoted to photon counting with θ = 0, and the other half is devoted to photon counting with θ = π/2. The resulting counts are statistically independent, Poisson random variables conditioned on knowledge of their illuminating fields, which are

$$N_{nm\pm}(\theta) = Poisson\left\{\int_{T_M/2} dt\left|e^{j\theta}E_n(t) \pm E_m(t)\right|^2/2\right\} \tag{A6-2}$$

We then create

$$\hat{g}_{nm} \equiv \left\{\left(N_{nm+}(0) - N_{nm-}(0)\right) - j\left(N_{nm+}\left(\frac{\pi}{2}\right) - N_{nm-}\left(\frac{\pi}{2}\right)\right)\right\}/T_M \tag{A6-3}$$

to create an unbiased estimator of the correlation (which is complex.)

To derive the SNR, we will use (A2-1,2) – repeated here with τ=0 and $A_n = A_m = A$, and writing in angular coordinates -

$$\langle E_n{}^*(t)E_m(t)\rangle = \{\mathcal{N}_S R_S(0)\}\int \; d^2\boldsymbol{\alpha}\; \tilde{I}_s(\boldsymbol{\alpha})e^{j2\pi\left[\frac{(\boldsymbol{\rho_n}-\boldsymbol{\rho_m})}{\lambda}\right]\cdot\boldsymbol{\alpha}} \tag{A2-2}$$

$$\text{and } \langle|E_m(t)|^2\rangle = \{\mathcal{N}_S R_S(0)\}$$

We can thus see

$$\left(N_{nm+}(\theta) - N_{nm-}(\theta)\right) = Poisson\left\{2Re\left[e^{j\theta}\int_{T_M/2} dtE_n(t)E_m{}^*(t)\right]\right\} \tag{A6-4}$$

$$\left(N_{nm+}(\theta) + N_{nm-}(\theta)\right) = Poisson\left\{\int_{T_M/2} dt\left(|E_n(t)|^2 + |E_m(t)|^2\right)\right\}$$

and so

$$\langle \hat{g}_{nm} \rangle = \left\{ 2Re\left[\int_{T_M/2} dt E_n(t) {E_m}^*(t) \right] - j2Re\left[j \int_{T_M/2} dt E_n(t) {E_m}^*(t) \right] \right\} / T_M \tag{A6-5}$$

$$= \frac{\langle \int dt E_n(t) {E_m}^*(t) \rangle}{T_M} = g_{nm} = \{ \mathcal{N}_S R_S(0) \} \int \; d^2\boldsymbol{\alpha} \; \tilde{I}_s(\boldsymbol{\alpha}) e^{j2\pi \left[\frac{(\boldsymbol{\rho_n} - \boldsymbol{\rho_m})}{\boldsymbol{\lambda}} \right] \cdot \boldsymbol{\alpha}}$$

and

$$Var\hat{g}_{nm} = \left\{ VarN_{nm+}(0) + VarN_{nm-}(0) + VarN_{nm+}\left(\frac{\pi}{2}\right) + VarN_{nm-}\left(\frac{\pi}{2}\right) \right\} / {T_M}^2 \tag{A6-6}$$

$$= \left\{ \langle N_{nm+}(0) \rangle + \langle N_{nm-}(0) \rangle + \langle N_{nm+}\left(\frac{\pi}{2}\right) \rangle + \langle N_{nm-}\left(\frac{\pi}{2}\right) \rangle \right\} / {T_M}^2$$

$$= 2\{ \mathcal{N}_S R_S(0) \} / T_M$$

Finally, we can write

$$SNR\hat{g}_{nm} = \frac{|\langle \hat{g}_{nm} \rangle|^2}{Var\hat{g}_{nm}} = \frac{T_M}{2} \{ \mathcal{N}_S R_S(0) \} \left| \int \; d^2\boldsymbol{\alpha} \; I_s(\boldsymbol{\alpha}) e^{j2\pi \left[\frac{(\boldsymbol{\rho_n} - \boldsymbol{\rho_m})}{\boldsymbol{\lambda}} \right] \cdot \boldsymbol{\alpha}} \right|^2 \tag{A6-7}$$

This SNR would be further reduced by any transmission loss and any non-unit-detection-efficiency of the detector.

APPENDIX 7 – PERFORMANCE ANALYSIS OF VC-Z WITH HETERODYNE DETECTION

We choose to model this architecture with classical fields. The architecture of a heterodyne detector from a single telescope is:

- Bandlimit the incoming signal to a band, B (which means that the very large band to be examined must be frequency-multiplexed into many, many subbands)
- Combine on a beamsplitter this signal and a large local oscillator laser offset from the center frequency of that band
- Perform balanced detection and bandlimit to B
- For correlation-based measurements, send (at low loss) the outputs from two heterodyne detectors to the correlator, mix their complex envelopes, and integrate over a measurement time, T_M

We model the output of the heterodyne mixer as

$$r_m(t) = Re\{\mathbf{r}_m(t)e^{-j\omega_{IF}t}\} = Re\{[E'_m(t) + n_m(t)]e^{-j\omega_{IF}t}\} \quad \text{(A7-1)}$$

where $E'_m(t)$ is the band-limited version of $E_m(t)$ and $n_m(t)$ is the complex envelope of the passband-limited local-oscillator shot noise. We will use this output as the estimate of the received field.

To calculate the SNR of the correlation measurement approach, we see that this output will lead to an unbiased estimate of the vC-Z correlation (i.e., the mean will equal the desired signal) and the variance (when local-oscillator shot-noise-limited) will be independent of the signal. The result, when compared to the classical, direct detection approach, is that

$$SNR\hat{g}_{nm,het} = \frac{\left|\langle \hat{g}_{nm,het} \rangle\right|^2}{Var\hat{g}_{nm,het}} = 2r\mathcal{N}_S SNR\hat{g}_{nm,DD} \quad \text{(A7-2)}$$

The factor of 2 comes from the classical system's need to split the power and make two separate measurements for I and Q. (In the case of non-unity detection efficiency, η, there will also be two factors of η in this balanced heterodyne system, while only one in the vC-Z approach.) The value r is the ratio of the total measurement bandwidths, which can be as close to 1 as possible for many, many parallel heterodyne bands. We note that a 20 THz total band (which we use in the system sizing section) and a 2 GHz heterodyne band would require 2,000 parallel heterodyne channels (and assumes they are packed losslessly into the 20 THz).

This page intentionally left blank.

APPENDIX 8 – PERFORMANCE ANALYSIS OF VC-Z WITH GJC MEASUREMENTS

The architecture is shown in Figure 14. Following GJC, in each time bin, we create a photon, send it through a balanced beamsplitter, and transmit the entangled pair to the telescopes where we employ noiseless, unit-efficiency photon counters as shown. We will here use quantum operator mathematics.

Exactly following our classical approach, we replace our complex field envelope with baseband field operators, with commutators

$$\left[\hat{E}_n(t), \hat{E}_m(u)^{\dagger},\right] = \delta_{nm}\delta(t-u) \tag{A8-1}$$

where δ_{nm} is the Kronecker delta function. These quantum fields are in a zero-mean, classical, jointly-Gaussian state whose N(N − 1)/2 baselines (for N telescopes) have the same coherence functions as the classical version,

$$\langle \hat{E}_n(t)^{\dagger} \hat{E}_m(u)\rangle = \{\mathcal{N}_S R_S(0)\} \int \; d^2\boldsymbol{\alpha}\; \tilde{I}_s(\boldsymbol{\alpha}) e^{j2\pi\left[\frac{(\boldsymbol{\rho_n}-\boldsymbol{\rho_m})}{\lambda}\right]\cdot\boldsymbol{\alpha}} \tag{A8-2}$$

The GJC on-demand photon source can be modeled

$$\hat{E}(t) = \sum_m^M \hat{a}_m\, \phi\left(t - mT_p\right) + \widehat{vacuum} \tag{A8-3}$$

where $\hat{a}_m$ is the photon annihilation operator for that field's excited modes; $\phi(t)$ is a unit-normalized temporal-mode function time-limited to $|t| \le t_S/2 \le T_p/2$ where T_p is the pulse repetition period; T_M is the measurement period, likely chosen to be >> T_p. The $\widehat{vacuum}$ term represents unexcited modes which ensure that (A8-1) is satisfied.

We have found, with a detailed analysis not included here, that the performance results one gets from the fully quantum analysis is exactly the same as both a classical field analysis and a Poisson-Bernoulli calculation using photon counts based on signal power. This is true for both the classical correlation approach and the GJC approach. In fact, we have found that the Poisson-Bernoulli approach allows one to calculate either performance after a fixed time, or the performance based on counting a fixed number of photons with the experiment time being the variable.

The architecture in Figure 14 and the equations (10) and (11) tell us we are looking for coincidences aa/bb or ab/ba. If we let $N_{n,a}, N_{n,b}, N_{m,a}, N_{m,a}$ be the (Poisson) photon counts at telescope n, detectors a and b and telescope m, detectors a and b, then the variable we are interested in is

$$\left(N_{n,a} - N_{n,b}\right)\left(N_{m,a} - N_{m,a}\right) \tag{A8-4}$$

We can find the mean and variance of this quantity by observing that $\hat{E}(t)$ and $\hat{E}_n(t)$ are independent. Thus the mean of the term is made up of 4-fold products which can be expanded and calculated.

For the covariance of the two sequential measurements that form I and Q, we need higher-order products. Thanks to our Gaussian signal assumption, these, too, can be factored and (tediously) expanded and calculated.

We can ultimately find

$$SNR\hat{g}_{nm} = \frac{|\langle \hat{g}_{nm} \rangle|^2}{Var\hat{g}_{nm}} = \frac{T_M\{\mathcal{N}_S R_S(0)\}}{2}\left(\frac{d_f {M_t}^2}{2}\right)\left|\int d^2\boldsymbol{\alpha}\ \tilde{I}_s(\boldsymbol{\alpha}) e^{j2\pi\left[\frac{(\boldsymbol{\rho_n}-\boldsymbol{\rho_m})}{\lambda}\right]\cdot\boldsymbol{\alpha}}\right|^2 \tag{A8-5}$$

where $d_f = t_s/T_p$ is the single photon source's duty factor, and

$$M_t = \frac{\int_{-\frac{t_s}{2}}^{\frac{t_s}{2}} dt \int_{-\frac{t_s}{2}}^{\frac{t_s}{2}} du\ \phi(t)\, R_S(t-u)\phi^*(u)}{t_s R_S(0)} \tag{A8-6}$$

is the temporal mismatch factor between the single-photon source's temporal mode and the temporal characteristics of the sky photons arriving at the telescopes.

Similar to the classical case, any non-repeatered transmission of the single photon will see a loss that directly reduces the SNR. Different from classical, though, is the fact that it requires two simultaneous photon measurements to perform GJC, so with detection efficiency, η, we reduce the GJC SNR by η^2.

In theory, we can design $\phi(t)$ to maximize M_t by noticing that (A8-6) is a standard Fredholm integral, known to be optimized if we expand $R_S(t)$ as a sum of orthogonal functions and then select $\phi(t)$ to be that function corresponding to the largest eigenvalue. M_t is then the ratio of this largest eigenvalue to the sum of all the eigenvalues.

APPENDIX 9 – QUANTUM LOGIC ANALYSIS OF KBdGL HERALDING

Following our simplified qubit analysis of Appendix 4, we define the sky photon by

$$\hat{\rho} = \frac{1}{2}\{(1+|V|)|\psi_{\emptyset}^{+}\rangle\langle\psi_{\emptyset}^{+}| + (1-|V|)|\psi_{\emptyset}^{-}\rangle\langle\psi_{\emptyset}^{-}|\} \tag{A9-1}$$

$$|\psi_{\emptyset}^{\pm}\rangle = \frac{1}{\sqrt{2}}\left[|0\rangle_{LT}|1\rangle_{RT} \pm e^{j\emptyset}|1\rangle_{LT}|0\rangle_{RT}\right] \tag{A9-2}$$

and disseminate the (binary) entangled qubit

$$|\varphi\rangle = \left(|0\rangle_{LN}|0\rangle_{RN} + e^{j\delta}|1\rangle_{LN}|1\rangle_{RN}\right)/\sqrt{2} \tag{A9-3}$$

likely storing it in memory cells at the telescopes. Following KBdGL, we use the sky qubits as the controls in local controlled-phase (CZ) quantum logic gates against the disseminated state in each memory. We see from (A9-2) that a single photon in $|\psi_{\emptyset}^{\pm}\rangle$ transforms the entangled qubit to

$$\left(|0\rangle_{LN}|0\rangle_{RN} - e^{j\delta}|1\rangle_{LN}|1\rangle_{RN}\right)/\sqrt{2}$$

while any no-photon or two-photon terms leaves it unchanged. If we apply a Hadamard transformation to this possibly transformed state, it is easy to show that the non-photon (or two-photon) term produces an even count across the two telescopes, but the single-photon term produces an odd count. Then, by using classical communication of the two measured outputs, we can deduce (ie, herald) whether the sky qubit appears in one or the other of the two telescope memories in that time bin.

Similar to GJC, we can generalize this approach to the entire M-ary array, using a disseminated GHZ state,

$$|\varphi\rangle = (|0\rangle|0\rangle|0\rangle|0\rangle \ldots + e^{j\delta}|1\rangle|1\rangle|1\rangle|1\rangle \ldots)/\sqrt{2} \tag{A9-4}$$

which, with the same quantum logic and classical communication, can herald whether a photon has fallen somewhere in the array in that time bin.

This page intentionally left blank.

APPENDIX 10 – QUANTUM LOGIC ANALYSIS OF KBdGL MEMORY COMPRESSION

KBdGL have devised a method for greatly reducing the number of memories required to store the sky photons and also the number of entangled states required for heralding. With pre-knowledge of the approximate flux rate in the system, they propose selecting a time period in which it is likely that at most one photon will be detected in the entire array. Numbering the time bins in that period 0,1,2…….. K-1, it can be seen that a $\log_2(K+1)$ bit binary address can uniquely list them (see Figure 20).

The compression idea first puts the received sky qubit into a "working" quantum memory. We will work out the math assuming two telescopes, A and B. (Performing the algorithm on N telescopes is a straightforward extension.) We write the sky photon in the working memory as

$$|0\rangle_{Aw}|1\rangle_{Bw} + e^{j\theta}|1\rangle_{Aw}|0\rangle_{Bw} \tag{A10-1}$$

(We will drop normalizing constants throughout this Appendix. We are also using the phase-only description of visibility. We saw in Appendices 4 and 5 that we can describe the more complete density operator with sums of such simpler descriptions.)

The binary addresses are used to enable (or not) a CNOT logic gate controlled by the sky qubit with outputs placed in the "m"emory bank of length $\log_2(K+1)$, as shown in Figure 20. An enabled CNOT leads to

$$\begin{aligned} &|0\rangle_{Aw}|0\rangle_{Am}|1\rangle_{Bw}|1\rangle_{Bm} + e^{j\theta}|1\rangle_{Aw}|1\rangle_{Am}|0\rangle_{Bw}|0\rangle_{Bm} \\ &\qquad = |0\rangle_{Aw}|1\rangle_{Bw}|0\rangle_{Am}|1\rangle_{Bm} + e^{j\theta}|1\rangle_{Aw}|0\rangle_{Bw}|1\rangle_{Am}|0\rangle_{Bm} \end{aligned} \tag{A10-2}$$

After a sky photon is captured, we find that it has been written into the memories according to the time address.

We would then like to reuse the working memory, so that we do not need a new one for each of the K time bins. Because of the entanglement with the memory bank, though, the working memory must be dealt with carefully after each time slot. For instance, after we use it in the CNOT, we cannot measure it, since that would collapse the superposition and give away that the photon was on one side or the other, thus destroying the phase information in the long-term memory. Neither can we erase nor reset the working

memory, since that corresponds to taking a trace over the several now-entangled qubits and would end up with a mixture instead of the superposition that holds the phase.

KGdBL propose applying a Hadamard operation to the working memory and then measuring that state (ie in the x-basis.) The Hadamard results in

$$\begin{aligned}[|0\rangle_{Aw}|0\rangle_{Bw} - |1\rangle_{Aw}|1\rangle_{Bw}]\left[|0\rangle_{Am}|1\rangle_{Bm} + e^{j\theta}|1\rangle_{Am}|0\rangle_{Bm}\right] \\ - [|0\rangle_{Aw}|1\rangle_{Bw} - |1\rangle_{Aw}|0\rangle_{Bw}]\left[|0\rangle_{Am}|1\rangle_{Bm} - e^{j\theta}|1\rangle_{Am}|0\rangle_{Bm}\right]\end{aligned} \tag{A10-3}$$

We can see that, if the measurement of the working memory pair then produces an even number of counts, the superposition in long-term memory is unchanged, but if there are an odd number of counts, the superposition has had a sign change, which will need to be corrected. We can keep track of the sign changes versus the time addresses in a classical memory.

After the K time slots have all arrived, we then want to deduce which, if any, time slot contained a photon in the array. To this end, we send a GHZ state for each memory bin. Using the memory bin as the control of a CZ gate operating on the GHZ state,

$$|\Phi^{\pm}\rangle = \frac{1}{\sqrt{2}}[|0000\ldots\rangle \pm |1111\ldots\rangle] \tag{A10-4}$$

we can see that $|\Phi^{\pm}\rangle \rightarrow |\Phi^{\mp}\rangle$ if the array memory cell contained one photon. Applying a Hadamard to the processed GHZ state, then, and measuring it in the x-basis, we find an even count with no photons and an odd count with one photon. (These array-wide measurements require classical communications.) The memory cell remains unchanged.

We must now carefully read out the memory cell. Applying a Hadamard transformation to those cells corresponding to 1's in the address, and measuring, we find that the remaining entangled memory cells see bit flips when the measurement is odd. When there is one memory cell left, our accounting and array-wide classical communications tell us whether it is the original qubit or has had CZ applied to it, which can be corrected.

What remains is a single array-wide memory cell with the heralded photon. This cell can be used to make a correlation measurement (with a disseminated W-state like GJC) or it can be teleported to a central facility for performing the QFT.

APPENDIX 11 – PERFORMANCE ANALYSIS OF (DIRTY) IMAGE FORMATION

To calculate the SNR of the dirty image, we will find the relationship between the value of the image at an arbitrary point and the underlying Poisson counts that make it up. We will examine both correlation-based Fourier transforms (i.e., vC-Z) and field-based, both classical and QFT. Our model will be the KxK regular, filled array. (We admit that a more realistic and sparser array may give different results.)

CORRELATION-BASED IMAGES

The formula for image creation based on the measured visibilities is given in (6) and (30). Equation (4) shows the second order moment of the Poisson variables that are used to create the correlations. Since SNR for Poisson-based variables is $\frac{\mu^2}{\mu} = \mu$ for Poisson mean, μ, we can find the SNR for the correlation-based Fourier Transform with careful normalization of the array. We also observe that each of the $\binom{K^2}{2}$ elements of the input to the FT is independent of the others, since each correlation is based on a unique set of photons.

We can define a 2-D dirty image as $\mathcal{I}(\boldsymbol{j})$ at grid point $\boldsymbol{j}$, to be normalized as $\sum \sum_{\boldsymbol{j}} \mathcal{I}(\boldsymbol{j}) = 1$. From these inputs and some algebra, it can be shown (where the filled square array simplifies much of the math in the multiple summations) that the correlation-based dirty image has SNR

$$SNR_C(\boldsymbol{j}) = \frac{K^6 T}{2(K^2-1)^2}\{\mathcal{N}_S R_S(0)\}\mathcal{I}(\boldsymbol{j})^2 \tag{A11-1}$$

For a Gaussian-shaped spectrum ((A1-11,12)), $R_S(0) = \frac{1}{\sqrt{4\pi}t_S}$ where t_S is the coherence time of the source. At large K, this gives

$$SNR_C(\boldsymbol{j}) = \frac{T\mathcal{N}_S K^2}{4\sqrt{\pi}t_S}\mathcal{I}(\boldsymbol{j})^2 \tag{A11-2}$$

We note that this formula had measured all the distinct baselines, including redundant ones in our filled array. In work not shown here, we have also investigated measuring only the non-redundant baselines (which allows more of the T-seconds of total integration to be used for each correlation.) It turns out that the result differs by only a small fraction, but the dirty beam is somewhat different and it is thus difficult to make a direct comparison.

CLASSICAL FIELD-BASED IMAGES

The formula for image creation based on the fields is given in (8) and (9). Once again, with careful normalization, and noting that that there are only K^2 independent elements in this calculation, one can show that (for large K)

$$SNR_F(\boldsymbol{j}) = \frac{T\mathcal{N}_S K^2}{2\sqrt{\pi}t_S}\mathcal{I}(\boldsymbol{j}) \qquad \text{(A11-3)}$$

(To derive this, we assumed that there were a large number of detected photons in many spatial modes, and so Poisson statistics apply. This allowed us to simplify a few expressions.)

Since the dirty image is positive and has unit total "energy", we can see that each point is on the order of $\mathcal{I}(\boldsymbol{j}) \sim \frac{1}{K^2}$. Thus, the field-based image has an SNR on the order of K^2 *greater* than that of the correlation-based image.

We show in Appendix 12 that the QFT-based field transform gives the same average output as the classical version, and so the SNR will be the same.

APPENDIX 12 – CALCULATION OF (DIRTY) IMAGE FORMATION FROM QFT

The 2-D array signals have a density operator shown here

$$\hat{\rho} = \frac{1}{K^2}\sum_{n_x=0}^{K-1}\sum_{n_y=0}^{K-1}\sum_{m_x=0}^{K-1}\sum_{m_y=0}^{K-1} g(n_x - m_x, n_y - m_y)\left|1_{n_x,n_y}\right\rangle\left\langle 1_{m_x,m_y}\right| \tag{A12-1}$$

In the same signal basis, the Quantum Fourier Transform operator can be written

$$\hat{U}_{QFT} = \frac{1}{K}\sum_{n_x=0}^{K-1}\sum_{n_y=0}^{K-1}\sum_{m_x=0}^{K-1}\sum_{m_y=0}^{K-1} exp\left[-\frac{j2\pi}{K}(n_x m_x + n_y m_y)\right]\left|1_{n_x,n_y}\right\rangle\left\langle 1_{m_x,m_y}\right| \tag{A12-2}$$

When applied to the array signals, the output is

$$\hat{\rho}_{output} = \hat{U}_{QFT}\hat{\rho}\hat{U}_{QFT}{}^{\dagger} \tag{A12-3}$$

We then measure the diagonal elements of this operator to find the estimate of the dirty image, as

$$\left\langle 1_{l_x,l_y}\right|\hat{\rho}_{output}\left|1_{l_x,l_y}\right\rangle \tag{A12-4}$$

As a first step, we calculate

$$\hat{U}_{QFT}{}^{\dagger}\left|1_{l_x,l_y}\right\rangle = \frac{1}{K}\sum_{n_x=0}^{K-1}\sum_{n_y=0}^{K-1} exp\left[\frac{j2\pi}{K}(n_x l_x + n_y l_y)\right]\left|1_{n_x,n_y}\right\rangle \tag{A12-5}$$

and from this, we ultimately find

$$\left\langle 1_{l_x,l_y}\right|\hat{\rho}_{output}\left|1_{l_x,l_y}\right\rangle = \tag{A12-6}$$
$$= \frac{1}{K^4}\sum_{n_x=0}^{K-1}\sum_{n_y=0}^{K-1}\sum_{m_x=0}^{K-1}\sum_{m_y=0}^{K-1} g(n_x - m_x, n_y - m_y)\, exp\left\{-\frac{j2\pi}{K}\left[(n_x - m_x)l_x + (n_y - m_y)l_y\right]\right\}$$

It is straightforward to show that this is the same formula as we find in the analysis (based on equations (6)-(9) and analyzed in Appendix 11) of the classical Fourier Transform approach. Thus, the QFT approach results in the same SNR as the classical FT approach, if we ignore the several losses of transmission and detection as well as the single-temporal-mode mismatch factor introduced in (19).

This page intentionally left blank.

APPENDIX 13 – CALIBRATION ANALYSIS OF (DIRTY) IMAGE FORMATION FROM FIELD TRANSFORMS

Since from (2)-(5), we have that the visibility is

$$g\left(\frac{\Delta x_{jk}}{\lambda},\frac{\Delta y_{jk}}{\lambda}\right) = \left\langle {E_k}^*(t)E_j(t)\right\rangle \tag{A13-1}$$

we can include the effects of turbulence and optics as seen at telescope k by multiplying $E_k(t)$ by a complex value h_k, resulting in the new density operator for the array (we write here only up to N-1=3, with obvious extension to more general N)

$$\hat{\rho}_h = \begin{bmatrix} h_0 & 0 & 0 & 0 \\ 0 & h_1 & 0 & 0 \\ 0 & 0 & h_2 & 0 \\ 0 & 0 & 0 & h_3 \end{bmatrix}^\dagger \begin{bmatrix} 1 & g(\boldsymbol{\rho}_0-\boldsymbol{\rho}_1) & g(\boldsymbol{\rho}_0-\boldsymbol{\rho}_2) & g(\boldsymbol{\rho}_0-\boldsymbol{\rho}_3) \\ g(\boldsymbol{\rho}_1-\boldsymbol{\rho}_0) & 1 & g(\boldsymbol{\rho}_1-\boldsymbol{\rho}_2) & g(\boldsymbol{\rho}_1-\boldsymbol{\rho}_3) \\ g(\boldsymbol{\rho}_2-\boldsymbol{\rho}_0) & g(\boldsymbol{\rho}_2-\boldsymbol{\rho}_1) & 1 & g(\boldsymbol{\rho}_2-\boldsymbol{\rho}_3) \\ g(\boldsymbol{\rho}_3-\boldsymbol{\rho}_0) & g(\boldsymbol{\rho}_3-\boldsymbol{\rho}_1) & g(\boldsymbol{\rho}_3-\boldsymbol{\rho}_2) & 1 \end{bmatrix} \begin{bmatrix} h_0 & 0 & 0 & 0 \\ 0 & h_1 & 0 & 0 \\ 0 & 0 & h_2 & 0 \\ 0 & 0 & 0 & h_3 \end{bmatrix} \tag{A13-2}$$

$$\equiv \widehat{H}^\dagger \hat{\rho} \widehat{H}$$

As there are only N measurements that can be made with any one N-array photon, we are forced to learning sequentially (or alternately) the telescope distortions plus the image.

It is straightforward to show that, after applying the QFT to the received states, we would have

$$\hat{\rho}_{output,h} = \widehat{U}_{QFT}\hat{\rho}_h {\widehat{U}_{QFT}}^\dagger = \left\{\widehat{U}_{QFT}\widehat{H}{\widehat{U}_{QFT}}^\dagger\right\}^\dagger \widehat{U}_{QFT}\hat{\rho}{\widehat{U}_{QFT}}^\dagger \left\{\widehat{U}_{QFT}\widehat{H}{\widehat{U}_{QFT}}^\dagger\right\} \tag{A13-3}$$

where the bracketed matrix has i,j element $H\left(\omega^{i+j}\right)$ and where $H(z) = \sum_{k=0}^{N-1} h(\boldsymbol{\rho_i})\, z^i$ describes the dirty beam with $\omega = e^{2\pi j/N}$.

We can try to learn the off-diagonal elements of this state (with analogy to the correlations approach) or perhaps find a way to learn $H(z)$ by learning each telescope's distortions separately, possibly by using a reference.

In either case, not getting intrinsic redundant measurements, as the correlation method can, forces us to add complexity to the field-transform method. The best way to implement this remains an open problem.

REPORT DOCUMENTATION PAGE

Form Approved
OMB No. 0704-0188

1. REPORT DATE *(DD-MM-YYYY)*	**2. REPORT TYPE**	**3. DATES COVERED** *(From - To)*
10-06-2024	Project Report	

4. TITLE AND SUBTITLE
A Survey and Assessment of Architectures for Optical Very Long Baseline Interferometry

5a. CONTRACT NUMBER

5b. GRANT NUMBER

5c. PROGRAM ELEMENT NUMBER

6. AUTHOR(S)
D.M. Boroson, J.H. Shapiro, B. Dixon, J.B. Ashcom

5d. PROJECT NUMBER
3476

5e. TASK NUMBER

5f. WORK UNIT NUMBER

7. PERFORMING ORGANIZATION NAME(S) AND ADDRESS(ES)

MIT Lincoln Laboratory
244 Wood Street
Lexington, MA 02421-6426

8. PERFORMING ORGANIZATION REPORT NUMBER
OVLBI-1

9. SPONSORING / MONITORING AGENCY NAME(S) AND ADDRESS(ES)
Under Secretary of Defense for Research and Engineering

10. SPONSOR/MONITOR'S ACRONYM(S)
USD (R&E)

11. SPONSOR/MONITOR'S REPORT NUMBER(S)

12. DISTRIBUTION / AVAILABILITY STATEMENT
DISTRIBUTION STATEMENT A. Approved for public release. Distribution is unlimited.

13. SUPPLEMENTARY NOTES

13. ABSTRACT
Motivated by the recent interest and publications in the quantum arena concerning possible improvements to Optical Very Long Baseline Interferometry (OVLBI), we have undertaken a survey and comparative analysis of a number of possible OVLBI architectures, both classical and quantum enabled. We assess here the feasibility and potential performance of them all, discussing a number of real-world considerations that must be taken into account. We also propose several technology-development paths that might lead to improved OVLBI performance.

15. SUBJECT TERMS

16. SECURITY CLASSIFICATION OF:			**17. LIMITATION OF ABSTRACT**	**18. NUMBER OF PAGES**	**19a. NAME OF RESPONSIBLE PERSON**
a. REPORT	**b. ABSTRACT**	**c. THIS PAGE**	None	114	**19b. TELEPHONE NUMBER** *(include area code)*
UNCLASSIFIED	UNCLASSIFIED	UNCLASSIFIED			